

See discussions, stats, and author profiles for this publication at: <https://www.researchgate.net/publication/328105705>

# PEM Fuel Cells: Modeling: A Volume in the Encyclopedia of Sustainability Science and Technology, Second Edition

Chapter · January 2019

DOI: 10.1007/978-1-4939-7789-5\_1019

CITATIONS

0

READS

340

5 authors, including:



**Marc Secanell**

University of Alberta

94 PUBLICATIONS 1,165 CITATIONS

[SEE PROFILE](#)



**Alex Jarauta**

University of Alberta

9 PUBLICATIONS 33 CITATIONS

[SEE PROFILE](#)



**Aslan Kosakian**

University of Alberta

3 PUBLICATIONS 9 CITATIONS

[SEE PROFILE](#)



**Mayank Sabharwal**

University of Alberta

15 PUBLICATIONS 59 CITATIONS

[SEE PROFILE](#)

Some of the authors of this publication are also working on these related projects:



Two-phase flow in PEFCs [View project](#)



PEM Fuel Cell Electrodes - Catalyst Layers (CL) and Microporous Layers (MPL) [View project](#)

See discussions, stats, and author profiles for this publication at: <https://www.researchgate.net/publication/322367301>

# PEM Fuel Cells, Modeling

Chapter · January 2018

CITATIONS

0

READS

389

5 authors, including:



Marc Secanell

University of Alberta

92 PUBLICATIONS 1,048 CITATIONS

SEE PROFILE



Alex Jarauta

University of Alberta

9 PUBLICATIONS 30 CITATIONS

SEE PROFILE



Aslan Kosakian

University of Alberta

3 PUBLICATIONS 7 CITATIONS

SEE PROFILE



Mayank Sabharwal

University of Alberta

13 PUBLICATIONS 45 CITATIONS

SEE PROFILE

Some of the authors of this publication are also working on these related projects:



Stochastic Reconstruction of Porous Media [View project](#)



Transport in Porous Media [View project](#)

# PEM Fuel Cells, Modeling

M. Secanell<sup>1,\*</sup>, A. Jarauta<sup>1</sup>, A. Kosakian<sup>1</sup>, M. Sabharwal<sup>1</sup> and J. Zhou<sup>1</sup>

Energy Systems Design Laboratory  
Department of Mechanical Engineering  
University of Alberta

19 October 2017

**Note.** This is the authors' version of the text. The published version is available in  
*Secanell M., Jarauta A., Kosakian A., Sabharwal M., Zhou J. (2017) PEM Fuel Cells, Modeling. In: Meyers R. (eds) Encyclopedia of Sustainability Science and Technology. Springer, New York, NY*  
and at [https://doi.org/10.1007/978-1-4939-2493-6\\_1019-1](https://doi.org/10.1007/978-1-4939-2493-6_1019-1).

## Contents

<b>1</b>	<b>Introduction</b>	<b>6</b>
<b>2</b>	<b>Fuel cell components and operation</b>	<b>8</b>
2.1	Bipolar plates . . . . .	8
2.2	Gas diffusion and microporous layers . . . . .	9
2.3	Catalyst layers . . . . .	11
2.4	Polymer electrolyte membrane . . . . .	13
<b>3</b>	<b>General models</b>	<b>14</b>
3.1	Mass transport in channels . . . . .	14
3.1.1	Two-phase flow in channels . . . . .	16
3.2	Mass transport in MEAs . . . . .	19
3.2.1	Gas transport . . . . .	19
3.2.2	Water transport in the polymer electrolyte . . . . .	21
3.2.3	Liquid water in MEAs . . . . .	23
3.3	Charge transport . . . . .	26
3.4	Electrochemical reactions . . . . .	29
3.5	Heat transport . . . . .	33
<b>4</b>	<b>Microscale simulation for parameter estimation</b>	<b>35</b>
<b>5</b>	<b>Implementation</b>	<b>39</b>
<b>6</b>	<b>Conclusion</b>	<b>40</b>
<b>7</b>	<b>Future directions</b>	<b>41</b>

---

<sup>1</sup>All authors contributed equally to this work.

\*secanell@ualberta.ca

# Nomenclature

$\bar{C}_p$	molar specific heat, [ $J mol^{-1} K^{-1}$ ]
$\bar{H}$	enthalpy, [ $J$ ]
$\dot{W}$	rate of work done by the system, [ $W cm^{-3}$ ]
$\mathbf{g}$	gravity vector field, [ $cm s^{-2}$ ]
$\hat{C}_p$	specific heat, [ $J g^{-1} K^{-1}$ ]
$\hat{h}$	specific enthalpy, [ $J g^{-1}$ ]
$\hat{u}$	specific internal energy, [ $J g^{-1}$ ]
$\hat{N}$	mass flux, [ $g cm^{-2} s^{-1}$ ]
$\mathcal{D}$	Maxwell-Stefan diffusion coefficient, [ $cm^2 s^{-1}$ ]
$N$	molar flux, [ $mol cm^{-2} s^{-1}$ ]
$\mathbf{q}$	molecular heat flux, [ $W cm^{-2} K^{-1}$ ]
$\mathbf{n}$	outward normal vector
$\hat{K}$	permeability tensor, [ $cm^2$ ]
$\mathbf{v}$	velocity, [ $cm s^{-1}$ ]
$A_v$	active area of Pt per unit volume of catalyst layer, [ $cm^2 cm^{-3}$ ]
$a_w$	Water activity
$a_{lv}$	liquid-gas interfacial surface area per unit volume, [ $cm^2 cm^{-3}$ ]
$c$	molar concentration, [ $mol cm^{-3}$ ]
$C_k$	volume fraction of fluid $k$
$D$	Fick's diffusion coefficient, [ $cm^2 s^{-1}$ ]
$D^K$	Knudsen diffusion coefficient, [ $cm^2 s^{-1}$ ]
$D_T$	thermo-osmotic diffusion coefficient, [ $mol cm^{-1} s^{-1} K^{-1}$ ]
$E$	half-cell voltage, [ $V$ ]
$EW$	equivalent weight of the ionomer, [ $g mol^{-1}$ ]
$F$	Faraday's constant, [ $C mol^{-1}$ ]
$h$	convective heat transfer coefficient, [ $W cm^{-2} K^{-1}$ ]
$H_{g,N}$	Henry's constant, [ $Pa cm^3 mol^{-1}$ ]
$i$	volumetric current density, [ $A cm^{-3}$ ]
$j$	current density, [ $A cm^{-2}$ ]
$j_0^{ref}$	exchange current density, [ $A cm^{-2}$ ]
$k$	equilibrium rate constant, [ $cm s^{-1} (cm^3 mol^{-1})^{(\alpha-1)}$ ]
$k_{e/c}$	evaporation or condensation rate per unit of liquid-gas interfacial surface area, [ $mol cm^{-2} s^{-1}$ ]
$K_{i,j}$	frictional interaction coefficient between species $i$ and $j$ , [ $N s cm^{-4}$ ]

$k_r$	effective permeability, [ $cm^2$ ]
$L$	characteristic length, [ $cm$ ]
$M$	molar mass, [ $g\ mol^{-1}$ ]
$n_d$	electro-osmotic drag coefficient
$p$	pressure, [ $g\ cm^{-1}\ s^{-2}$ ]
$R$	universal gas constant, [ $J\ mol^{-1}\ K^{-1}$ ]
$r_p$	pore radius, [ $cm$ ]
$S_{heat}$	Volumetric heat source, [ $W\ cm^{-3}$ ]
$T$	absolute temperature, [ $K$ ]
$t$	time, [ $s$ ]
$u_{i,k}$	mobility of species $i$ in phase $k$ , [ $cm^2\ mol\ J^{-1}\ s^{-1}$ ]
$x$	molar fraction
$z_i$	valence (or charge number) of species $i$

### Abbreviations

BPP	nipolar plate
CL	catalyst layer
CSF	continuum surface force
CSS	continuum surface stress
ECSA	electrochemically active surface area
FEP	fluorinated ethylene propylene
GDL	gas diffusion layer
ICCP	ionomer covered catalyst particle
LS	level set
MEA	membrane electrode assembly
MPL	microporous layer
PEM	proton exchange membrane
PEMFC	proton exchange membrane fuel cell
PFSA	perfluorosulfonic acid
PLIC	piecewise linear interface calculation
PTFE	polytetrafluoroethylene
VOF	volume of fluid

### Greek letters

$\alpha_i$	transfer coefficient for reaction $i$
$\bar{\kappa}$	partial viscosity, [ $g\ cm^{-1}\ s^{-1}$ ]
$\bar{v}$	specific volume, [ $cm^3\ g^{-1}$ ]

$\beta$	transfer coefficient for cathodic reaction
$\hat{\boldsymbol{\tau}}$	Cauchy stress tensor, [ $g\text{ cm}^{-1}\text{ s}^{-2}$ ]
$\Lambda$	collision diameter, [ $cm$ ]
$\hat{\kappa}$	surface curvature, [ $cm^{-1}$ ]
$\eta$	overpotential, [ $V$ ]
$\hat{\boldsymbol{\beta}}$	Forchheimer correction tensor, [ $cm$ ]
$\gamma$	surface tension coefficient, [ $g\text{ s}^{-2}$ ]
$\gamma_i$	order of reaction for reaction $i$
$\gamma_{\text{ads}}$	potential range constant for adsorption isotherm
$\hat{\mu}_i$	electrochemical potential of species $i$ , [ $J\text{ mol}^{-1}$ ]
$\hat{\rho}$	charge density, [ $C\text{ cm}^{-3}$ ]
$\kappa$	thermal conductivity coefficient, [ $W\text{ cm}^{-2}\text{ K}^{-1}$ ]
$\lambda$	sorbed water content in the membrane
$\lambda_b$	bulk viscosity, [ $g\text{ cm}^{-1}\text{ s}^{-1}$ ]
$\lambda_{eq}$	equilibrium sorbed water content in the membrane
$\mu$	dynamic viscosity, [ $g\text{ cm}^{-1}\text{ s}^{-1}$ ]
$\nu$	rate of reaction, [ $mol\text{ cm}^{-2}\text{ s}^{-1}$ ]
$\omega$	mass fraction
$\phi_k$	electrostatic potential of phase $k$ , [ $V$ ]
$\psi$	fraction of active platinum sites available
$\rho$	density, [ $g\text{ cm}^{-3}$ ]
$\boldsymbol{\tau}$	shear stress tensor, [ $g\text{ cm}^{-1}\text{ s}^{-2}$ ]
$\sigma$	conductivity, [ $S\text{ cm}^{-1}$ ]
$\tau$	tortuosity
$\theta$	coverage of intermediate reaction species
$\varepsilon$	volume fraction

### Mathematical operators

$\nabla$	gradient
$\nabla_s$	symmetric gradient, $\nabla_s = \frac{1}{2}(\nabla + \nabla^T)$
$\otimes$	tensor product
$\Theta(x)$	Heaviside step function

### Subscripts and superscripts

$DA$	dissociative adsorption reaction
$g$	gas mixture
$H$	Heyrovsky reaction

$i, j$	species indexes
$k$	phase index
$m$	electrolyte phase
$p$	percolation threshold
$RA$	reductive adsorption reaction
$RD$	reductive desorption reaction
$RT$	reductive transition reaction
$s$	solid phase
$T$	Tafel reaction
$V$	Volmer reaction
$v$	void phase

# Glossary

**Proton exchange membrane fuel cells (PEMFCs)** are energy conversion devices that transform chemical energy in a fuel directly to electricity by means of two electrochemical reactions divided by a proton conductive membrane.

**Mathematical modeling** is the development of partial differential equations for describing the physical and electrochemical processes that govern a physico-chemical system, in this entry, a PEMFC.

**Numerical modeling** is the development of numerical analysis and software tools to solve the partial differential equations that describe a physico-chemical system, in this entry, a PEMFC.

**Gas diffusion layers (GDL)** are porous, electrically conductive layers made of carbon fibers, a binder and usually coated with PTFE that are placed between a fuel cell gas channel and the catalyst layer.

**Catalyst layers (CLs)** are porous, electronically and ionically conductive composite layers made of ionomer and a supported catalysts. They are the heart of the fuel cell as it is in these layers that the electrochemical reactions take place.

**Proton exchange membranes (PEM)** are ion conductive membranes, usually made of a perfluorosulfonic acid (PFSA) polymer, that are used to separate anodic and cathodic reactions in a fuel cell.

**Ohmic transport losses** are cell voltage losses associated with the transport of charge within the fuel cell components.

**Mass transport losses** are cell voltage losses associated with either inappropriate reactant distribution to the reaction site or slow product removal.

**Kinetic losses** are cell voltage losses associated with the irreversible potential required to accelerate the rate of the electrochemical reactions.

**Open-source fuel cell software** is numerical analysis software for fuel cells where the source code is made available with a license in which the copyright holder provides the rights to study, change, and distribute the software to anyone and for any purpose. Open-source software is ideal for collaborative development.

## Definition of the subject

Proton exchange membrane fuel cell (PEMFC) operation involves multi-phase mass, charge and heat transport, complex electrochemical reactions, and physical processes that occur at multiple spatial and time scales, e.g., from double layer effects occurring in milliseconds to catalyst degradation, which becomes significant only after many hours of operation. PEMFC design is therefore a complex endeavor that requires the optimization of a multitude of objectives, such as minimizing cost and maximizing specific current density, efficiency and durability, by modifying a large design dataset that includes the geometry, composition and micro-structure of each of the components that form the cell. In order to achieve an optimal design, multi-disciplinary computational design and optimization is required. The heart of numerical design and optimization is a numerical model of the system under study, in this case a numerical model of the PEMFC. Mathematical and numerical modeling of PEMFCs is therefore critical in order to understand the physical and chemical processes occurring inside the fuel cell, and to design a PEMFC system that can meet current targets for PEMFC commercialization.

The modern era of PEMFC modeling started with the pioneering work of Springer et al. [1] and Bernardi and Verbrugge [2] in early 1990's, where one-dimensional full-cell models were considered, and has continued to present time with the development of complex three-dimensional PEMFC models including multi-component mass transport, charge and heat transport, two-phase flow, and multi-step electrochemical reactions [3–6]. In recent years, advancement in image analysis has led to the development of micro-scale numerical models [7–18]. In this entry, the reader is first introduced to the physico-chemical properties and function of each component in a fuel cell. Then, based on the expected physical processes in each component, general models are developed to describe the physico-chemical behavior of the PEMFC components. Common simplifications applied to the most general governing equations are highlighted in order to reach the most common set of governing equations used in numerical modeling software. Then, micro-scale models are reviewed and discussed. Finally, strategies used to solve the PEMFC governing equations are discussed with emphasis on the use of open-source software as a novel tool for collaborative development on numerical models for PEMFC.

## 1 Introduction

PEMFCs convert the energy in a chemical fuel, such as hydrogen, directly to electricity by means of two electrochemical reactions separated by a polymer electrolyte membrane. PEMFCs present a viable alternative to the

internal combustion engine and lithium-ion batteries in transportation, portable, and backup-power applications. The transportation sector, which is currently responsible for nearly 30% of all greenhouse gas (GHG) emission in North America, could be fueled by hydrogen gas produced using electricity from intermittent renewable sources, such as wind and solar. PEMFC vehicles fueled with hydrogen produce only water vapor as a by-product, could then eliminate nearly all particulate matter and greenhouse gas emissions associated with the sector as well as providing added-value to excess electricity from renewable resources during low demand. PEMFC vehicles have already demonstrated all attributes that customers expect, such as quick start-up and refueling, long range, and durability [19]. An increase in market penetration of PEMFC vehicles, however, will depend on further production cost reductions as well as performance and durability improvements [20].

In order to reduce the cost of transportation PEMFC stacks to commercialization targets, i.e., \$30/kW (2020 U.S. Department of Energy targets), PEMFC stacks need to be designed to achieve higher power density, and reduce or eliminate the use of expensive catalysts, such as platinum [20]. To increase durability, PEMFCs need to be designed and operated at conditions that minimize membrane damage, catalyst dissolution, and catalyst support corrosion [21]. For example, hydrogen depletion/starvation in the anode during start-up/shutdown leads to carbon corrosion [22] and oxygen starvation due to local water accumulation leads to oxygen peroxide formation which damages the polymer membrane [23]. To design such PEMFC stacks, an excellent understanding of the steady-state and transient mass, charge and heat transport and electrochemical processes occurring at the nano-, micro- and macro-scale inside each component of the fuel cell is required. PEMFC stack design is therefore a multi-scale, multi-disciplinary problem which aims at achieving multiple objectives while conforming to very stringent constraints regarding cost, durability and reliability. Such complex design problem is best tackled by numerical design and optimization which require accurate mathematical and numerical modeling tools [24, 25].

Mathematical models are a requirement for PEMFC design, but they can also provide insight into the physical and electrochemical phenomena occurring inside PEMFCs, insight that is especially challenging to obtain experimentally due to the sub-millimeter scales of most fuel cell components and the lack of visual access. Along with physical experiments and visualization, mathematical modeling can be used to estimate transport and electrochemical properties of new PEMFC materials and components by means of least-square parameter estimation [26, 27], experimental data fitting with numerical macro-homogeneous models [28], or by means of direct pore-scale simulation using imaging data [18, 29].

The modern era of PEMFC modeling started with the pioneering work of Springer et al. [1] and Bernardi and Verbrugge [2] in early 1990's, where one-dimensional full-cell models were considered. It shortly became evident that, for the detailed analysis and design of fuel cells, multidimensional models were needed in order to account for channel/landing interactions [30], oxygen depletion along the channel at low stoichiometries [5], and non-uniform temperature and relative humidity profiles [5]. This led to two-dimensional [31, 32] and three-dimensional [3–5] models. This entry will provide the reader with the necessary set of governing equations to develop their own mathematical models and numerical implementations, therefore a detailed review of the many numerical modeling articles in the literature is not provided and instead these will be cited in the context of the physical processes that they included. A number of excellent reviews have been written in the fuel cell modeling area, e.g., [33–40], the reader can refer to these publications for a detailed chronological review of the numerical models in the literature.

This entry will focus on developing a transient, multi-dimensional, multi-scale mathematical model for a fuel cell. The literature also contains multitude of analytical 1D and quasi-2D models for describing the fuel cell behavior, a collection of which can be found, for example, in references [41, 42]. These models can be used for quick, rough estimation of a certain effect, however, they are limited by dimensionality assumptions and physical simplifications. Geometry of the reactant flow fields, land-channel interactions, gas-liquid water interaction in channels and in porous media, thermal gradients, anisotropic properties and microstructural characteristics of the components are only a few of the multitude of effects that are ignored in such analytical and semi-analytical models, thereby making it challenging to analyze any results obtained. Models that are able to account for multi-dimensional reactant, product, reaction and heat variations, as well as geometrical, compositional, and morphological features are required for fuel cell design. The aim of this entry is, therefore, to develop such models instead of the aforementioned analytical 1D and quasi-2D models.

Remarkable progress has been achieved in macroscale numerical modelling of fuel cells. These models, however, cannot account for the effect microscopic features in porous composite materials in PEMFCs have on mass transport properties and reactions. Macro-scale mathematical models have thus far used semi-empirical or percolation theory-based functions to estimate the effective transport properties [43, 44]. Recent experimental and modeling work has shown that these functions can over-predict effective transport parameters by 3 to 10 times [45–48]. Recent work in low loading electrodes has also shown that large local mass transport losses at catalyst/electrolyte interfaces are present and can only be studied by accounting for the layer's micro-structural details [49–51]. During operation, liquid water accumulation in the porous media also leads to dynamic pore blockage, further reducing transport and

making the use of semi-empirical correlation functions challenging. FIB-SEM and nanoCT methods have recently been used to image catalyst layers (CLs) [52, 53] and microporous layers (MPLs) [54, 55] with resolutions of 5-20 nm and 30-50 nm, respectively. Scanning TEM has been used to visualize platinum particles in the CLs [56] and the electrolyte network [57]. Electrolyte properties in the CL are also being analyzed [58, 59]. Using imaging data from FIB-SEM and nanoCT, tortuosity [60], mass transport [18, 29, 55], liquid water injection [54], and reactions [14, 17, 18] have very recently been studied by computer simulation. This entry will, therefore, also cover this emerging area of research.

Mathematical modeling of fuel cells is most commonly performed using commercial software, e.g., ANSYS Fluent [3, 4, 61–70], COMSOL Multiphysics [71–78], Star-CD [79], and MATLAB/SIMULINK [80, 81]. While commercial software is an attractive option because it does not require much implementation effort and usually has better customer support than open-source analogs, it has a few drawbacks compared to the latter, primarily: a) lack of access to source code, which prevents users from understanding how the equations are solved and limits the flexibility of implementing novel solution and domain decomposition strategies; b) lack of collaborative development tools for sharing numerical implementation and input parameter databases; c) higher computational requirements due to the universality of commercial software which leads to a complex logical kernel (e.g., ref. [82] showed a specialized in-house code solved the same problem three to four times faster than the same model implemented in COMSOL Multiphysics); and, d) license fees, which are expensive, especially for non-academic use and when running multi-core simulations. The necessity of an open-source software in the area of fuel cells that is available for everyone has led to the development of several open-source software projects, OpenFCST [6, 83] and FastFC [84], and OpenPNM [85] for pore network modeling. Details on the implementation of the software to solve the mathematical models proposed in the entry will therefore also be discussed.

This entry starts with a brief introduction to the functionality and structure of each fuel cell component in Section 2. This insight is then used in order to develop a generalized model for transport and electrochemical reactions in the channels and membrane electrode assembly (MEA) of fuel cells in Section 3. As previously discussed, macroscale models depend on a large number of effective parameters, therefore Section 4 introduces the mathematical models currently available to extract average macroscopic parameters from imaging data. Finally, fuel cell mathematical model implementation details are provided in Section 5. The entry does not cover mathematical models involving degradation mechanisms. Even though this area is extremely important, it was excluded in order to limit the scope of the entry. For information in this area, the reader is referred to references [21, 33, 86–88].

## 2 Fuel cell components and operation

A polymer electrolyte fuel cell (PEFC) is an electrochemical energy conversion device that converts the chemical energy in a fuel to electricity by means of two electrochemical reactions that are separated by a gas tight and ion conductive electrolyte. In the case of PEMFCs, which are the subject of this entry, the electrolyte is usually a proton conductive membrane, such as Nafion<sup>®</sup>. To catalyze the electrochemical reactions, both sides of the polymer electrolyte membrane are coated with a 2-20  $\mu\text{m}$  porous catalyst layer. The catalyst coated membrane (CCM) is then sandwiched between two gas transport layers made of a microporous layer and a gas diffusion layer (GDL). This assembly, known as the membrane electrode assembly, is finally sandwiched between two conductive plates engraved with micro-channels used to deliver the reactant gas mixtures and remove the by-product water. A cross-section of a typical PEMFC is shown in Figure 2.1. Reactant gases, ions, and electrons are transported through void, electrolyte, and solid phases, respectively, in GDL, MPL, and CL. By-product water in either vapor or liquid form, and heat are also transported by these layers. Due to their multi-functional nature, these layers are composite materials with a complex micro-structure. A detailed description of each layer is provided below, including its composition, functionality, durability, and physical phenomena occurring inside the layer.

### 2.1 Bipolar plates

Bipolar plates (BPP) are responsible for:

- gas reactant supply to the cell;
- electrical connection between the cell and the current collectors;
- transport of the product heat to ambient and to the stack cooling system; and
- removal of excess water from the cell.

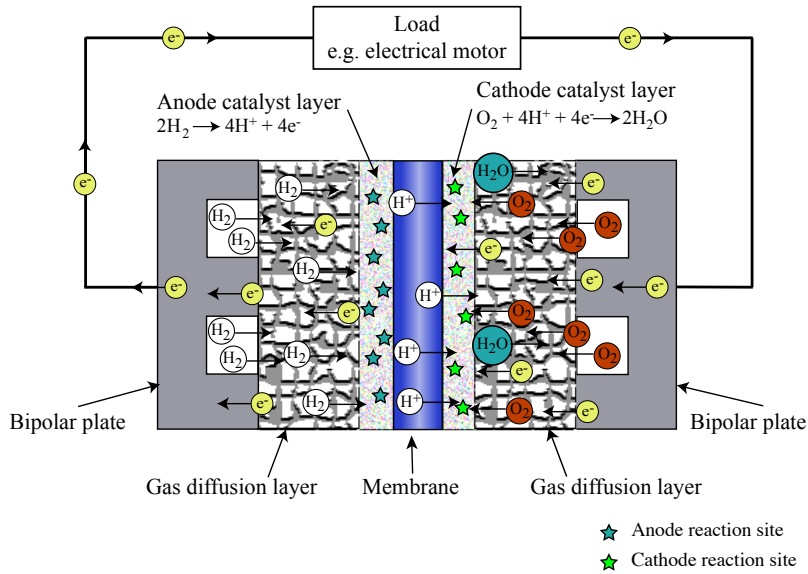


Figure 2.1: A schematic of a PEMFC cross-section. Reproduced from [82] with the permission of the author.

Since bipolar plates need to be electrically conductive, they are made of either carbon-based materials or metals [89–91]. Graphite plates are most commonly used in fuel cell hardware because metal plates suffer corrosion and dissolution under the high humidity and acidity conditions typical of PEMFCs [92–94]. To reduce the risk of degradation, metal plates are usually coated with thin corrosion-resistant films [94], which, however, add to the price of the final product.

Flow field design aims at achieving multiple goals such as improving gas and charge transport to the catalyst site, removing excess liquid water from the channel and MEA, achieving appropriate compression and sealing, and maintaining a uniform thermal profile. The most popular and simple flow field designs are parallel and serpentine channels, both of which have their advantages and disadvantages. Parallel channels are more prone to water blockage since reactant gases can easily by-pass blocked channels thereby not allowing the necessary pressure buildup in the channel to remove the liquid water blockage [95]. Serpentine channels, on the other hand, have a long gas flow path leading to substantial pressure drops and gas composition changes along the channel. Interdigitated channels are another common design which incorporates dead-ended inlets and dead-ended outlets that are not connected, forcing the gas through the gas diffusion layer. Although interdigitated channels lead to better liquid water removal from the cell, they exhibit large pressure gradients compared to serpentine and parallel channels and therefore higher parasitic power consumption. For more details on flow field designs, the reader is referred to [96].

Due to reactant, pressure, humidity, and heat variations in the channels, structural land/channel interactions, and complicated geometries, detailed bipolar plates analysis can only be performed with three-dimensional models including transport and structural physical processes. Depending on the goal of the simulation, only a cross-section of the cell may be considered (red rectangle in Figure 2.2). In this case, reactant, heat and pressure drop along the channel are neglected and two-dimensional models are used where the channel reactant concentrations are used as boundary conditions. Through-the-channel models, as they are commonly named, are likely appropriate when operating fuel cells with parallel channels and small active area at high gas flow rates, i.e., high stoichiometry, in order to maintain uniform reactant and product concentration in the channel – a testing condition recently referred to as ‘differential’ condition by Kongkanand and Mathias [20] (supplementary material). If reactant depletion along the channel is of primary concern however, a model considering the green rectangle domain in Figure 2.2 could also be developed, known as an along-the-channel model. This model however ignores land to channel effects, which are important in most fuel cells [30], unless porous plates are used [97].

Mathematical models for mass transport in channels are presented in Section 3.1, including the modeling approaches for liquid water transport in channels in Section 3.1.1.

## 2.2 Gas diffusion and microporous layers

GDLs are responsible for:

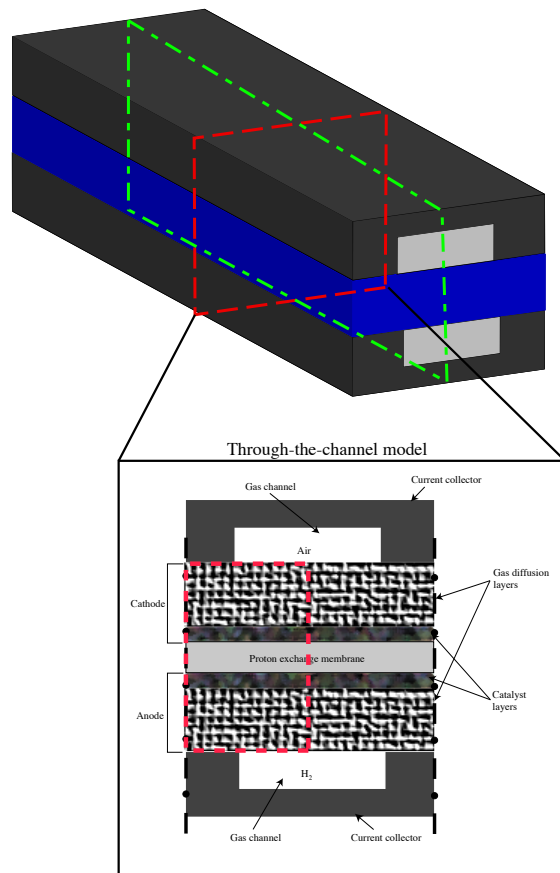


Figure 2.2: A schematic of a single-channel PEMFC. Through-the-channel computational domain is shown in the red rectangle. Along-the-channel computational domain is shown in the green rectangle. Reproduced from [82] with the permission of the author.

- uniform distribution of the reactant gases to the catalyst layer (see mass transport models in Section 3.2);
- transport of water and heat generated in catalyst layers to BPPs (Sections 3.2.3 and 3.5);
- electrical connection between the catalyst layer and current collectors (Section 3.3); and
- improving the mechanical stability of the MEA.

GDLs are 100-500  $\mu\text{m}$  thick porous layers made of an electrically conductive material, such as carbon paper or carbon cloth [98–101]. GDL porosity is between 90 and 70%, depending on manufacturer, type and compression level [102, 103]. Electron transport in GDLs occurs through the solid network of carbon fibers, while reactant and product gases as well as liquid water are transported through the void, or pore, phase of the GDLs. To aid liquid water removal from the cell and avoid flooding, GDLs are impregnated with polytetrafluoroethylene (PTFE) or other hydrophobic materials [98].

The microporous layer, commonly manufactured by intermixing a hydrophobic polymer, e.g., PTFE, with carbon black, is a porous media between the CL and GDL. The role of the microporous layer is still under debate, however it has been shown to reduce fuel cell ohmic resistance, increase fuel cell stability, and enhance performance at high current density, especially under fully humidified conditions [104–111]. Based on these studies, the hypothesized MPL functionality includes:

- increasing the water removal rate [104];
- providing a better electrical contact [105];
- alleviating water accumulation by forcing the liquid water from cathode to anode [107];
- improving the evaporation in the electrodes [110, 111]; and
- creating an in-plane diffusion pathway in the partially saturated layers [110].

In the past decade, durability and degradation of fuel cell materials and components has become a major area of research [21, 112–128]. In GDLs, carbon sites may be oxidized and form hydrophilic regions (this is primarily observed on the cathode side) [21]. This leads to increase in water uptake and, as a result, degraded gas transport. Similar carbon degradation, i.e., corrosion and mass loss, is observed in MPLs [21]. Loss of hydrophobicity may also be attributed to disintegration of PTFE binders in GDLs, which is more significant on the anode side [112].

In addition to the layers themselves, GDL/MPL and CL/MPL interfaces have received a great deal of attention in recent years [33, 129–136]. Imperfect GDL/MPL and CL/MPL interfacial contact may result in not only additional ohmic resistance due to the loss of contact area [130] but also increased mass transport losses due to water accumulation at the interfacial gaps between the layers [131–134].

## 2.3 Catalyst layers

Catalyst layers are responsible for:

- activation of reaction kinetics (see reaction kinetics models in Section 3.4);
- reactant transport (Section 3.2);
- charge transport (Section 3.3); and
- water transport between GDL and PEM (Section 3.2.3).

In order to achieve the functionality above, these layers are composed of three phases: an electronically conductive solid phase (carbon nano-particles with attached catalyst particles, often platinum or platinum-based alloys), an ion conductive phase, also known as ionomer phase (usually a perfluorosulfonic acid ionomer (PFSA) dispersion of varying equivalent weight [137–139]), and a void (pore) phase. The solid phase in the catalyst layer includes the catalyst as well as the supporting particles which transfer the electrons. The catalyst serves the purpose of initiating the electrochemical reaction. During the past decade, a wide variety of catalysts have been developed including: (a) Pt, (b) Pt-based alloys [140], (c) core-shell [141, 142], (d) non-precious metal catalysts [143–145], and (e) shape-controlled nanocrystals [146, 147]. Among them, Pt/C and Pt-based alloys (e.g., PtCo, PtNi) are used in commercial PEMFC products due to the maturity of these technologies [148, 149]. Reducing the amount of catalyst used in PEMFC is still critical to achieve lighter stack weight and lower PEMFCs cost to meet DOE targets [150, 151]. The catalyst

layer thickness is optimized to achieve a high catalyst utilization, resulting in a thickness of 1-20  $\mu\text{m}$ . Experimental studies have shown that the optimal electrolyte loading is between 30 and 40%, however it varies depending on the catalyst loading and operating conditions [152–156].

The optimal catalyst layer design strikes a balance between the fractions of void space, electrolyte loading and solid phase. It is more cost efficient to use a numerical model to perform parametric studies on the catalyst layer compositions. For example, a couple of numerical optimization studies on electrolyte loading have been carried out over the past decades [24, 157–159].

Conceptual models of catalyst layers can be divided into three main categories depending on their complexity: interface models, macro-homogeneous models, and multiscale models. Interface, or zero-thickness, models assume infinitely thin catalyst layers and reaction kinetics are implemented in the model as a boundary condition between GDL (or MPL) and PEM. It is considered that all properties of the catalyst layer are uniform and its effects are negligible or are not of primary interest, e.g., when studying water or heat management in a complete cell [5, 160]. This approach cannot provide an adequate description of the cathode overpotential [161, 162] and is clearly not suitable for catalyst layer optimization.

In macro-homogeneous models, the catalyst layer is simulated as a heterogeneous porous structure made of a solid catalyst support (like carbon), a catalyst, and an electrolyte. Electrochemical reactions occur on the surface of the catalytic particles that are sitting on larger supporting particles. All reactants and products need therefore to travel through the catalyst layer to reach or leave those reaction sites. In cathode CLs, electrons are transported through the catalyst and support particles, protons through the ionomer, and oxygen travels through the void space. These transport processes are modeled using a volume-averaged approach with effective transport parameters obtained either by experiments or microscale simulations.

Models that account for both macro- and micro-structure features in the catalyst layer are labeled here multiscale models. The key idea of multiscale models is to account not only for reactant and charge transport within the catalyst layer using a volume-average approach, but also to include some detail of the local transport processes occurring at the catalyst particle using an idealized model of the local processes. Then, the volume-average model and the local models are coupled via the reaction source term. Based on early scanning electron microscopy imaging, a local reaction model idealization was developed to account for observed mass transport losses in the microscale. It was assumed that the carbon particles formed large spherical aggregates of 0.5 to 2  $\mu\text{m}$  and these carbon aggregates were idealized as a spherical porous catalyst with the pores inside the catalyst filled with ionomer [163–167]. Further refinements to this idealization included covering the agglomerates with ionomer thin films [44, 162, 168–170] and water films [171–173] to further enhance mass transport limitations, as well as replacing the ionomer in the pores by liquid water [174, 175]. Electrochemical reactions in agglomerates were then modeled similarly to those in porous electrodes [176]: oxygen is first transported through the gas pores (macro-scale transport), it then dissolves and is transported through the electrolyte/water films around the agglomerate, diffuses through the agglomerate filling, and finally reaches the reaction sites. A detailed comparison of the suggested agglomerate structures and their effects on fuel cell performance can be found in [175].

Recent experimental [53, 177–179] and numerical [53, 180] studies suggest that catalyst support particles arrange into aggregates, but these aggregates are much smaller than those used in previous modeling work, i.e., in the range of 25-200 nm instead of 500-2000 nm [170], and that are only partially covered by an ionomer thin film [57, 181]. Further, given the heterogeneous surfaces in the catalyst layer, it is unlikely a uniform water film will cover these small aggregates. Once agglomerate sizes are reduced to those observed experimentally, bulk ionomer transport values no longer can explain the decrease in performance observed experimentally in conventional, and particularly low loading electrodes [18, 27, 49, 182, 183]. Oxygen transport measurements through ionomer thin films supported on platinum [182, 183], and micro-scale simulation results [18] show negligible local transport limitations in the gas phase suggesting that transport through the ionomer covering the catalyst particles is the key parameter limiting performance at the local reaction site. If this is the case, a more realistic idealization at the local scale would be the use of a single particle (30-70 nm [177]) or several particles (100-150 nm [178]) covered by an ionomer film with transport properties that are different from those from bulk ionomer, as highlighted by Owejan et al. [49] who stated that ionomer transport properties would have to be an order of magnitude lower to explain the performance degradation observed in low loading electrodes. A simple, yet more realistic idealization of the catalyst layer is, for example, the ionomer covered catalyst particle (ICCP) model [175, 184] which considers a single catalyst carbon particle with smaller platinum particles evenly residing on its surface, all covered with a thin ionomer film [175]. A similar model by Hao et al. [158] takes into account oxygen transport through a water film that covers the ionomer surface. The ICCP model is provided as an example. This idealization might only be valid from some carbon supports, e.g., low surface area carbon such as Vulcan [179, 185], and it might not be valid for other types of carbon such as high surface area carbons. Local idealizations that are physically meaningful and yet computational easy to implement and solve are still required. These should be obtained based on catalyst, catalyst support and catalyst

layer microstructure and composition.

The models discussed above are valid at beginning of life (BOL), however the catalyst layer will undergo degradation during operation. Models are required to understand these processes. Even though such models are not included in this entry, a basic overview on degradation mechanisms is provided for completeness in the next paragraphs. A number of experimental studies have highlighted two key mechanisms of catalyst layer degradation: a) loss of the electrochemically active surface area (ECSA) due to platinum particle coarsening [21, 113–115, 117, 186, 187]; and b) carbon corrosion [120, 188–190]. Even though the exact Pt dissolution mechanism remains unclear [187], three pathways leading to platinum particle coarsening have been identified: 1) Ostwald ripening, where small particles dissolve, diffuse and redeposit into larger particles, 2) dissolution and re-precipitation into newly formed particles often inside the membrane, and 3) particle coalescence, where two particles in close proximity sinter to form one large particle with lower surface energy [21]. Pt degradation is often approximated with thermodynamic and kinetic models of the reactions of interest, such as platinum dissolution and oxide growth, together with a particle size distribution that evolves over time. Examples of kinetic models to study platinum degradation can be found in references [21, 113, 114, 118, 186, 191–196]. Very few attempts have been made to integrate Pt dissolution models in an MEA model. Franco and Tembeley [192] developed a 0D+1D model of the whole MEA for modeling aging mechanisms in a PEMFC cathode.

Carbon corrosion kinetic models have also been developed and, unlike platinum degradation models, they have been integrated into MEA models. Meyers and Darling [119] and Fuller and Gray [197] developed carbon degradation models in 1D and 2D, respectively, in which a Butler-Volmer kinetics model and a cathodic carbon oxidation reaction (in addition to the common PEMFC kinetics) were incorporated (Meyers and Darling [119] used Tafel kinetics for carbon corrosion). Although these models are able to quantify the effect of operating conditions on carbon corrosion, they neglect the instantaneous performance change due to degradation. Franco and Gerard [121] proposed an improved multiscale model (based on the model from [192]) that was capable of predicting the instantaneous performance feedback to carbon aging, e.g., cathode catalyst layer thinning, decrease of platinum surface area in it, and increase in CL-GDL contact resistance. With that model, it was possible to analyze the effect of catalyst layer composition and operating conditions on carbon mass loss during the fuel cell operation. The model by Franco and Gerard has several simplifying assumptions, such as isothermal conditions, single phase and no coupling between carbon corrosion and electrode structure, however, it is a starting point for the implementation of carbon corrosion into more sophisticated mathematical models. The kinetic mechanism of carbon corrosion was recently improved by Pandey et al. [120], who suggested several multi-step reaction mechanisms at different zones around the platinum particle on the support.

## 2.4 Polymer electrolyte membrane

Polymer electrolyte membranes used in PEMFCs usually belong to the perfluorosulfonic acid (PFSA) family of polymer membranes such as Nafion<sup>®</sup> and Aquivion<sup>®</sup>. Their key functions include:

- acting as an electrical insulator separating anode and cathode sides of the cell;
- preventing reactant crossover between the two halves of the cell; and
- acting as a protonic conductor to provide means for hydrogen protons to reach the cathode.

An accurate representation of the membrane in a model is required for good approximation of ohmic losses and water transport. Ohmic losses are associated with the protonic conductivity of the membrane, which depends on its hydration level. Efficient water management in the fuel cell is required to maintain the membrane and ionomer in the catalyst layers hydrated while removing excessive liquid water.

Most PEM mathematical models consider transport of only two components, protons and water (in liquid or sorbed form), neglecting any reactant crossover that can happen between the electrodes. In PEM fuel cells, crossover effects are usually insignificant; however, they must be taken into account if the model is designed for durability studies.

Proton transport is predominantly modeled with either Nernst-Planck [198–202] or simpler Ohm’s law-based [40, 61, 63–71, 73, 76, 78, 203–209] equations, in which the transport parameters, e.g., protonic conductivity, depend on the membrane water content  $\lambda$ , a ratio of the number of moles of sorbed water to the number of moles of sulfonic groups in the PEM. The simplest models assume that the membrane is always fully hydrated and exhibits its peak protonic conductivity.

An accurate representation of polymer electrolyte membrane requires a model that takes into account water transport, which can be approximated as a diffusion [1] or a hydraulic process [2, 201]. In the former, the membrane

is assumed to be a homogeneous and nonporous material, in which water is transported by diffusion and electro-osmotic drag. Hydraulic models, on the other hand, suggest that the membrane has two phases, the polymer phase and the pore phase that is filled with liquid water. These models also consider electro-osmotic drag, but the other driving force is associated with a pressure gradient. Schlögl's equation is used in such models to compute the liquid water velocity [5]. Applicability of either of the two models might depend on the hydration level of the membrane. Diffusion models appear to be suitable for dry membranes while hydraulic models might be applicable when the membrane is saturated [210, 211]. An approach that is valid for both cases is thus a better choice for fuel cell modeling. An example of such models can be found in [210, 212]. More recent models are designed in a way that allows them to couple protonic and water transport [213].

Constantly changing temperature and humidity conditions during the typical operation of a fuel cell lead to hydrothermal cycling loading of the membrane and directly affect its durability by significant mechanical stress development and pinhole and crack formation, as shown by visco-plastic, elasto-plastic, and viscoelastic-plastic studies [123–125]. Polymer electrolyte membranes can degrade not only mechanically, but also chemically through  $\cdot\text{OH}$  and  $\cdot\text{H}$  radical formation and side chain decomposition [126, 127]. Examples of proposed models for membrane degradation are provided in references [126, 127]. A detailed review on membrane properties and degradation mechanisms was recently provided by Kusoglu and Weber [139].

### 3 General models

#### 3.1 Mass transport in channels

Multi-component gas transport in fuel cell channels is governed by mass, momentum, and energy conservation equations. Most mathematical models, with the exception of the generalized model by Kerkhof et al. [214, 215], formulate this problem using mass, momentum, and energy conservation equations for the gas mixture, and  $N - 1$  combined mass and momentum conservation equations for the  $N$  individual species [176, 216].

The mass conservation equation for the gas mixture is [217, 218]

$$\frac{\partial \rho}{\partial t} + \nabla \cdot (\rho \mathbf{v}) = S, \quad (3.1)$$

where  $\rho$  is the density of the gas mixture,  $t$  is time,  $\mathbf{v}$  is the mass averaged velocity of the mixture, and  $S$  is a source term that combines the consumption and/or production of each species in the gas mixture. Due to the consumption of reactants, the density of the mixture will not be constant along the channel and a compressible form of the mass conservation equation should be used [5, 160, 219], however, several articles [32, 220–223] assume the density changes are negligible and then, the incompressible form of the mass conservation is used.

The momentum conservation equation is the result of applying Newton's second law to a fluid particle in motion. For the gas mixture, it is given by

$$\frac{\partial}{\partial t} (\rho \mathbf{v}) + \nabla \cdot (\rho \mathbf{v} \otimes \mathbf{v}) = \nabla \cdot \hat{\boldsymbol{\tau}} + \rho \mathbf{g} + \mathbf{F}, \quad (3.2)$$

where the operator  $\otimes$  stands for the tensor product,  $\hat{\boldsymbol{\tau}}$  is the Cauchy stress tensor,  $\mathbf{g}$  is gravity vector field, and  $\mathbf{F}$  is a momentum source term, which is equal to zero for one species transport in gas channels. For a Newtonian fluid, the Cauchy stress tensor is given by

$$\hat{\boldsymbol{\tau}} = -(p - \lambda_b \varepsilon_V) \mathbf{I} + 2\mu \mathbf{D}, \quad (3.3)$$

where  $p$  is pressure,  $\lambda_b$  is the bulk viscosity,  $\varepsilon_V = \nabla \cdot \mathbf{v}$  is the volumetric strain rate,  $\mathbf{I}$  is the identity tensor,  $\mu$  is the dynamic viscosity, and  $\mathbf{D} = \nabla_s \mathbf{v} = \frac{1}{2} (\nabla \mathbf{v} + \nabla^T \mathbf{v})$  is the strain rate tensor. The viscosity of the mixture is given by Chapman-Enskog theory [176, 224, 225]:

$$\mu = \sum_{i=1}^N \frac{x_i \mu_i^0}{\sum_{j=1}^N x_j \xi_{ij}}, \quad (3.4)$$

where  $x_i$  is the molar fraction of species  $i$ ,  $\mu^0$  is the viscosity of a pure substance, and  $\xi$  is the Lennard-Zones interaction parameter [224]. If, in order to simplify the equations, the density of the fluid mixture is assumed constant, the Cauchy stress tensor for an incompressible fluid yields

$$\hat{\boldsymbol{\tau}} = -p \mathbf{I} + \mu (\nabla \mathbf{v} + \nabla^T \mathbf{v}). \quad (3.5)$$

The first term in equation (3.5) represents the hydrostatic pressure acting on the considered particle, whereas the latter indicates its rate of strain. Combination of equations (3.1), (3.2), and (3.3) results in the Navier-Stokes equations for a compressible fluid.

The energy transport equation for an ideal gas is given by [176],

$$\hat{C}_p \frac{D(\rho T)}{Dt} = \nabla \cdot (k \nabla T) + \frac{Dp}{Dt} + Q, \quad (3.6)$$

where  $\hat{C}_p$  is the specific heat,  $T$  is temperature,  $k$  is the thermal conductivity,  $p$  is pressure, and  $Q$  is a volumetric heat source. However, the vast majority of models that analyze mass transport in fuel cell channels [32, 219–222, 226–234] consider the fluid to be isothermal and, therefore, this equation is not solved.

The transport of individual species is described using a combined mass and momentum conservation for the individual species. This equation can be formulated for each species  $i$  as

$$\frac{\partial \rho_i}{\partial t} + \nabla \cdot \hat{\mathbf{N}}_i = S_i, \quad (3.7)$$

where  $\rho_i$  is the density of species  $i$ ,  $\hat{\mathbf{N}}_i = \rho_i \mathbf{v}_i$  is the mass flux of species  $i$ ,  $\mathbf{v}_i$  is the velocity of species  $i$ , and  $S_i$  is the source term. Neglecting external body forces, the velocity for all  $N - 1$  species can be obtained using the Maxwell-Stefan equations, i.e., [216]

$$\nabla x_i + (x_i - \omega_i) \frac{\nabla p}{p} = - \sum_{i \neq j}^N \frac{x_i x_j}{\mathcal{D}_{ij}} (\mathbf{v}_i - \mathbf{v}_j). \quad (3.8)$$

where  $\omega_i$  is the mass fraction of species  $i$ , and  $\mathcal{D}_{ij}$  is the binary diffusion coefficient between species  $i$  and  $j$ . Maxwell-Stefan equations account for interactions between species. The model is capable of predicting reverse diffusion, osmotic diffusion, and diffusion barrier effect [216]. The density and velocity for each species can be obtained combining mass and momentum equations for the mixture,  $N - 1$  mass conservation and Maxwell-Stefan (momentum conservation) equations with the following closure equations:

$$\rho = \sum_{i=1}^N \rho_i, \quad (3.9)$$

$$\mathbf{v} = \sum_{i=1}^N \omega_i \mathbf{v}_i, \quad (3.10)$$

$$x_i = \omega_i \frac{\sum_{k=1}^N M_k x_k}{M_i}, \quad (3.11)$$

where  $M_i$  is the molar mass of species  $i$  and  $\mathbf{v}$  is the mass-averaged velocity of the mixture. Assuming negligible pressure changes, equation (3.8) can be re-arranged in order to obtain an explicit expression for the species mass fluxes such that [216]

$$\hat{\mathbf{N}}_i = \sum_{j=1}^N \hat{D}_{ij} \nabla x_j. \quad (3.12)$$

where tensor  $\hat{D}$  is a function of molecular diffusion coefficients and composition of the mixture. For infinitely dilute species and negligible velocities, the equation above becomes Fick's law of diffusion and equation (3.7) becomes Fick's second law of diffusion:

$$\frac{\partial \rho_i}{\partial t} = \nabla \cdot (\rho \mathcal{D}_{ij} \nabla \omega_i) + S_i, \quad (3.13)$$

where  $i$  is the solute and  $j$  is the solvent. The binary diffusivity  $\mathcal{D}_{ij}$  can be estimated using Chapman-Engskog theory [176]:

$$\mathcal{D}_{ij} = \frac{188.29 T^{3/2}}{p \Lambda_{ij}^2 \Omega_D^*} \sqrt{\frac{1}{M_i} + \frac{1}{M_j}}, \quad (3.14)$$

where  $T$  is temperature,  $\Lambda_{ij}$  is the collision diameter of a binary mixture,  $\Omega_D^*$  is a correction factor, and  $M_i$  is the molar mass of species  $i$ . The collision diameter  $\Lambda_{ij}$  is obtained as the average of the collision diameters  $\Lambda_i$  and  $\Lambda_j$  of species  $i$  and  $j$ :

$$\Lambda_{ij} = \frac{1}{2}(\Lambda_i + \Lambda_j). \quad (3.15)$$

The most common method for solving the set of equations (3.1), (3.2), and (3.6) is the finite volume method [235], which has been implemented in many commercial numerical simulation packages, such as ANSYS Fluent [236], and STAR-CCM+ [237], as well as some open-source software, e.g., OpenFOAM [238]. An alternative approach is the finite element method [239], which is available in commercial packages such as COMSOL Multiphysics [240], and in open-source frameworks such as Kratos Multiphysics [241] and deal.ii [242].

### 3.1.1 Two-phase flow in channels

In order to numerically reproduce two-phase flow in fuel cell channels, the model presented in Section 3.1 needs to be extended. There are two approaches in literature to study two-phase flow in fuel cell channels: analytical and numerical models. The former approach has been taken by several authors [243–245], but usually these models are an oversimplification of the phenomena and, therefore, are not considered here.

Numerical models use Navier-Stokes and continuity equations to model the mass transport of both gas and liquid phases. The main challenges of two-phase flow models are:

- identification of the interface between both phases;
- taking into account the changes in the material properties (i.e., density and viscosity);
- representation of the discontinuity of flow variables, i.e., velocity and pressure;
- modeling surface tension and wetting phenomena.

The difference between models basically resides in the chosen kinematic framework. Fixed-grid models use the Eulerian formulation to model both air and water. However, they must include additional techniques to track or reconstruct the interface between the phases. Moving-mesh models use the Lagrangian formulation, allowing to track the air-water interface exactly. In those methods, the numerical domain has to be continuously re-meshed, which can be computationally expensive. An alternative to the previous models is a combination of fixed and moving grids, often referred to as embedded formulations, which have been extensively used in the fluid-structure interaction (FSI) community and have been proven to be a promising method for multi-fluid problems.

Fixed-grid models are the most used methods to solve two-phase problems. The most know fixed-grid method is the volume of fluid (VOF) method, which is a front-capturing technique. It was developed by Hirt and Nichols [246] and, together with equations (3.1) and (3.2) for both gas and liquid, includes an additional equation for convecting the interface volume fraction variable  $C_k$ :

$$\frac{\partial}{\partial t} (C_k \rho_k) + \nabla \cdot (C_k \rho_k \mathbf{v}_k) = 0, \quad (3.16)$$

where  $\rho_k$  and  $\mathbf{v}_k$  are the density and the velocity of the fluid  $k$ , respectively. The volume fraction variable,  $C_k$ , takes the value 0 for the nodes outside the fluid  $k$ , 1 inside the fluid, and between 0 and 1 when the considered element contains the interface between two fluids. In the case of two fluids therefore only one equation needs to be solved and  $C_k$  is usually replaced by  $S$ . Piecewise linear interface calculation (PLIC) techniques [247, 248] are the most used nowadays and have been included in commercial codes [249]. Figure 3.1 shows a possible distribution of obtained  $C_k$  values in a fixed mesh using the VOF. Cells with a  $C_k$  value between 0 and 1 contain the interface between the two phases, as shown on the right-hand side mesh after interface reconstruction using PLIC technique.

In order to include surface tension effects, an additional force term is added to the right-hand side of equation (3.2). The majority of existing commercial codes, such as ANSYS Fluent [236], COMSOL Multiphysics [240], or STAR-CCM+ [237], use the continuum surface force (CSF) model [250], in which the surface tension is evaluated at the historical time step of the transient problem (i.e., the model is explicit in time). The expression for the surface tension force is

$$\mathbf{f}_{st} = \gamma \rho \hat{\kappa} \frac{\nabla C_k}{0.5(\rho_l + \rho_g)}, \quad (3.17)$$

where  $\gamma$  is the surface tension coefficient,  $\rho_l$  and  $\rho_g$  are the densities of liquid and gas phases, respectively, and  $\hat{\kappa}$  is the curvature of the air-water interface defined as the divergence of the unit normal to the interface:

$$\hat{\kappa} = \nabla \cdot \frac{\mathbf{n}}{\|\mathbf{n}\|}, \quad (3.18)$$

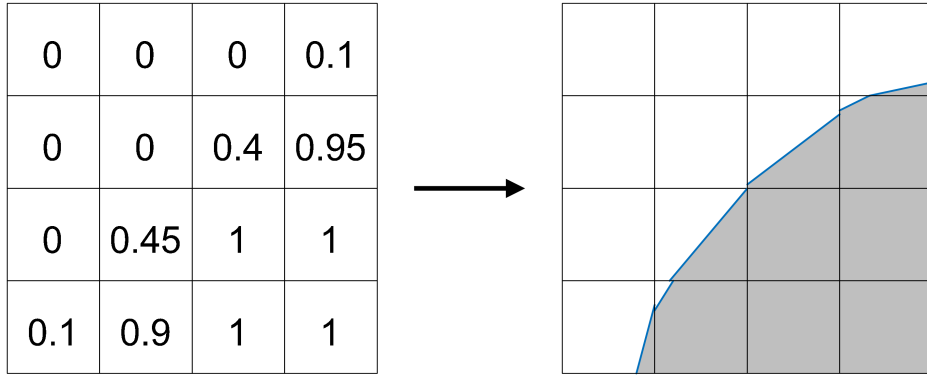


Figure 3.1: Schematic representation of obtained  $C_k$  values in a fixed mesh using the VOF, and interface reconstruction using PLIC technique [247, 248].

where the normal vector is related to the volume fraction  $C_k$  through

$$\mathbf{n} = \nabla C_k. \quad (3.19)$$

An alternative to the CSF model is the continuum surface stress (CSS) model, developed by Lafaurie et al. [251]. The surface tension term has the following expression:

$$\mathbf{f}_{st} = \nabla \cdot \left( \gamma \left( \|\nabla C_k\| \mathbf{I} - \frac{\nabla C_k \otimes \nabla C_k}{\|\nabla C_k\|} \right) \right), \quad (3.20)$$

where  $\otimes$  denotes the tensor product. The CSS model has several advantages over the CSF model: it is conservative and it does not require the computation of the curvature  $\hat{\kappa}$ . Moreover, it can be used to solve problems with variable surface tension, whereas CSF model cannot account for this effect.

Earlier studies of droplet dynamics in fuel cell channels include the works by Golpaygan and Ashgriz [226, 252], and Shirani and Masoomi [253]. In these studies, the contact line was fixed and no validation was provided. Other studies analyzed the problem in 3D [227–229, 254–257], however, validation was again not provided and the droplets were placed in the channel domain *a priori* without any particular criteria. The first studies using VOF that included experimental validation in their study were the works of Theodorakakos et al. [258] and Bazylak et al. [231].

Le and Zhou [259] implemented a model in ANSYS Fluent that integrated a multi-component, non-isothermal two-phase flow in the channel and GDL with a CL model including electrochemical reactions. The water distribution in the model was qualitatively validated by visual comparison to experimental results, however, no quantitative validation was provided regarding water distribution or cell performance, and the model could not predict water formation in the MEA and posterior emergence into the channels. Instead, they started their simulations with several droplets distributed along the serpentine channels. A review on the application of VOF to the PEMFC field was recently provided in [249].

The level set (LS) method is another fixed-grid technique that was presented by Osher and Sethian in 1988 [260] as a general technique to capture a moving interface. The basic idea of the level set method is to represent the interface by the zero level set of a smooth scalar function  $\phi(\mathbf{x})$  [261], [262]:

$$\phi(\mathbf{x}) : \mathbb{R}^n \longrightarrow \mathbb{R} \quad \Gamma = \{x : \phi(\mathbf{x}) = 0\}. \quad (3.21)$$

The position of the interface is known implicitly by the nodal values of  $\phi$ : nodes with positive values are inside the fluid, whereas negative values mark nodes outside the fluid domain, as shown in Figure 3.2. The position of the interface is then obtained by interpolation of nodal values of function  $\phi$ . The LS method has the advantage of being capable of handling topological changes and complex shapes of the interface. It may, however, give inaccurate results for normal vector and interface curvature, and it also fails at mass conservation. Additional techniques to alleviate these drawbacks have been reported in literature [263], [264–268].

The embedded formulation combines Lagrangian and Eulerian descriptions for the liquid and the gas phases, respectively. The method was proposed in [269] and [270] and was extended later for surface tension-dominated problems in [233] and [234]. The main advantage of this method is that it allows tracking of the interface between air and water, which is critical in surface tension-dominated problems, such as droplet shedding in fuel cell channels. The gas is modeled using the Eulerian formulation, which is the most natural approach, whereas the liquid phase

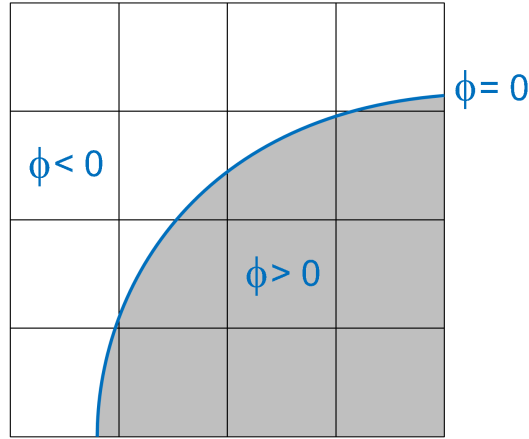


Figure 3.2: Schematic representation of function  $\phi(\mathbf{x})$  representing the interface in the LS method.

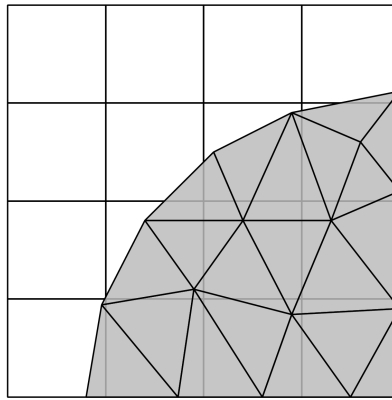


Figure 3.3: Schematic of the moving mesh, representing the liquid domain, overlapped with the fixed mesh, representing the gas domain, in the embedded method.

is described using a Lagrangian formulation. The embedded model does not require mesh refinement around the interface to avoid numerical diffusion, contrary to fixed-grid methods. The liquid domain has to be re-meshed in order to update its configuration. Since the water domain usually represents a small fraction of the total domain in fuel cell channels, however, the cost of re-meshing is reduced.

Figure 3.3 shows a schematic representation of the two meshes used in this method. Since the liquid domain is discretized using a moving mesh embedded into the fixed mesh of the gas domain, a coupling technique must be implemented. The overall solution strategy is:

1. solve the problem in the moving mesh, i.e., liquid domain, obtaining velocity and pressure;
2. identify the position of the interface in the fixed mesh;
3. project the velocity of the boundary nodes in the moving mesh onto the the nodes of the fixed mesh representing the interface;
4. use this velocity as a Dirichlet boundary condition to solve the problem in the fixed mesh, obtaining velocity and pressure;
5. use the solution of the fixed mesh to project the whole stress onto the boundary of the moving mesh;
6. repeat.

Jarauta et al. [233] showed that the model can accurately describe wetting phenomena on rough surfaces and droplet oscillation in channels. Effects of surface energy and roughness were validated by showing good agreement between experimental and numerical predictions of advancing and receding contact angles of droplets of varying sizes

on different substrates and inclined planes. It was also shown that sessile droplets on smooth hydrophobic surfaces, such as PTFE, are more prone to detachment than on rough surfaces, such as GDLs, where droplets experience large deformations before detachment due to the effect of contact line pinning. The model was also able to capture the recirculating pattern observed experimentally in sessile droplets subjected to an airflow [271].

## 3.2 Mass transport in MEAs

### 3.2.1 Gas transport

In porous media, the mass and momentum transport equations of gaseous mixtures (3.1) and (3.2) need to be volume averaged [225] and a source term,

$$\mathbf{F} = -\left(\mu\hat{\mathbf{K}}^{-1}\varepsilon_v\mathbf{v} + \hat{\beta}\rho\varepsilon_v^2|\mathbf{v}|\mathbf{v}\right), \quad (3.22)$$

representing solid-fluid interactions needs to be added to the momentum equation. In the equation above,  $\varepsilon_v$  is the porosity of the porous media,  $\hat{\mathbf{K}}$  is the permeability tensor,  $\mathbf{v}$  represents the interstitial (intrinsic) mass-averaged velocity vector of the mixture, and  $\hat{\beta}$  is the Forchheimer correction tensor. Equation (3.1) then results in [225]:

$$\frac{D(\rho\mathbf{v})}{Dt} - \nabla \cdot \mu(\nabla\mathbf{v} + \nabla^T\mathbf{v}) + \nabla p + \nabla\left(\frac{2}{3}\lambda_b\varepsilon_v\right) = \rho\mathbf{g} - \left(\mu\hat{\mathbf{K}}^{-1}\varepsilon_v\mathbf{v} + \hat{\beta}\rho\varepsilon_v^2|\mathbf{v}|\mathbf{v}\right). \quad (3.23)$$

where  $\rho$  is the phase (superficial) averaged density.

If inertia and viscous effects are assumed to be negligible in the porous media, along with gravity effects, and assuming steady state, equation (3.23) becomes the Darcy-Forchheimer law of momentum transport in porous media:

$$\nabla p = -\left(\mu\hat{\mathbf{K}}^{-1}\varepsilon_v\mathbf{v} + \hat{\beta}\rho\varepsilon_v^2|\mathbf{v}|\mathbf{v}\right). \quad (3.24)$$

If the porosity is higher than 0.6 [272], and if viscous effects cannot be neglected, Brinkman's equation must be used instead:

$$\nabla p = -\left(\mu\hat{\mathbf{K}}^{-1}\varepsilon_v\mathbf{v} + \hat{\beta}\rho\varepsilon_v^2|\mathbf{v}|\mathbf{v}\right) + \hat{\mu}\nabla^2\varepsilon_v^2\mathbf{v}, \quad (3.25)$$

where  $\hat{\mu}$  is the effective diffusivity [272]. At low velocities, the second term in equation (3.24) can be neglected, giving Darcy's law [5, 32, 164]:

$$\nabla p = -\mu\hat{\mathbf{K}}^{-1}\varepsilon_v\mathbf{v}. \quad (3.26)$$

For the mass transport of individual species, one option relies on solving the volume-averaged mass and momentum mixture equations, and mass and momentum conservation volume-averaged equations for  $N-1$  of the considered species, i.e., equations (3.7) and (3.8). As shown in Section 3.1, mass transport can be modeled using either Fick's law of diffusion or Maxwell-Stefan equations for multi-component mass transport. An additional momentum conservation model for multi-component mixtures that accounts for porous media-particle interactions is the dusty gas model (DGM) [224, 225, 273]:

$$\frac{1}{RT}\nabla p_i = \sum_{i=1}^N \frac{x_i\mathbf{N}_j - x_j\mathbf{N}_i}{D_{ij}^{\text{eff}}} - \frac{\mathbf{N}_i}{D_i^K}, \quad (3.27)$$

where  $R$  is the universal gas constant,  $D_{ij}^{\text{eff}}$  is the effective molecular diffusivity between species  $i$  and  $j$ , and  $D^K$  is the Knudsen diffusion coefficient, which is discussed later in this Section. Although this model is considered an extension of Maxwell-Stefan equations, Kerkhof [274] pointed out that the model takes viscous forces into account twice and, therefore, is incorrect. In his work, Kerkhof proposed the binary friction model (BFM) based on Lightfoot's friction model [275]. The governing equation for the binary friction model is given by [224, 225, 274]

$$\frac{1}{RT}\nabla p_i = \sum_{i=1}^N \Phi_{ij} \frac{x_i\mathbf{N}_j - x_j\mathbf{N}_i}{D_{ij}^{\text{eff}}} - \left(D_i^K + \frac{\hat{\mathbf{K}}}{\bar{\kappa}_i}\right)^{-1} \mathbf{N}_i, \quad (3.28)$$

where the coefficient  $\Phi$  is equal to one in the continuum region and zero in Knudsen region [224], and  $\bar{\kappa}$  is the partial viscosity. Pant et al. [224] proposed a modified binary friction model (MBFM) in order to make it valid for mass transport in capillaries.

An alternative model to solving volume-average equations for the mixture and  $N-1$  species, is to use the model proposed by Kerkhof and Geboers [214, 215] for all species. In this case, the momentum conservation equation for each species is extended to include a term that accounts for the interaction between species:

$$\frac{D}{Dt}(\rho_i \mathbf{v}_i) = \nabla \cdot \hat{\boldsymbol{\tau}}_{ij} + \rho \mathbf{g} + \mathbf{F} + \mathbf{D}_i, \quad (3.29)$$

where the term  $\mathbf{D}_i$  is given by

$$\mathbf{D}_i = \sum_{j=1}^N \frac{p_i p_j}{p D_{ij}^{\text{eff}}} \hat{\mathbf{I}} (\mathbf{v}_j - \mathbf{v}_i), \quad (3.30)$$

and where  $\hat{\mathbf{I}}$  is the identity tensor. The term  $\mathbf{D}_i$  accounts for friction effects between species. The option of solving equations (3.7), (3.29) for each species was adopted in references [225, 276]; however, this leads to a computationally intensive model [225]. To date, there is only one study in literature that includes an implementation of the model by Kerkhof and Geboers in porous media [225]. This is still an active area of research [224, 225, 277–280].

The vast majority of models that study mass transport of gaseous species in the porous media consider Navier-Stokes equations for the gas mixture, and then use Fick's law (equation (3.13)) or Maxwell-Stefan (equation (3.8)) models for the mass transport of individual species. Quan et al. [256, 257] and Gurau et al. [32] modeled the transport of species in the porous media under a serpentine channel using the Navier-Stokes equations, including a Darcy source term for the momentum transport. A similar approach was taken by Le et al. [259, 281–283], but the transport of individual species was modeled using Fick's equation (3.7). Other studies have considered the same governing equations [4, 219–222]. Berning et al. [5, 160] also used Navier-Stokes equations for mass transport in the channel, however they considered Darcy's law in the porous media together with Maxwell-Stefan equations for the transport of individual species.

In order to apply any of the aforementioned models in porous media, permeability and effective diffusion coefficients need to be obtained. Semi-empirical correlations are commonly used to estimate these coefficients based on the morphology, porosity and tortuosity of the material, where the expression constants are obtained by fitting the semi-empirical results to experimental values.

A commonly used expression for gas permeability of GDLs is the Carman-Kozeny equation given as [284]

$$\hat{K} = \frac{d_f^2 \varepsilon_v^3}{16 k_{CK} (1 - \varepsilon_v^2)}, \quad (3.31)$$

where  $d_f$  is the fiber diameter, and  $k_{CK}$  is known as the Carman-Kozeny constant which is considered as a fitting parameter that is obtained experimentally. References [45, 285–294] provide the value of these empirical constants for several GDLs. The permeability of several MPL materials was also estimated in some of the references above, e.g., [292].

The effective diffusion coefficient of dry GDLs and dry CLs can also be estimated using appropriate semi-empirical equations that relate effective molecular diffusivity to bulk molecular diffusivity, porosity and tortuosity of the porous material. One commonly used method to estimate effective diffusion coefficients is using percolation theory, where the effective diffusion coefficient,  $D_{ij}^{\text{eff}}$ , is computed based on the bulk diffusion coefficient,  $\mathcal{D}_{ij}$ , as [43, 170]

$$D_{ij}^{\text{eff}} = \mathcal{D}_{ij} \left( \frac{\varepsilon_v - \varepsilon_p}{1 - \varepsilon_p} \right)^\mu \Theta(\varepsilon_v - \varepsilon_p), \quad (3.32)$$

where  $\varepsilon_p$  is the so-called percolation threshold,  $\mu$  is an exponent that depends on the material structure, and  $\Theta(x)$  is the Heaviside step function. When  $\varepsilon_v < \varepsilon_p$ , no transport occurs.

An alternative to the previous approach is the tortuosity model, where the effective diffusion coefficient,  $D_{ij}^{\text{eff}}$ , is computed based on the bulk diffusion coefficient,  $D_{ij}$ , with the random walk method [295]:

$$D_{ij}^{\text{eff}} = \frac{\varepsilon_v}{\tau} D_{ij}, \quad (3.33)$$

where the tortuosity of the phase  $\tau$  is given by the generalized Archie's law [284, 296]:

$$\tau = \left( \frac{1 - \varepsilon_p}{\varepsilon_v - \varepsilon_p} \right)^\alpha. \quad (3.34)$$

The resulting equation for the effective diffusion coefficient is

Table 3.1: Source terms for oxygen and water electrochemical reaction.

Parameters	GDL	CCL	ACL	PEM
$S_{H_2}$	0	0	$-\frac{i}{2F}$	0
$S_{O_2}$	0	$-\frac{i}{4F}$	0	0
$S_w$	0	$\frac{i}{2F}$	0	0

$$D_{ij}^{\text{eff}} = \frac{\varepsilon_v}{\left(\frac{1-\varepsilon_p}{\varepsilon_v-\varepsilon_p}\right)^\alpha} D_{ij}, \quad (3.35)$$

where the exponent  $\alpha$  depends on the material structure. These models can be used to describe transport in various structures depending on the parameter used from fibrous structures [284] to randomly distributed cylindrical and spherical particles [297]. For example, setting  $\varepsilon_p = 0$  results in Archie's law,  $\tau = \varepsilon^{-\alpha}$ , and two particular cases of Archie's law are the Bruggeman model for transport in porous media with randomly distributed cylindrical and spherical particles. Respectively, those correspond to  $\alpha = 1$  ( $\tau = \varepsilon^{-1}$ ) and  $\alpha = 0.5$  ( $\tau = \varepsilon^{-0.5}$ ) [297]. The Heaviside step function,  $\Theta(x)$ , may be used in equation (3.35) to limit transport for the case  $\varepsilon_v < \varepsilon_p$ . References [45, 48, 294, 298–301] have fitted some of these expressions to experimental data for different GDL, MPL and CL materials and provided estimates for the different empirical constants. Pore-scale numerical modeling can also be used to provide estimates of effective transport properties, e.g., [18, 302].

For porous media where the Knudsen number, i.e., the ratio between the mean free path of the molecules and the pore diameter, is large (approx. larger than 0.1), Knudsen diffusion should be considered in addition to bulk diffusion [30, 51, 303, 304]. In the GDL, the pore sizes are large enough that Knudsen diffusion does not need to be considered; however, it becomes more important in MPL and CLs, where pore sizes are smaller as recently demonstrated experimentally in the case of MPLs by Pant et al. [291] and Carrigy et al. [292]. The Knudsen diffusion coefficient of species  $\alpha$ ,  $D_\alpha^K$ , can be estimated as:

$$D_\alpha^K = \frac{2r_p}{3} \sqrt{\frac{8RT}{\pi M_\alpha}}, \quad (3.36)$$

where  $r_p$  is the pore radius. An effective pore radius for MPLs was estimated experimentally in [291, 292].

When the aforementioned equations are applied to model mass transport in fuel cells, source terms  $S_i$  must be included in order to account for mass variations due to the electrochemical reactions. For instance, if mass transport in the MEA is modeled using Fick's law, the governing equations for oxygen and water vapor molar fractions are:

$$\varepsilon_v \frac{\partial c_{O_2}}{\partial t} - \nabla \cdot (c D_{O_2}^{\text{eff}} \nabla x_{O_2}) = S_{O_2} \quad (3.37)$$

$$\varepsilon_v \frac{\partial c_w}{\partial t} - \nabla \cdot (c D_w^{\text{eff}} \nabla x_w) = S_w. \quad (3.38)$$

Equation (3.38) needs to be modified if water sorption/desorption effects are taken into account (see Section 3.2.3). Under the assumption of impermeable membrane (no gas crossover), there is no need for additional equations for nitrogen or hydrogen molar fractions since they can be obtained as  $x_{N_2} = 1 - x_{O_2} - x_w$  in the cathode side and  $x_{H_2} = 1 - x_w$  in the anode side, respectively. Table 3.1 includes the source terms for hydrogen (if needed), oxygen and water transport equations (3.37) and (3.38), where  $i$  is the volumetric current density and  $F$  is Faraday's constant.

Source terms in Table 3.1 follow directly from the relation between current density and species flux discussed in Section 3.3 and the number of charged species (electrons) per mole of oxygen and water in the electrochemical reaction (3.71).

### 3.2.2 Water transport in the polymer electrolyte

Water transport in the electrolyte is generally considered either in liquid or sorbed form. In the former approach, based on the works by Bernardi and Verbrugge [2, 201], the membrane is assumed to be a polymer matrix with pores filled with liquid water. The velocity of liquid water in the membrane is computed using the Schlögl equation [2, 5, 201, 305–307]

$$\mathbf{v} = \frac{\hat{\mathbf{K}}_\phi}{\mu} z_f c_f F \nabla \phi_m - \frac{\hat{\mathbf{K}}_p}{\mu} \nabla p_l, \quad (3.39)$$

where  $\hat{\mathbf{K}}_\phi$  is the electrokinetic permeability of the membrane,  $\mu$  is the viscosity of the pore fluid,  $z_f$  is the charge number of the sulfonic acid ions attached to the polymer backbone in the membrane,  $c_f$  is their concentration,  $\hat{\mathbf{K}}_p$  is the hydraulic permeability of the membrane, and  $p_l$  is the hydraulic pressure. The driving forces considered in this model are associated with the electroosmosis and hydraulic pressure. Velocity (3.39) is used to describe convective mass transport in the membrane [2,201]. This approach is generally used for fully humidified membranes and diffusive transport of water is neglected [5].

A more common approach was proposed by Springer et al. [1], in which the membrane is assumed to be homogeneous and non-porous. In their model, water is transported in the sorbed form and is driven by electroosmosis and back diffusion. The flux of sorbed water due to electroosmosis is proportional to the proton flux in the membrane [1, 82, 304, 308, 309]:

$$\mathbf{N}_{\lambda, \text{drag}} = -n_d \frac{\sigma_m^{\text{eff}}}{F} \nabla \phi_m, \quad (3.40)$$

where  $\sigma_m^{\text{eff}}$  and  $\phi_m$  are the conductivity of the electrolyte and its potential (see Section 3.3) and  $n_d$  is the electroosmosis coefficient (the ratio of the flux of water molecules to the flux of protons in the absence of concentration gradients). In the PEM, the effective value is the bulk value. In the CL, the effective value is obtained using relations such as (3.32) [43, 170]. The electroosmosis coefficient has been studied by various groups over the past decade, e.g., references [1, 310–312] to name but a few. Kusoglu and Weber [139] reviewed previous work and highlighted that most of them report electroosmosis values of 0.9 to 1.4 in vapor-equilibrated membranes ( $\lambda < 14$ ) and 2.5 to 2.9 in liquid water equilibrated membranes ( $\lambda > 20$ ). Analysis of the results for vapor-equilibrated membranes also shows that, although some authors have reported a constant electroosmosis coefficient of approximately one, e.g., [310, 311], many others have observed a quasi-linear relationship between the number of sorbed water molecules and the electroosmosis coefficient, e.g., [1, 312–314], with a relationship that is similar to that proposed by Springer et al. [1] and given by

$$n_d = \frac{2.5\lambda}{22},$$

where  $\lambda$  is the sorbed water content in the membrane (in moles of sorbed water per number of moles of sulfonate groups  $\text{SO}_3^-$ ). The electroosmosis coefficient also depends on temperature and membrane equivalent weight and type and manufacturing method, e.g., casted or extruded [139].

The sorbed water flux due to back diffusion is defined as [1, 82, 304, 308, 309]

$$\mathbf{N}_{\lambda, \text{diffusion}} = -\frac{\rho_{\text{dry}}}{EW} D_\lambda^{\text{eff}} \nabla \lambda, \quad (3.41)$$

where  $\rho_{\text{dry}}$  is the density of the dry ionomer and  $EW$  is its equivalent weight (in grams of the ionomer per mole of ionic group). The effective diffusion coefficient  $D_\lambda^{\text{eff}}$  again will be bulk in the PEM and an effective value in the CL. The bulk diffusion coefficient depends on  $\lambda$  and temperature. The exact functional form of  $D_\lambda^{\text{eff}}(\lambda, T)$  depends on the type of the ionomer and is obtained through fitting of experimental data. Examples of such relations for bulk sorbed water diffusivity in Nafion<sup>®</sup> can be found in [31, 315, 316] to name but a few. Zhou et al. recently implemented the latter expressions in a full MEA model in order to study their effect on water transport in reference [317]. Kusoglu and Weber [139] provided a detailed review of the water diffusion coefficients reported in the literature.

Under non-isothermal conditions, the sorbed water is also transported due to variations in temperature. This process is called thermo-osmosis [130, 318, 319], and the corresponding flux of the sorbed water is [304, 308, 309]

$$\mathbf{N}_{\lambda, \text{thermo-osmosis}} = -\frac{D_T^{\text{eff}}}{M_{\text{H}_2\text{O}}} \nabla T, \quad (3.42)$$

where  $D_T^{\text{eff}}$  is the effective thermo-osmosis diffusion coefficient, the values of which vary between the materials [130, 318, 319].

The total sorbed water flux in the electrolyte considering all three modes of transport is given by

$$\mathbf{N}_\lambda = \mathbf{N}_{\lambda, \text{drag}} + \mathbf{N}_{\lambda, \text{diffusion}} + \mathbf{N}_{\lambda, \text{thermo-osmosis}} = -n_d \frac{\sigma_m^{\text{eff}}}{F} \nabla \phi_m - \frac{\rho_{\text{dry}}}{EW} D_\lambda^{\text{eff}} \nabla \lambda - \frac{D_T^{\text{eff}}}{M_{\text{H}_2\text{O}}} \nabla T, \quad (3.43)$$

where in the PEM the bulk values should be used. Thus, the mass conservation equation for sorbed water takes the following form:

$$\varepsilon_N \frac{\rho_{\text{dry}}}{EW} \frac{\partial \lambda}{\partial t} - \nabla \cdot \left( n_d \frac{\sigma_m^{\text{eff}}}{F} \nabla \phi_m + \frac{\rho_{\text{dry}}}{EW} D_\lambda^{\text{eff}} \nabla \lambda + \frac{D_T^{\text{eff}}}{M_{H_2O}} \nabla T \right) = S_\lambda, \quad (3.44)$$

where the transient term is present in the form natural for the diffusion-type equation (3.44) and  $\varepsilon_N$  is the volume fraction of the ionomer in the CL and  $\varepsilon_N = 1$  in the PEM. The complexity of the resulting model depends on how many driving forces are considered in equation (3.44). The source term,  $S_\lambda$ , is given by [82]

$$S_\lambda = \begin{cases} k_t \frac{\rho_{\text{dry}}}{EW} (\lambda_{\text{eq}} - \lambda) & \text{in CLs,} \\ 0 & \text{everywhere else,} \end{cases} \quad (3.45)$$

where  $k_t$  is a time constant and  $\lambda_{\text{eq}}$  is the equilibrium value of  $\lambda$  in the electrolyte determined by a sorption isotherm [320]. In general,  $\lambda_{\text{eq}}$  depends on the equivalent weight of the ionomer, water vapor mole fraction, and temperature [139]. Experimentally fitted  $\lambda_{\text{eq}}$  can be obtained in the form  $\lambda_{\text{eq}}(a_w, T)$  [321], where the activity of water is defined as

$$a_w = \frac{p \, x_{H_2O}}{p_{\text{sat}}},$$

Since water sorption/desorption affects water vapor transport,  $S_\lambda$  is also included in equation (3.38) so that it is modified into

$$\varepsilon_v \frac{\partial c_w}{\partial t} - \nabla \cdot (c D_w^{\text{eff}} \nabla x_w) = S_w - S_\lambda.$$

For  $k_t < 10^{-2} \text{ s}^{-1}$ ,  $S_\lambda$  becomes negligible compared to  $S_w$ , and the coupling between water vapor transport and water sorption/desorption is weak [82]. The time required for  $\lambda$  to reach its equilibrium value is normally of order  $100 - 1,000 \text{ s}^{-1}$  [322]. In steady-state simulations, a value 10,000 may be used to ensure strong coupling between the equations [82, 308]. Because of the coupling, water vapor will either be sorbed into the ionomer from the pore space or desorbed from the ionomer depending on the relative humidity and temperature conditions.

The effective electrolyte protonic conductivity  $\sigma_m^{\text{eff}}$  used in the sorbed water transport equation (3.44) and electrolyte potential transport equation (see Section 3.3) is the bulk value, and in the CL is an effective value. In general, the bulk conductivity depends on the water content and temperature, as it was discussed in Sections 2.4. The functional form  $\sigma_m^{\text{eff}}(a_w, T)$  or  $\sigma_m^{\text{eff}}(\lambda, T)$  is obtained experimentally and can be found in [308].

### 3.2.3 Liquid water in MEAs

Water management is critical to achieving higher current density and improving the durability of fuel cells, especially under cold and wet operating conditions. A large number of models have been proposed in the fuel cell literature during the past decades to study water management [323–331]. Based on these studies, it was identified that the key to appropriate fuel cell water management is to strike a balance between membrane dehydration and water accumulation in the electrode, also known as flooding. When the cell is operating with dry gases, keeping the electrolyte in the PEM and CLs sufficiently hydrated is critical to maintaining good ionic conductivity and reducing ohmic losses. During high relative humidity and high current density operation, removing the excess water generated in the electrodes is critical to avoid water accumulation and achieve high performance.

Liquid water is produced at the cathode CL. At low relative humidity, the generated liquid water evaporates and is transported to the channels in vapor phase. If the electrode gas mixture is saturated with water vapor, liquid water accumulates in the electrode. This leads to a sharp drop in performance which limits the fuel cell maximum current and power densities. When a sufficient liquid pressure is available to flow through the CL, MPL, and GDL, liquid water removed from the MEA will reach the gas flow channels and negatively affect also the reactant flow as discussed in previous sections.

Natarajan et al. [332] proposed one of the first two-phase cathode models in the literature. Wang et al. [333] also introduced a two-phase model that included a threshold current density to distinguish the single- and two-phase regimes. Weber and Newman proposed the first structure-based two-phase flow model [330]. It included mass and momentum conservation equations for gas and liquid transport in the MEA and it used a pore size distribution to estimate transport properties. The models above, however, did not account for thermal effects. Thermal effects were accounted for in more recent two-phase models, allowing to study the heat pipe effect as well as phase change induced flow [209, 304, 323].

Two-phase flow transport in the porous media of fuel cells has usually been studied using a volume-averaged approach at the MEA level [209, 304, 323, 330, 333]. This approach is based on the assumption that there exists a

Table 3.2: Estimated dimensionless numbers for an operating PEMFC.

Dimensionless Characteristic length	Physical meaning	GDL 10 $\mu\text{m}$	CL 0.1 $\mu\text{m}$
Bond	Gravitational force to surface tension	$10^{-3}$	$10^{-7}$
Weber	Inertial force to surface tension	$10^{-10}$	$10^{-12}$
Capillary	Viscous force to surface tension	$10^{-7}$	$10^{-7}$

representative elementary volume (REV) in the porous medium where hydrophilic and hydrophobic pore networks are homogeneous. In general, pore-scale models, such as full morphology and pore network models (discussed in the following sections), have been mainly used to study two-phase flow in the GDL while volume-averaged models incorporating information on the pore size distribution have been used in the MPL and CL. Such choice is appropriate given the length scales in each layer. Conventional CLs and MPLs are 5-15  $\mu\text{m}$  and 40-80  $\mu\text{m}$  in thickness, respectively. CLs contain pores that are 5-210 nm, with most pores in the range of 20-80nm [18, 29, 334, 335], and MPLs contain pores that are smaller than 1  $\mu\text{m}$  [336]. Given the pore size and layer thickness, there are hundreds of pores across any CL and MPL and, therefore, an REV is likely to exist. In this case, volume-averaged models are appropriate and effective properties, such as interfacial area, effective diffusivity and relative permeability, are likely well approximated by using statistical theory of heterogeneous media. In the GDL, the layer thickness is 150-400  $\mu\text{m}$  and the pore size is between 5 and 60  $\mu\text{m}$ . Due to the size of the pores, an REV for the GDL might be of the same size or even larger than the GDL thickness; thereby, a volume-average model should not be used [337]. The use of an REV for the GDL can only be justified on the basis of averaging along the channel to create a two-dimensional model. The use of pore-scale models is more appropriate however, and the integration of volume-average MPL and CL models with a pore-scale model has been recently performed by Zenyuk et al. [338].

The effect of liquid water can be studied by reducing the void fraction available for gas transport in porous layers, however a mechanism is required in order to estimate the percentage of pores that will be filled with water. In the crudest approximations, the volume fraction is treated as a fitting parameter. Thus, the only effect of liquid water is to decrease the mobility of reactants to diffuse to the electrochemically active site [339, 340]. Most mathematical models in the literature, however, assume that capillary pressure is the driving force for pore filling in porous media, an assumption that is justified based on non-dimensional analysis that shows that surface tension effects are orders of magnitude larger than gravitational, inertial and viscous effects. To validate this assumption, Bond [341, 342], Bo, Weber [342], We, and Capillary [343], Ca, numbers for GDL and CL are summarized in Table 3.2, see reference [308] for more details. Table 3.2 clearly shows that surface tension effects are at least three orders of magnitude larger than any of the other effects discussed above.

The transport equations described in Section 3.2.1 are solved for each phase in order to estimate capillary pressure [5, 201, 330]. Assuming the Reynolds number in the porous media for gas and liquid phases is small, i.e., less than one, and using further simplifications a mass conservation equation, (3.1), and Darcy's law for momentum transport, (3.26) can be obtained for each phase. Two approaches are proposed in literature as the two-phase transport governing equations in the MEA: a) saturation-based, and b) capillary-based models.

In saturation-based models, gas pressure changes are assumed negligible and capillary pressure and saturation are related by an empirical function known as the Leverett J-function. Using these assumptions, Darcy's law equation for the liquid phase is reformulated as a function of saturation,  $s$ , instead of capillary pressure,  $p_c$ , and the former is used as the solution variable. The governing equation can then be expressed as

$$\frac{\partial(\varepsilon_v s \rho_l)}{\partial t} - \nabla \cdot \left( \frac{\rho_l k_{lr}}{\mu_l} \left( \frac{\partial p_c}{\partial s} \right) \nabla s \right) = S_{\text{liquid}}, \quad (3.46)$$

where  $\varepsilon_v$  is the porosity,  $k_{lr}$  is the effective permeability in liquid phase,  $p_c$  is the capillary pressure, and  $s$  is the saturation variable. Note that in this expression, the interstitial density is used instead of the superficial density in equation (3.1) and the permeability tensor is assumed isotropic. This method is generally used in petroleum engineering applications, particularly for measuring the one-dimensional steady-state transport on packed sand [344]. The saturation approach was first adopted by Natarajan and Nguyen [332] in studying the liquid water transport in the cathode. Since then, a great number of saturation-based models have been proposed in literature to study liquid water transport in the MEA [327, 345–350].

One of the primary concerns of using saturation-based models is that, in most cases, a continuous function is used to approximate the saturation variable even though, saturation is likely to be discontinuous at the interface between porous layers, e.g., at MPL-GDL interface, due to the different wettabilities and pore sizes. Also, the approach is usually limited to fully humidified conditions as the specification of a finite saturation at the GDL/channel boundary

Table 3.3: Source terms for two-phase transport.

Parameters	GDL,MPL	CCL	ACL	PEM
$S_{\text{gas}}$	$-M_{H_2O}S_{H_2O(\text{evap}/\text{cond})}$	$-M_{H_2O}S_{H_2O(\text{evap}/\text{cond})} + \frac{i}{4F}M_{O_2} + S_{\lambda}M_{H_2O}$	$-M_{H_2O}S_{H_2O(\text{evap}/\text{cond})} + \frac{i}{2F}M_{H_2} + S_{\lambda}M_{H_2O}$	0
$S_{\text{liquid}}$	$M_{H_2O}S_{H_2O(\text{evap}/\text{cond})}$	$M_{H_2O}S_{H_2O(\text{evap}/\text{cond})} - \frac{i}{2F}M_{H_2O}$	$M_{H_2O}S_{H_2O(\text{evap}/\text{cond})}$	0

implies that some liquid water should already be present in the channel. Even if a value of zero saturation is used, liquid water can flow from the channel to the MEA.

Capillary-based models solve mass and momentum conservation equations for liquid water and gas mixture pressure separately and relate them to saturation by means of the capillary pressure and a set of closure equations using micro-structural information [327–331, 351]. The input parameters for the micro-structural model are the pore size distribution (PSD) and the wettability of the porous material. Based on this information, a bundle of rejoined capillaries model is used to estimate dry and wet transport properties, e.g., liquid and gas permeability and relative permeability. The advantage of this method is that it provides an idealized micro-scale model that can be used to perform parametric studies in order to find the optimized porous layer design. The use of gas and liquid pressure enforces continuity in the pressure fields while saturation is allowed to vary at the interface between materials.

The first capillary-based models that proposed the use of a PSD assumed either a hydrophilic or hydrophobic pore network for the whole material [329, 330]. More recently, researchers have introduced a variety of mixed wettability models based on experimental observations proposing that a network of hydrophilic and hydrophobic pores might co-exist in fuel cell materials such as GDLs and CLs [352, 353]. Weber et al. [323, 330], Mateo [351] and Mulone et al. [331] have treated hydrophilic (HI) and hydrophobic (HO) pore-networks separately either by introducing a continuous wettability distribution [323] or by studying two independent networks [330, 331, 351]. In all previous work, however, due to the difficulty of implementation of a PSD model in multi-dimensional computational fluid dynamics solvers, the PSD model was either not integrated in a complete MEA model [329, 331, 351] or was integrated only in a one-dimensional model [323, 330]. Recently, Zhou et al. [304] introduced a multi-dimensional, two-phase, capillary-based model. The model was shown to be suitable to study fuel cell operation under both dry and wet conditions as well as to predict water distribution in the MEA and water fluxes at the GDL/channel boundaries.

The governing equations for the capillary-based model, which solve for liquid and total gas pressure, respectively, are as follows:

$$\frac{\partial(\rho_g \varepsilon_g)}{\partial t} - \nabla \cdot \left( \frac{\rho_g k_{gr}(p_c)}{\mu_g} \nabla p_g \right) = S_{\text{gas}}, \quad (3.47)$$

$$\frac{\partial(\rho_l \varepsilon_l)}{\partial t} - \nabla \cdot \left( \frac{\rho_l k_{lr}(p_c)}{\mu_l} \nabla p_l \right) = S_{\text{liquid}}, \quad (3.48)$$

where  $\rho$  is the interstitial (phase) density,  $\varepsilon_k$  is the volume fraction of phase  $k$ , and subscripts  $g$  and  $l$  refer to gas and liquid phases, respectively. In this entry, the capillary pressure is defined as

$$p_c = p_l - p_g. \quad (3.49)$$

The corresponding source terms are listed in Table 3.3. The source term for condensation and evaporation is described by

$$S_{H_2O(\text{evap}/\text{cond})} = k_{e/c} a_{lv} \left( \frac{p_v - p_{\text{sat}}(p_c, T)}{p_{\text{sat}}(p_c, T)} \right), \quad (3.50)$$

where  $k_{e/c}$  is the aerial evaporation or condensation rate constant,  $a_{lv}$  is the liquid-gas interfacial surface area per unit volume, and  $p_v$  is the vapor pressure. The effective saturation vapor pressure in a capillary,  $p_{\text{sat}}(p_c, T)$ , is determined by considering the Kelvin effect and the Young-Laplace equation as follows:

$$p_{\text{sat}}(p_c, T) = p_{\text{sat}}(T) \exp\left(\frac{p_c M_G}{RT \rho_g}\right), \quad (3.51)$$

where  $p_{\text{sat}}$  is the uncorrected saturated vapor pressure of water, and  $M_G$  is the molar mass of water.

The GDL and MPL absolute permeabilities have been reported by various studies [45, 285, 286, 288, 291, 294, 354–356]. It has been shown that the absolute permeability depends on many factors such as level of compression, type of carbon black, percentage of PTFE content and pore size distribution. The typical GDL permeability falls

mostly within the range of  $10^{-12}$  to  $10^{-10}$  m<sup>2</sup>. The MPL permeability is usually extrapolated from the measured permeabilities of the GDL and the GDL-MPL assembly and the estimated value is around  $10^{-13}$  m<sup>2</sup>. The measurement of CL absolute permeability is not yet feasible as the layer is too thin to conduct the experiment.

Measurements of GDL relative permeability have not received much attention during the past decades. Air relative permeabilities were reported by Nguyen et al. [357] and Koido et al. [358]. Relative liquid water permeability was measured by Hussaini et al. [359] and Sole [360]. Alternatively, numerical models, such as pore size distribution [304] and pore network models [361], can be used to estimate the relative permeability with a reasonable agreement with the experimental data.

Determining an appropriate liquid water boundary condition at the GDL/channel interface is important to any two-phase flow model. Zero flux [326, 328, 362] and fixed saturation values are the most commonly used boundary conditions [363]. These boundary conditions either force all water to be vaporized in the MEA or impose the existence of liquid water at the GDL/channel boundary. Their applicability is therefore limited and a more general boundary condition is needed. Zenyuk et al. [209] recently introduced a step function to switch from a no flux boundary condition to a Dirichlet condition for liquid pressure. After reaching a breakthrough pressure, the liquid pressure is considered to be constant. Alternatively, a dynamic boundary condition could be used where once the capillary pressure reaches the given breakthrough pressure, a flux proportional to the liquid pressure is applied [304], i.e.,

$$\rho_l \mathbf{v}_l \cdot \mathbf{n} = - \left( \frac{\rho_l k_{rl}}{\mu_l} \nabla p_l \right) \cdot \mathbf{n} = k \left( \frac{p_l - p_{l,\text{channel}}}{p_0} \right) g(p_l), \quad (3.52)$$

where  $k$  is an unknown proportionality constant that controls the flux of water as a function of the liquid pressure,  $p_{l,\text{channel}}$  is the liquid pressure at the channel-GDL interface, and  $p_0$  is a dimensionless factor. Function  $g(p_l)$  in equation (3.52) is given by

$$g(p_l) = \left[ \frac{\tanh((p_l - p_{l,\text{channel}})/p_0) + 1}{2} \right] \theta(p_l - p_{\text{BT}}), \quad (3.53)$$

where  $p_{\text{BT}}$  is the liquid breakthrough pressure and  $\theta(p_l - p_{\text{BT}})$  is a step function, i.e., it is set to be zero until  $p_l > p_{\text{BT}}$  is satisfied in the Newton solver loop and not modified further in order to maintain numerical stability. Its validity should be confirmed during post-processing by making sure that the liquid water flux remains positive. In order to prevent liquid water from entering the MEA from the channel, once the step function is set to be one, a tangent function  $\tanh((p_l - p_{l,\text{channel}})/p_0)$  is used, where  $p_{l,\text{channel}}$  is set to be atmospheric pressure considering the droplet volume is large enough so that Laplace pressure is negligible, and  $p_0$  should reflect the channel conditions.

### 3.3 Charge transport

In general, transport of charged species in an electrolyte is described by either concentrated-solution or dilute-solution models. The former are more general, but require more information on the interactions between the different species in the solution [33, 198]. Multi-component diffusion of charged species is generally described by [198]

$$c_i \nabla \hat{\mu}_i = \sum_{j \neq i} K_{ij} (\mathbf{v}_j - \mathbf{v}_i), \quad (3.54)$$

which is similar to the Maxwell-Stefan equation (3.8). Here,  $\hat{\mu}_i$  is the electrochemical potential of species  $i$ ,  $K_{ij}$  are friction coefficients, and  $\mathbf{v}_i$  is the superficial velocity of species  $i$ . The term  $-c_i \nabla \hat{\mu}_i$  in equation (3.54) is a volumetric driving force causing the motion of species  $i$ ; the term  $K_{ij} (\mathbf{v}_j - \mathbf{v}_i)$  is the balancing volumetric force of species  $j$  acting on species  $i$  in their relative motion. Coefficients  $K_{ij}$  can be related to the binary interaction coefficients  $D_{ij}$  with [198, 364]

$$K_{ij} = \frac{RT c_i c_j}{c D_{ij}}. \quad (3.55)$$

Assuming that species  $i$  is minor and the total concentration  $c_{\text{tot}}$  is approximately equal to the solvent concentration  $c_0$ , one can use equation (3.55) and rewrite equation (3.54) as

$$c_i \nabla \hat{\mu}_i = \frac{RT}{D_{i0}} (c_i \mathbf{v}_0 - c_i \mathbf{v}_i). \quad (3.56)$$

Then, the molar flux of species  $i$  is given by

$$\mathbf{N}_i = c_i \mathbf{v}_i = - \frac{D_{i0}}{RT} c_i \nabla \hat{\mu}_i + c_i \mathbf{v}_0. \quad (3.57)$$

Further, if the solution is dilute, the species-solvent interaction coefficients  $D_{i0}$  can be replaced with the diffusion coefficients  $D_i$  and the solvent velocity  $\mathbf{v}_0$  can be approximated by the bulk velocity  $\mathbf{v}$ :

$$\mathbf{N}_i = -\frac{D_i}{RT} c_i \nabla \hat{\mu}_i + c_i \mathbf{v}. \quad (3.58)$$

Equation (3.57) can be written in the form of the Nernst-Planck equation with a convective term [198–202]:

$$\mathbf{N}_i = -z_i \frac{F}{RT} c_i D_i \nabla \phi - D_i \nabla c_i + c_i \mathbf{v}. \quad (3.59)$$

Note that, in the case of infinitely dilute solutions, the first term in the right hand side of equation (3.59) is sometimes written in terms of the mobility  $u_i$  of species  $i$  instead of its diffusivity using the Nernst-Einstein equation [33, 198, 200]

$$D_i = RT u_i;$$

Multiplying equation (3.59) by  $z_i F$ , summing over species  $i$ , and using the definition of current density, i.e.,

$$\mathbf{j} = F \sum_i z_i \mathbf{N}_i,$$

and conductivity,  $\sigma$ ,

$$\sigma = F^2 \sum_i z_i^2 c_i u_i = F^2 \sum_i z_i^2 c_i \frac{D_i}{RT},$$

the following expression for the current density is obtained:

$$\mathbf{j} = -\sigma \nabla \phi - F \sum_i z_i D_i \nabla c_i. \quad (3.60)$$

The first term in equation (3.60) is the Ohmic current component of  $\mathbf{j}$  and the second term is the diffusion current. Since sulfonic acid groups are immovable in the solid electrolytes used in PEMFCs, e.g., Nafion, and assuming the only charged species being transported in the membrane is protons, equation (3.60) simplifies to Ohm's law

$$\mathbf{j} = -\sigma \nabla \phi. \quad (3.61)$$

once electroneutrality is assumed, i.e.,

$$\sum_i z_i c_i = 0,$$

Equation (3.61) is commonly used in the area of fuel cell modeling to relate current density and variation in the potential, although its applicability is limited by the assumptions listed above. In cases where ion transport across the membrane is of interest, i.e., in cases when Pt redeposition is to be studied, equation (3.60) should be used. Finally, if the species of interest is not minor in the solution, then the general model (3.54), (3.55) should be used.

In hydrogen PEM fuel cells, there are mainly two types of charged species that are transported, electrons in the solid phase of GDLs and CLs (and in BPPs) and protons in the PEM and in the ionomer in CLs, and therefore two current densities,  $\mathbf{j}_p$  and  $\mathbf{j}_e$ . They are equal to each other in absolute value and have opposite signs:  $\mathbf{j}_p = -\mathbf{j}_e$ . Each of them is normally assumed to obey Ohm's law (3.61),

$$\begin{aligned} \mathbf{j}_p &= -\sigma_m^{\text{eff}} \nabla \phi_m, \\ \mathbf{j}_e &= -\sigma_s^{\text{eff}} \nabla \phi_s, \end{aligned}$$

where effective conductivity depends on the structure and composition of the medium and is approximated using the percolation or the random walk method (see Section 3.2 for details).

The typical effective electrical conductivity values for PEMFC GDLs are in the range of 80 - 200 S/cm in the in-plane direction [285, 365, 366], reaching the higher of the reported values when MPL is dispersed on the side of the diffusion layer [285], and in the range 3 - 70 S/cm in the through-plane direction [285, 365, 366]. In the catalyst layers, effective electrical conductivities are reported to be between 0.1 and 3.0 S/cm for a wide range of solid phase volume fractions from 0.1 to 0.8 [367, 368].

The bulk proton conductivity in the ionomer phase is a function of temperature and water content [1, 34, 139, 304, 369–371]. The water content, which depends on relative humidity and temperature, can be determined using

equation (3.44). Numerical models used to estimate bulk proton conductivity have been proposed by several researchers [1, 210, 372]. One example of the most commonly used model for estimating the bulk proton conductivity is Springer's model [1]:

$$\sigma_m = 0.005139\lambda - 0.00326 \exp(1268.0(1.0/303.0 - 1.0/T)), \quad (3.62)$$

Kusoglu and Weber [139] recently compiled a comprehensive list of the proton conductivity measurements for various PEM types at varying relative humidity and temperature.

The effective proton conductivity in the catalyst layer is of the order  $10^{-4}$  to  $10^{-1}$  S/cm [58, 373]. There are a few models proposed in the literature to compute the effective proton conductivity in the catalyst layer such as Bruggeman method, percolation theory and the correlation proposed by Iden et al. using experiments with a pseudo-catalyst layer on a hydrogen pump [371].

In order to estimate the phase potential, a charge conservation equation is used,

$$\frac{\partial \hat{\rho}}{\partial t} + \nabla \cdot \mathbf{j} = R,$$

where  $\hat{\rho}$  is the free charge density and  $R$  is a source/sink term due to electrochemical reactions and charge redistribution as discussed later in this section. For convenience, models are usually constructed considering the volumetric electronic current density  $i = \nabla \cdot \mathbf{j}_e$ , A/cm<sup>3</sup>. Equations modeling charge transport in PEMFCs are predominantly used in their steady-state form even though other effects may be considered in transient [40, 61, 63–71, 73, 76, 78, 203–209]. This leads to the two equations describing the steady-state transport of charge,

$$-\nabla \cdot (\sigma_m^{\text{eff}} \nabla \phi_m) = R_{\text{H}^+}, \quad (3.63)$$

$$-\nabla \cdot (\sigma_s^{\text{eff}} \nabla \phi_s) = R_{\text{e}^-}, \quad (3.64)$$

where  $R_{\text{H}^+}$  and  $R_{\text{e}^-}$  are reaction source terms and are defined as

$$R_{\text{H}^+} = \begin{cases} -i & \text{in cathode CL,} \\ i & \text{in anode CL,} \\ 0 & \text{everywhere else;} \end{cases} \quad (3.65)$$

and

$$R_{\text{e}^-} = \begin{cases} i & \text{in cathode CL,} \\ -i & \text{in anode CL,} \\ 0 & \text{everywhere else.} \end{cases} \quad (3.66)$$

The interface between the solid phase and the surrounding electrolyte act as a capacitor. At a given potential, there exists charge  $q_1$  at the electrode surface and charge  $q_2 = -q_1$  accumulated as a thin layer in the electrolyte at the interface with the electrode (Figure 3.4). Such interfacial distribution of charged species and oriented dipoles is called the electrical double layer. A change in the potential causes redistribution of charge at the interface, which gives rise to the transient charging (or capacitive) current.

When no capacitive effects are taken into account, the total volumetric current density,  $i$ , is equal to  $i_f$ , the faradaic current resulting from electrochemical reactions, which can be computed using equation (3.81) or (3.94) using the kinetic models (described in Section 3.4). In the presence of a double layer with volumetric capacitance  $C_{\text{dl}}$ , F/cm<sup>3</sup>, total current density consists of faradaic and charging current densities [199],

$$i = i_f + i_c,$$

where

$$i_c = -C_{\text{dl}} \frac{\partial \eta}{\partial t}.$$

In this case, the total current is no longer purely faradaic and the charge conservation equations (3.63) and (3.64) include transient terms describing capacitive current due to the rearrangement of charge in the double layers inside CLs in addition to the faradaic current accounted for in the reaction source terms:

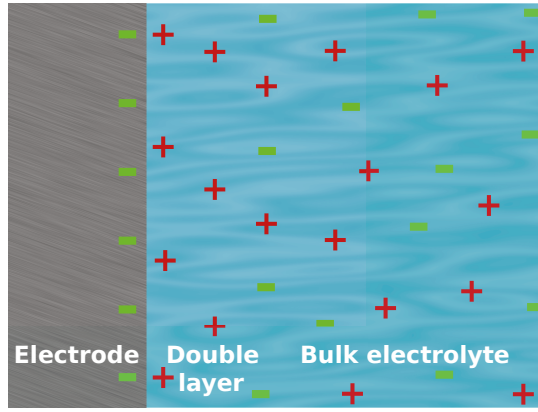


Figure 3.4: Illustration of the electrical double layer at the electrode-electrolyte interface.

$$-C_{\text{dl}} \frac{\partial \eta}{\partial t} - \nabla \cdot (\sigma_m^{\text{eff}} \nabla \phi_m) = R_{\text{H}^+}, \quad (3.67)$$

$$C_{\text{dl}} \frac{\partial \eta}{\partial t} - \nabla \cdot (\sigma_s^{\text{eff}} \nabla \phi_s) = R_{\text{e}^-}, \quad (3.68)$$

where  $\eta$  is the local overpotential defined as

$$\eta = \phi_s - \phi_m - E_{\text{th}}. \quad (3.69)$$

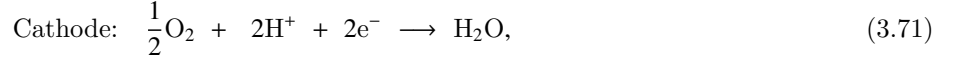
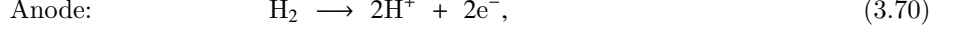
and  $E_{\text{th}}$  is the theoretical half-cell potential.

In fuel cells, charge transport is always coupled with mass and thermal transport through reaction source terms, and therefore equations (3.63) and (3.64) are never purely steady-state when any of the latter two processes are transient. Choice of those equations over their fully transient form (3.67), (3.68) is often made with assumption of negligible double layer effect. Double layer charging and discharging is normally observed at relatively small time scales that depend on the double layer capacitance, which is estimated to be between  $8 \cdot 10^{-3}$  and  $10^{-1}$  F/cm<sup>2</sup> [374–380] or between 3 and 9 F/cm<sup>3</sup> [367,378] (or between 3 and 34 F/cm<sup>3</sup> if recomputed from F/cm<sup>2</sup> using the reported catalyst layer thickness in [374,376,377,379]).

Most of literature disregards double layer effects, often referring to the work of Wang and Wang [79], who claimed that the time constant of double layer discharging is of order  $10^{-7}$  s while the time constant for gas diffusion through GDLs is of order  $10^{-2}$  s and for membrane hydration is of order 10 s. When estimating the charging/discharging time for the double layer, Wang and Wang considered the double layer capacitance per unit area,  $C_{\text{dl}}^{\text{a}}$ , of  $2 \cdot 10^{-5}$  F/cm<sup>2</sup>. Peng et al. [62] have simulated a cell with two orders of magnitude larger capacitance (which corresponds to the experimental values listed above) and have shown that such values affect approximately the first 0.15 s of the current density response to a step change in cell voltage, a significantly longer time period than estimated by Wang and Wang. Moreover, since the time constant for the double layer charging is directly proportional to its capacitance [79], an increase of the double layer capacitance by just one order of magnitude to order 10 F/cm<sup>3</sup> leads to charging effects lasting for more than a second [62], “smoothing” the response even further. In contrast, absence of the double layer in the model ( $C_{\text{dl}} = 0$ ) may lead to over- and undershoots in the power output of the cell when a change in current or voltage is applied [62,375]. Peaks in the transient response of the cell are observed experimentally [76,379]; their size and stabilization time depend not only on the double layer capacitance, but also on the operating conditions [61,65,67–69,73,76,79]. Such peaks are commonly attributed to reactant availability after the step change in operating conditions [61,65,68,69,381] and membrane water content [69]. Further modeling and experimental studies are required to estimate the time scale of the double layer charging effects at various operating conditions and for various catalyst layer compositions.

### 3.4 Electrochemical reactions

Electrochemical reactions taking place in the fuel cell are responsible for generation of electric current by converting the chemical energy of the reactants, i.e., hydrogen and oxygen, to electrical energy. For a hydrogen PEM fuel cell, the half-cell reactions at the anode and cathode are



where the anodic reaction is the hydrogen oxidation reaction (HOR) and the cathodic reaction is the oxygen reduction reaction (ORR). The source terms in mass and charge transport equations in the CL are computed from the HOR and ORR kinetic models. The reaction kinetic models compute the current density (or volumetric current density) as a function of the reactant concentration (partial pressure of gases) and overpotential  $\eta$ .

Butler-Volmer and Tafel kinetics are most commonly used to describe the reaction kinetics for both the HOR [1, 5, 34, 220, 338, 345] and ORR [1, 5, 34, 44, 329, 333, 382]. Using the Butler-Volmer equation, the volumetric current density  $i$  can be written as [184, 345]

$$i = A_v j_0^{ref} \left\{ \left[ \prod_{i=\text{reactants}} \left( \frac{c_i}{c_i^*} \right)^{\gamma_i} \right] \exp\left(\frac{-\alpha_R F \eta}{RT}\right) - \left[ \prod_{i=\text{products}} \left( \frac{c_i}{c_i^*} \right)^{\gamma_i} \right] \exp\left(\frac{\alpha_P F \eta}{RT}\right) \right\}, \quad (3.72)$$

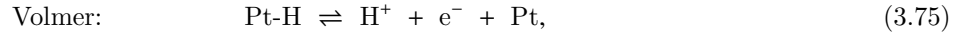
where  $A_v$  is the active area of platinum per unit volume of catalyst layer,  $c_i$  is the concentration of species  $i$  at the electrode surface,  $c_i^*$  is the concentration of species  $i$  at which the exchange current density,  $j_0^{ref}$ , was measured,  $\alpha_R$  and  $\alpha_P$  are the reaction transfer coefficients, and  $\gamma_i$  is the reaction order with respect to species  $i$ .

For sluggish reactions requiring high negative overpotentials to proceed such as the ORR, the Butler-Volmer equation (3.72), can be simplified to the Tafel expression:

$$i = A_v j_0^{ref} \left\{ \left[ \prod_{i=\text{reactants}} \left( \frac{c_i}{c_i^*} \right)^{\gamma_i} \right] \exp\left(\frac{-\alpha_R F \eta}{RT}\right) \right\}.$$

Butler-Volmer and Tafel kinetics are only valid for single electron transfer and multi-step reactions with a unique rate determining step. Experimental evidence however suggests that HOR [8, 383, 384] and ORR [385–388] have rate determining step that change with overpotential. Thus, kinetic models which can take into account the multi-step reaction mechanisms are required to accurately predict the reaction rates for the HOR and ORR. Complex kinetic models are also required to study Pt dissolution and carbon corrosion.

HOR on Pt catalyst is generally described by the Tafel-Heyrovsky-Volmer mechanism [389–391],



with two possible pathways, i.e., Tafel-Volmer and Heyrovsky-Volmer, for the oxidation of hydrogen to protons. The Tafel-Volmer pathway involves a dissociative chemisorption of hydrogen on the Pt surface (Tafel step) followed by the one-electron oxidation reaction of the adsorbed hydrogen atom (Volmer step) which occurs twice. In the Heyrovsky-Volmer mechanism, the first step involves dissociative adsorption of hydrogen along with one-electron oxidation of one of the hydrogen atoms (Heyrovsky step) followed by the one-electron oxidation of the adsorbed hydrogen atom (Volmer step). Studies have shown the relative contributions of the Tafel-Volmer and Heyrovsky-Volmer mechanisms at different overpotentials and limiting mass transport currents [383, 392, 392, 393]. Wang et al. [8] proposed a dual path kinetic model for the HOR that considered both reaction pathways and was able to accurately model experimental polarization curves for a range of limiting mass transport currents.

For the dual path model, the reaction rates for each of the elementary steps in equations (3.73)-(3.75) are [8]

$$\nu_T = k_T(1 - \theta_{\text{Pt-H}})^2 c_{\text{H}_2} - k_{-T} \theta_{\text{Pt-H}}^2, \quad (3.76)$$

$$\nu_H = k_H(1 - \theta_{\text{Pt-H}}) c_{\text{H}_2} \exp\left(\frac{(1 - \beta_H) F E}{RT}\right) - k_{-H} \theta_{\text{Pt-H}} c_{\text{H}^+} \exp\left(\frac{-\beta_H F E}{RT}\right), \quad (3.77)$$

$$\nu_V = k_V \theta_{\text{Pt-H}} \exp\left(\frac{(1 - \beta_V) F E}{RT}\right) - k_{-V} c_{\text{H}^+} (1 - \theta_{\text{Pt-H}}) \exp\left(\frac{-\beta_V F E}{RT}\right), \quad (3.78)$$

where  $\nu$  is the rate of the reaction,  $E$  is the half-cell voltage,  $k$  is the equilibrium rate constant (usually computed from experimental data), subscripts T, H, and V denote the Tafel, Heyrovsky, and Volmer reactions, and negative subscripts denote the backward reactions. Wang et al. [8] suggest a value of 0.5 for both  $\beta_H$  and  $\beta_V$ . The coverage

$\theta_{\text{Pt-H}}$  is defined as the fraction of active Pt sites occupied by the intermediate adsorbed species Pt-H. Therefore,  $(1 - \theta_{\text{Pt-H}})$  gives the fraction of active Pt sites available for reaction, as seen in equations (3.76) and (3.77). Using equations (3.76)-(3.78), the change in coverage of the intermediate species can be written as

$$\frac{d\theta_{\text{Pt-H}}}{dt} = 2\nu_T + \nu_H - \nu_V. \quad (3.79)$$

The HOR current density,  $j_{\text{HOR}}$ , can be computed as

$$j_{\text{HOR}} = F(\nu_H + \nu_V), \quad (3.80)$$

which gives the current per unit area of Pt. The volumetric current density,  $i_{\text{HOR}}$ , i.e., current per unit volume of electrode, can be obtained using

$$i_{\text{HOR}} = j_{\text{HOR}}A_v, \quad (3.81)$$

which is used in the source term in equations (3.67) and (3.68) and in Table 3.3 for the anode.

Equations (3.76)-(3.80) summarize the general set of nonlinear system of equations for the dual-path HOR kinetics with six rate constants and two cathodic transfer coefficients. However, for practical implementation into MEA or full-cell models, the kinetic model needs to be simplified so that the overall simulation is feasible and computationally efficient. Further, the rate constants cannot be measured directly from experiments, therefore, they must be fitted to the experimental data by correlating them to the exchange current density, i.e, the current density produced when the reaction is at equilibrium (forward reaction rate is equal to the backward reaction rate). The following assumptions are made to simplify the dual-path kinetic model:

1. steady state conditions are assumed for the coverages so that  $\frac{d\theta_{\text{Pt-H}}}{dt} = 0$ ;
2. the rate of the Volmer reaction is much higher than the Tafel or Heyrovsky reactions;
3. the coverage of the intermediate species is small so that  $(1 - \theta_{\text{Pt-H}}) \sim 1$  and  $(1 - \theta_{\text{Pt-H}}^0) \sim 1$ ;
4. the concentration of protons ( $c_{\text{H}^+}$ ) is equal to the reference equilibrium proton concentration ( $c_{\text{H}^+}^{\text{eq}}$ ); and
5. the cathodic transfer coefficients for Heyrovsky and Volmer reactions are 0.5 ( $\beta_H = \beta_V = 0.5$ ) [8].

Applying these assumptions to equations (3.76)-(3.80) and correlating the rate constants to the exchange current density, the coverage of the intermediate species can be written as

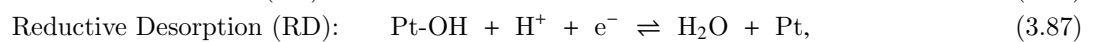
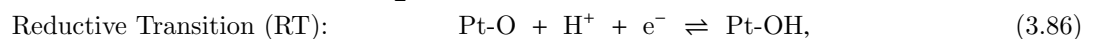
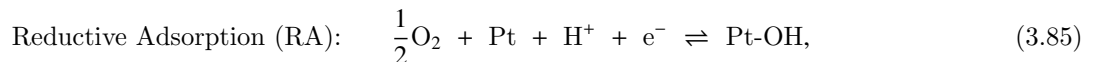
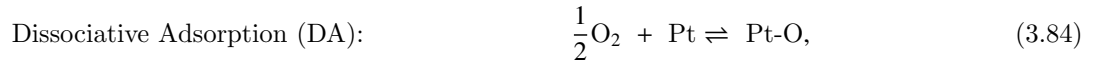
$$\frac{\theta_{\text{Pt-H}}}{\theta_{\text{Pt-H}}^0} = e^{\frac{-F\eta}{\gamma_{\text{ads}}RT}} \quad (3.82)$$

where  $\theta_{\text{Pt-H}}^0$  is the equilibrium coverage of the intermediate species and  $\gamma_{\text{ads}}$  is the potential range constant for adsorption isotherm [8]. The HOR current density can then be computed as [8]

$$j_{\text{HOR}} = j_{0T} \left[ \frac{c_{\text{H}_2}}{c_{\text{H}_2}^{\text{ref}}} - \frac{c_{\text{H}_2}^0}{c_{\text{H}_2}^{\text{ref}}} e^{\frac{-2F\eta}{\gamma_{\text{ads}}RT}} \right] + j_{0H} \left[ \frac{c_{\text{H}_2}}{c_{\text{H}_2}^{\text{ref}}} e^{\frac{F\eta}{2RT}} - \frac{c_{\text{H}_2}^0}{c_{\text{H}_2}^{\text{ref}}} e^{\frac{-F\eta}{\gamma_{\text{ads}}RT}} e^{\frac{-F\eta}{2RT}} \right], \quad (3.83)$$

where  $c_{\text{H}_2}^0$  is the equilibrium concentration of hydrogen at the Pt surface,  $c_{\text{H}_2}^{\text{ref}}$  is the saturation concentration of  $\text{H}_2$  under 1 atm pressure, and  $j_{0T}$  and  $j_{0H}$  are the exchange current densities for the Tafel and Heyrovsky reactions, respectively. A detailed derivation of equations (3.82) and (3.83) can be found in reference [8]. Equation (3.83) can be implemented in any numerical model and a similar expression is implemented, for example in OpenFCST [6, 83].

Several studies have been performed to investigate the ORR mechanism on Pt catalyst [385, 388, 394–397]. Walch et al. [398] summarize the different ORR mechanisms where up to six intermediate adsorbed species, namely  $\text{O}_{2(\text{ads})}$ ,  $\text{O}_{(\text{ads})}$ ,  $\text{HO}_{2(\text{ads})}$ ,  $\text{H}_2\text{O}_{2(\text{ads})}$ ,  $\text{H}_2\text{O}_{(\text{ads})}$ , and  $\text{OH}_{(\text{ads})}$ , can be present. However, detailed reaction pathways such as those in [398] are generally not used for fuel cell modeling. Only recently, the double trap mechanism proposed by Wang et al. [397], which assumes two intermediate species,  $\text{OH}_{(\text{ads})}$  and  $\text{O}_{(\text{ads})}$ , was used for fuel cell MEA models [51, 304, 317, 338, 399, 400]. The elementary reactions for the double trap mechanism for the ORR on Pt proposed by Wang et al. [397] and later fitted to experimental data by Moore et al. [27] are



where Pt-O and Pt-OH are adsorbed species on the Pt active sites. The double trap mechanism proposes that ORR can take place via two routes, namely DA-RT-RD and RA-RD. Markiewicz et al. [388] found that the double trap model was unable to predict their experimental ORR polarization curves for potentials in the range of 0.3-0.7 V. They proposed a modified double trap model with three intermediate species, however an analytical expression for the current density was not provided and therefore the model is not discussed further.

In the double trap model, the reaction rates for the reactions in equations (3.84)-(3.87) are,

$$v_{DA} = k_{DA}\psi c_{O_2}^{\frac{1}{2}} - k_{-DA}\theta_{Pt-O}, \quad (3.88)$$

$$v_{RA} = k_{RA}\psi c_{O_2}^{\frac{1}{2}} c_{H^+} \exp\left(\frac{-\beta_{RA}FE}{RT}\right) - k_{-RA}\theta_{Pt-OH} \exp\left(\frac{(1-\beta_{RA})FE}{RT}\right), \quad (3.89)$$

$$v_{RT} = k_{RT}\theta_{Pt-O} c_{H^+} \exp\left(\frac{-\beta_{RT}FE}{RT}\right) - k_{-RT}\theta_{Pt-OH} \exp\left(\frac{(1-\beta_{RT})FE}{RT}\right), \quad (3.90)$$

$$v_{RD} = k_{RD}\theta_{Pt-OH} c_{H^+} \exp\left(\frac{-\beta_{RD}FE}{RT}\right) - k_{-RD}\psi \exp\left(\frac{(1-\beta_{RD})FE}{RT}\right), \quad (3.91)$$

where  $\psi$  is the fraction of active platinum sites available, which is related to the coverage of intermediate species through the following equation:

$$\psi = 1 - \theta_{Pt-O} - \theta_{Pt-OH}. \quad (3.92)$$

Using the reaction rates from equations (3.88)-(3.91), the ORR current density,  $j_{ORR}$ , can be computed using

$$j_{ORR} = -F(v_{RA} + v_{RT} + v_{RD}), \quad (3.93)$$

where the negative sign is added to follow the convention that reduction current is negative and  $j_{ORR}$  is the ORR current per unit area of platinum. Similar to the HOR, the volumetric current density  $i_{ORR}$  can be obtained as

$$i_{ORR} = j_{ORR}A_v, \quad (3.94)$$

which is used in the source terms in equations (3.67) and (3.68) and in Tables 3.1, and 3.3 for the cathode. The following assumptions are made to simplify the expression for  $j_{ORR}$ :

1. steady state conditions are assumed for the coverages so that  $\frac{d\theta_{Pt-O}}{dt} = 0$  and  $\frac{d\theta_{Pt-OH}}{dt} = 0$ ;
2. the concentration of protons is constant and equal to the reference equilibrium proton concentration; and
3. the equilibrium free energies of the intermediates ( $\theta_{Pt-O}^{eq}$  and  $\theta_{Pt-OH}^{eq}$ ) can be represented using Langmuir isotherms so that

$$\frac{\theta_{Pt-O}^0}{\psi^0} = e^{-\Delta G_{Pt-O}^0}, \quad (3.95)$$

$$\frac{\theta_{Pt-OH}^0}{\psi^0} = e^{-\Delta G_{Pt-OH}^0}, \quad (3.96)$$

where  $\Delta G_i^0$  denotes the equilibrium Gibbs free energy for intermediate species  $i$ ,  $\theta_{Pt-O}^0$  is the equilibrium coverage of the intermediate species  $O_{ads}$ ,  $\theta_{Pt-OH}^0$  is the equilibrium coverage of the intermediate species  $OH_{ads}$ , and  $\psi^0$  is the equilibrium fraction of free Pt sites.

Applying the assumptions above and relating the rate constants to the free energy of the reactions, the expression for the current density for the ORR is [401]

$$j_{ORR} = j^* \left[ e^{-\frac{\Delta G_{RD}^*}{kT}} \theta_{Pt-OH} - e^{-\frac{\Delta G_{RT}^*}{kT}} \psi \right], \quad (3.97)$$

where  $j^*$  is a reference prefactor for the ORR reaction which is set to  $1,000 \text{ Acm}^{-2}$  in [27, 397] and the coverage of the intermediate steps are given as [27, 401]

$$\theta_{Pt-OH} = \frac{C_{gDA}(C_{gRA}+g_{RD}-g_{RT})-(C_{gRA}+g_{RD})(C_{gDA}+g_{DA}+g_{RT})}{(C_{gDA}-g_{RT})(C_{gRA}+g_{RD}-g_{RT})-(C_{gRA}+g_{RA}+g_{RT}+g_{RD}+g_{RD})(C_{gDA}+g_{DA}+g_{RT})} \quad (3.98)$$

$$\theta_{Pt-O} = \frac{C_{gDA}(C_{gRA}+g_{RA}+g_{RT}+g_{RD}+g_{RD})-(C_{gRA}+g_{RD})(C_{gDA}-g_{RT})}{(C_{gDA}+g_{DA}+g_{RT})(C_{gRA}+g_{RA}+g_{RT}+g_{RD}+g_{RD})-(C_{gRA}+g_{RD}-g_{RT})(C_{gDA}-g_{RT})} \quad (3.99)$$

where  $C$  is the oxygen concentration ratio and is given by

$$C = \left( \frac{c_{O_2}}{c_{O_2}^{ref}} \right)^{1/2} \quad (3.100)$$

The  $g_i$  terms in equations (3.98) and (3.99) are given by:

$$g_i = e^{-\Delta G_i^*/kT} \quad (3.101)$$

where  $\Delta G_i^*$  are the potential dependent free energies of activation of the  $i$ -th step. These free energies are given by [401]

$$\begin{aligned} \Delta G_{DA}^* &= \Delta G_{DA}^{*0}, \\ \Delta G_{-DA}^* &= \Delta G_{DA}^{*0} - \Delta G_O^0, \\ \Delta G_{RA}^* &= \Delta G_{RA}^{*0} + \beta_{RA}e\eta, \\ \Delta G_{-RA}^* &= \Delta G_{RA}^{*0} - \Delta G_{OH}^0 - \beta_{RA}e\eta, \\ \Delta G_{RT}^* &= \Delta G_{RT}^{*0} + \beta_{RT}e\eta, \\ \Delta G_{-RT}^* &= \Delta G_{RT}^{*0} - \Delta G_{OH}^0 + \Delta G_O^0 - \beta_{RT}e\eta, \\ \Delta G_{RD}^* &= \Delta G_{RD}^{*0} + \beta_{RD}e\eta, \\ \Delta G_{-RD}^* &= \Delta G_{RD}^{*0} + \Delta G_{OH}^0 - \beta_{RD}e\eta, \end{aligned}$$

where  $e$  is the charge of a single electron and  $\eta$  is the applied overpotential i.e.  $\eta = E - E_{eq}$ . The free energies of activation at zero overpotential are denoted  $\Delta G_{DA}^{*0}$ ,  $\Delta G_{RA}^{*0}$ ,  $\Delta G_{RT}^{*0}$  and  $\Delta G_{RD}^{*0}$  while the free energies of adsorption at zero overpotential are denoted  $\Delta G_O^0$  and  $\Delta G_{OH}^0$ . These six free energies are the unknown kinetic parameters upon which the model is based. These values were obtained by Moore et al. in reference [27]. Detailed derivations for the expressions above can be found in [27, 397, 401]. An implementation of the kinetic model can be found in OpenFCST [6, 83].

### 3.5 Heat transport

Thermal effects cannot be neglected in single-cell and stack fuel cell models, especially in cases where phase change is dominant. High temperatures increase reaction rates and species transport while they reduce theoretical cell voltage and membrane conductivity (due to low water content) while increasing hydrogen crossover. If the cell is operated at high current density, localized excessive heat in the catalyst layers may lead to membrane degradation and the appearance of pin holes [402, 403]. Achieving a balance between positive and negative thermal effects, known as heat (or thermal) management, has been an active area of research for many years within the fuel cell mathematical modeling community and resulted in a large number of fuel cell models aiming at predicting the temperature distribution within the fuel cell which has been measured experimentally to change by several degrees [111].

Nguyen and White proposed a non-isothermal PEMFC model as early as 1993 [31]. Since then, more detailed non-isothermal fuel cell models were developed including three-dimensional studies by Wang et al. [404], Mazumder and Cole [405], and Ju et al. [406, 407]. Unfortunately, some key thermal effects were neglected in those models, such as the heat of the reaction [31], reversible heat of reaction [404, 405], ohmic losses due to electron transport [404, 406, 407], and heat sink due to water evaporation [406, 407]. Other 3D models also lacked a description of ohmic heating [5, 408]. Wang and Wang [409] improved the model by Ju et al. by including two-phase effects. However, a number of simplifying assumptions were still present in their model, e.g., isotropic and homogeneous properties of the fuel cell layers. Geometrical simplifications resulted in several 1D [410–412] and 2D [413–416] models that, due to their lower computational and implementation demands, allowed scientist to introduce more accurate physical representations, including anisotropy of the porous media [414, 415] and two-phase physics [410, 412, 415, 416]. These models however still contained some simplifications. For instance, Rowe and Li [410] and Ramousse et al. [411] did not take into account local thermal effects and assumed either a uniform cell temperature [411] or that the thermophysical properties were given at the average cell temperature [410]. Birgersson et al. [413] and Weber and Newman [412] considered interface models for catalyst layers, thereby neglecting any effects within the catalyst layer. Pasaogullari et al. [414] only studied the GDL and Zamel and Li [416] limited their model to the cathode. Bapat and Thynell [415] only considered heat conduction. Bhaiya et al. [308, 309] recently developed a single-phase, non-isothermal PEMFC model that took into account all thermal effects listed in previous publications, except for water condensation because all water in cathode was assumed to be generated in vapor form. This model was extended

later by Zhou et al. [304] into a two-phase, non-isothermal PEMFC model where the effects of condensation and enthalpy transport of liquid water are included.

Temperature distribution within a cell is governed by the energy conservation equation [32,160,303,417]. A single energy conservation equation is considered in this entry by assuming local thermal equilibrium between phases due to the large interstitial area of the porous materials in a PEMFC [308,309]. An energy conservation equation could be used for each phase (solid, gas and liquid), however this approach is not taken here and the interested reader is referred to references [418–420] for more information.

During the operation of a fuel cell, the main local sources and sinks of heat can be separated into three major categories depending on their nature: a) reaction heat; b) due to changes in the physical state of water; and c) ohmic heating. Reaction heat (reversible and irreversible) is released in the catalyst layers as the electrochemical reactions proceed. Liquid water is generated in the cathode during ORR and, depending on the local temperature, pressure, and humidity, may evaporate acting as a heat sink, be transported to cooler regions of the cell, and condense there creating a heat source (this is referred to as the heat pipe effect). Water sorption and desorption into and out of the electrolyte also release/absorb heat. Thermal effects may also affect the transport phenomena in PEMFCs, such as in the case of thermo-osmosis, i.e., the transport of sorbed water in the ionomer due to temperature gradients.

Based on the analysis above, treating all gases as ideal, and neglecting viscous heat dissipation, Soret and Dufour effects, the energy conservation equation inside a fuel cell takes the following form:

$$\varepsilon_v \frac{\partial(\rho_g \hat{h}_g)}{\partial t} + \nabla \cdot (\varepsilon_v \rho_g \hat{h}_g \mathbf{v}_g) = \nabla \cdot (\kappa^{\text{eff}} \nabla T) - \nabla \cdot \left( \sum \bar{H}_i \mathbf{N}_i \right) + \hat{S}_{\text{heat}} - \dot{W}_{\text{electrical}}, \quad (3.102)$$

where  $\hat{h}_g$  is the mass specific enthalpy of the gas,  $\mathbf{v}_g$  is the interstitial velocity of the gas mixture,  $\kappa^{\text{eff}}$  is the effective thermal conductivity,  $\bar{H}_i$  is the molar specific enthalpy of species  $i$ ,  $\mathbf{N}_i$  is the molar flux, and  $\hat{S}_{\text{heat}}$  and  $\dot{W}$  are volumetric rates of heat production and work done by the system, respectively.

The expression above depends on the mixture velocity and the molar flux of the different species in the porous media, therefore it has to be expanded for each fuel cell compartment and its final form depends on the mass transport model used as described in detail in reference [308]. In the cathode compartment of a PEMFC, a steady-state case with negligible convective gas transport, i.e.,  $\mathbf{v}_g \approx 0$ , and Fickian diffusion, the equation above can be expanded and further simplified to achieve the following expression [308],

$$\begin{aligned} & \nabla \cdot (\kappa^{\text{eff}} \nabla T) + D_{O_2, N_2}^{\text{eff}} c \nabla x_{O_2} \cdot (\nabla \bar{H}_{O_2} - \nabla \bar{H}_{N_2}) \\ & + D_{H_2O, N_2}^{\text{eff}} c \nabla x_{H_2O} \cdot (\nabla \bar{H}_{H_2O} - \nabla \bar{H}_{N_2}) - \mathbf{N}_\lambda \cdot \nabla \bar{H}_\lambda - \mathbf{N}_l \cdot \nabla \bar{H}_l + \hat{S}_{\text{heat}} = 0. \end{aligned} \quad (3.103)$$

For ideal gases, molar enthalpies of gaseous species are function of temperature alone. For sorbed water and liquid water, it is also assumed here that the molar specific enthalpies are only a function of temperature. Thus considering the sorbed water transport due to electro-osmotic drag, water diffusion and thermo-osmotic diffusion, the thermal transport equation inside the cathode catalyst layer can finally be expressed as:

$$\begin{aligned} & \nabla \cdot (\kappa^{\text{eff}} \nabla T) + D_{O_2, N_2}^{\text{eff}} c \left( \frac{\partial \bar{H}_{O_2}}{\partial T} - \frac{\partial \bar{H}_{N_2}}{\partial T} \right) \nabla T \cdot \nabla x_{O_2} \\ & + D_{H_2O, N_2}^{\text{eff}} c \left( \frac{\partial \bar{H}_{H_2O}}{\partial T} - \frac{\partial \bar{H}_{N_2}}{\partial T} \right) \nabla T \cdot \nabla x_{H_2O} + \frac{n_d \sigma_m^{\text{eff}}}{F} \frac{\partial \bar{H}_\lambda}{\partial T} \nabla T \cdot \nabla \phi_m \\ & + \frac{\rho_{\text{dry}}}{EW} D_\lambda^{\text{eff}} \frac{\partial \bar{H}_\lambda}{\partial T} \nabla T \cdot \nabla \lambda + \frac{1}{M_{H_2O}} D_T^{\text{eff}} \frac{\partial \bar{H}_\lambda}{\partial T} \nabla T \cdot \nabla T + \frac{\rho_l k_{rl}}{\mu_l} \frac{\partial \bar{H}_l}{\partial T} \nabla p_c \cdot \nabla T + \hat{S}_{\text{heat}} = 0, \end{aligned} \quad (3.104)$$

where in the cathode catalyst layer the term  $\hat{S}_{\text{heat}}$  contains the following:

1. The irreversible heat generation (efficiency losses) due to activation overpotential:

$$S_{\text{irrev,ORR}} = -i\eta = -i(\phi_s - \phi_m - E_{\text{ORR}}), \quad (3.105)$$

where  $\eta$  is the overpotential. Since  $\eta$  is negative for a cathodic reaction, a negative sign is placed in the formula,  $E_{\text{ORR}}$  is the equilibrium potential derived from the Nernst equation [199,401].

2. Reversible heat generation in the cathode catalyst layer due to ORR is:

$$S_{\text{rev,ORR}} = \frac{i}{2F} (-T \Delta \bar{S}_{\text{ORR}}) = \frac{i}{2F} (-T f_{\text{ORR}} \Delta \bar{S}_{\text{overall}}), \quad (3.106)$$

where  $\bar{S}_{\text{overall}}$  is the overall entropy change per mole of fuel ( $H_2$ ). Since the entropy of the half-cell reaction cannot be explicitly obtained, a factor  $f_{\text{ORR}}$ , is introduced to account for the fraction of reversible heat produced in the ORR.

3. Heat source term due to phase change:

$$S_{\text{phase,CL}} = M_{H_2O} S_{H_2O(\text{evap/cond})} \hat{L}_{\text{water}}, \quad (3.107)$$

where  $\hat{L}_{\text{water}}$  is the specific latent heat of vaporization/condensation of water, which is a function of temperature and is reported in [421].

4. The electronic and protonic Ohmic heating (irreversible):

$$S_{\text{ohmic,CL}} = \sigma_m^{\text{eff}} (\nabla \phi_m \cdot \nabla \phi_m) + \sigma_s^{\text{eff}} (\nabla \phi_s \cdot \nabla \phi_s). \quad (3.108)$$

5. Heat source term due to water vapor sorption/desorption in the ionomer

$$S_{\text{sorption,CL}} = \frac{k_t \rho_{\text{dry}}}{EW} (\lambda_{\text{eq}} - \lambda) \bar{H}_{\text{sorption}}, \quad (3.109)$$

where  $\bar{H}_{\text{sorption}}$  is heat release due to molar enthalpy change which corresponds to water vapor sorption.

Equation (3.104) can be implemented in order to estimate the temperature in the cathode CL. For the GDL and MPL the same equation can be used excluding the reaction heat terms, i.e., (3.105), (3.106), and water sorption term, i.e., (3.109). For the anode, a similar expression can be obtained. The interested reader is referred to [308].

## 4 Microscale simulation for parameter estimation

The governing equations of an MEA are described in Section 3. Critical to the proposed models are effective transport coefficients such as the effective diffusion coefficient in equation (3.37). Effective medium theories, such as Bruggemann correlation [34,44,422] (a particular case of equation (3.35)) and percolation theory [304,329,423] (shown in equation (3.32)), have traditionally been used to estimate the effective transport properties of the porous media by correlating the bulk transport properties to the solid or void volume fraction. However, these approximations do not take into account the intrinsic structure of the porous media and rely upon experimental measurements to estimate the exponents for the expressions in equations (3.32) and (3.35). A more accurate alternative to the effective medium theories is the use of microscale simulations to estimate the transport properties, coefficients for condensation and evaporation, and reaction effectiveness.

Advancements in microscopy techniques, such as x-ray computed tomography (X-CT) [29, 53, 55, 103, 424–431], scanning transmission x-ray microscopy (STXM) [432–434], and focused ion beam-scanning electron microscopy (FIB-SEM) [18, 52, 54, 55, 60, 335, 435], have enabled the visualization of the intrinsic structure of the fuel cell porous media. The choice of the technique to be used depends on the application and fuel cell layer to be visualized. Imaging techniques produce large image data sets which often require extensive image analysis to filter external noise and provide meaningful information about the underlying structure. To estimate the transport and electrochemical properties from the image data, a numerical tool must address the following aspects: a) image analysis of the data to produce binarized images; b) conversion of the binarized image data to a computational domain or mesh; c) modeling of the underlying physics, including simulation of the model, which involves providing parameters and discretization of the equations; and d) computational requirement.

Image analysis depends on the microscopy technique used to obtain the data. Details for image analysis can be found in the references for the different techniques mentioned above. The goal of image analysis is the segmentation of the structure into different phases (for X-CT and FIB-SEM). This binarized data set can then be used to generate a computational mesh. The mesh can be generated from the images in one of the following ways:

1. direct conversion of the image voxels into cells (for direct numerical simulation (DNS)) or lattice points (used for Lattice Boltzmann method (LBM)) [9, 12, 18, 366, 436–441] so that the mesh resolution is the voxel size;
2. use of triangulation algorithms to generate meshes from the images [29, 103, 442], typically used for CFD simulations; and
3. abstraction of the geometry to simplified networks [361, 428, 437, 440, 443–447], usually employed in pore network models (this method, however, results in the loss of morphological features of the original sample).

Berson et al. [448] reported that the direct conversion of voxels into a mesh, as is the case with the first approach, could lead to an overprediction of the interfacial area depending upon the mesh resolution. However, the use of meshing algorithms to smooth the digitized geometry might not be necessarily accurate, because the smallest

recoverable feature or interface depends on the voxel size. Also, it is unlikely that the solid surface in the fuel cell porous media, made up of heterogeneous materials, such as platinum supported on high surface area carbon in CLs, is smooth. Therefore, the first approach of converting image voxels into a computational mesh is acceptable for numerical simulation of the transport and electrochemical performance in the microstructures.

Numerical simulations in PEMFC microstructures have been performed either using the continuum approach (DNS) or LBM. However, for certain cases like diffusion in the CL, where the pore sizes are in the range of the mean free path of the gas molecules, the continuum approach is an approximation. This has led to the use of higher order LBM for such cases [15, 424, 449]. However, the large computational cost associated with the LBM (e.g., 6 hours on 320 cores for 8 million lattice points without consideration of Knudsen effects [15]) makes it unfeasible for performing optimization studies. This, in conjunction with the similar results obtained using continuum and LBM simulations for  $\text{Kn} \sim 1$  [14], has led to the continued use of the continuum approach to describe the physics in microstructures. In this Section, continuum equations used to compute the effective transport properties for the microstructures are described. Since the effective properties depend only on the steady-state fluxes, transient effects are ignored in the presented models.

Charge transport in the microstructures is simulated using Ohm's law [13, 366, 431, 439, 442, 450, 451],

$$\nabla \cdot (\boldsymbol{\sigma} \nabla \phi) = 0, \quad (4.1)$$

where  $\boldsymbol{\sigma}$  is either the bulk electronic or protonic conductivity tensor of the material and  $\phi$  is either the electronic or protonic potential, depending upon the phase under study. Usually, equation (4.1) is simulated in the solid phase of the microstructures, corresponding to the platinum and carbon in the CL and carbon fibers in the GDL. Therefore,  $\phi$  is usually the electronic potential except when the equation is simulated in the ionomer or liquid water phase of the CL where it would be the protonic potential. It is important to note that the source term (usually written on the right side) in equation (4.1) is zero. This is because the effective conductivity is assumed to be a function of the geometry and material of the layer and independent of the electrochemical reactions in the layer. To compute the effective conductivity in the Cartesian directions (X, Y and Z), equation (4.1) is solved with the boundary conditions

$$\begin{aligned} \phi &= \phi^{\text{in}} \text{ on } \Gamma_1, \\ \phi &= \phi^{\text{out}} \text{ on } \Gamma_2, \text{ and} \\ (\boldsymbol{\sigma} \nabla \phi) \cdot \mathbf{n} &= 0 \text{ (no-flux condition) everywhere else,} \end{aligned} \quad (4.2)$$

where  $\phi^{\text{in}}$  is the potential at the inlet plane,  $\phi^{\text{out}}$  is the potential at the outlet plane,  $\mathbf{n}$  is the outward normal vector to a surface, and  $\Gamma_1$  and  $\Gamma_2$  are the inlet and outlet cross-section planes, respectively, in the direction in which the effective conductivity is to be computed. For example, to compute the effective conductivity in the X-direction, i.e.,  $\sigma_{XX}^{\text{eff}}$  component of the conductivity tensor,  $\Gamma_1$  and  $\Gamma_2$  would be the YZ planes at the X-inlet and X-outlet. The no-flux boundary condition in equations (4.2) is used to prevent the charge transport across the solid-void interface and assume symmetry on all the outer planes except the inlet and outlet plane. By solving equation (4.1) with boundary conditions given by (4.2), the total current,  $I$ , leaving through the outlet plane,  $\Gamma_2$ , can be computed. This can be used to compute the effective conductivity,  $\sigma^{\text{eff}}$ , using

$$\sigma^{\text{eff}} = I \frac{L}{A(\phi^{\text{in}} - \phi^{\text{out}})}, \quad (4.3)$$

where  $L$  is the distance between the inlet and outlet planes, and  $A$  is the cross-section area of the outlet plane.

The effective thermal conductivity of the solid phase in the microstructures can be computed using heat conservation based on Fourier's law [450–452],

$$\nabla \cdot (\boldsymbol{\kappa} \nabla T) = 0, \quad (4.4)$$

where  $\boldsymbol{\kappa}$  is the bulk thermal conductivity tensor of the solid phase material in the microstructure. The thermal transport is considered to take place primarily in the solid phase due to difference of 3-4 orders of magnitude between the thermal conductivity of air and carbon (which is the primary material for most of the fuel cell porous media). Boundary conditions similar to equation (4.2) can be used by replacing  $\phi$  with  $T$  and  $\boldsymbol{\sigma}$  with  $\boldsymbol{\kappa}$ . It is assumed that the gas and solid are at a thermal equilibrium near the solid-void interface, therefore the no-flux boundary condition can be used at solid-void interface. Further, it is assumed that symmetry conditions apply at the outer planes of the domain except the inlet,  $\Gamma_1$ , and outlet,  $\Gamma_2$ , planes. Similar to the charge transport, equation (4.4) can be solved with the given boundary conditions, to compute the total heat flow rate,  $Q$ , through the outlet plane which can be used to compute the effective thermal conductivity,  $\kappa^{\text{eff}}$ , using equation (4.3) with  $I$ ,  $\phi$  and  $\sigma^{\text{eff}}$  replaced by  $Q$ ,  $T$  and  $\kappa^{\text{eff}}$ , respectively.

The thermal and charge transport equations presented here ignore the the local contact resistances that might exist between the particles in the microstructure. Kotaka et al. [431] compared the numerically computed effective electronic conductivity, using equation (4.1), with experimentally measured values for GDLs and MPLs and found that the numerical values were 27-32% higher than the experimental values for the GDL and 39 times the experimental value for the MPL. They attributed the huge discrepancy, especially for the MPL sample, to the contact resistance between carbon particles. The effect of contact resistances has also been shown by Espinola et al. [453], where the experimentally measured electrical conductivity for carbon powders was shown to be a function of compression pressure. These results indicate that the contact resistance between particles in porous layers made of carbon powder based materials, such as MPLs and CLs, is important to accurately estimate the effective electronic conductivity of these materials. Since thermal transport is also assumed to take place via conduction through the solid material, a similar thermal contact resistance should be accounted for in the thermal transport model.

Gas transport in the pores of the microstructures is commonly studied using the steady-state form of Fick's second law of diffusion [13, 18, 448, 451], given in equation (3.37). In this case, the diffusion coefficient for species  $i$ ,  $D_i$ , is defined as the bulk diffusion coefficient of species  $i$  in the gas for GDLs, where the Knudsen effects are negligible, and using the Bosanquet equation for CLs and MPLs, where pore sizes are in the range of the mean free path of the gas molecules [13, 18, 448, 451]. In the latter case, the diffusion coefficient is given by

$$\frac{1}{D_i} = \frac{1}{\mathcal{D}_{ij}} + \frac{1}{D_i^K}, \quad (4.5)$$

where  $D_i^K$  is the Knudsen diffusion coefficient for species  $i$ , given by equation (3.36). Since the Knudsen diffusion coefficient depends on the local pore radius, it is specified locally by computing the local pore radius (using sphere fitting [18, 29], average of the wall distance in different directions [13, 439]), or using an effective pore radius for the entire domain [10]. Boundary conditions similar to equation (4.2) can be used by replacing  $\phi$  with  $x_i$  and  $\sigma$  with  $D_i$ . The total flow rate of species  $i$  at the outlet,  $\dot{N}_i$ , can be used to compute the effective diffusivity,  $D_i^{\text{eff}}$ , using equation (4.3) by replacing  $I$ ,  $\phi$  and  $\sigma^{\text{eff}}$  with  $\dot{N}_i$ ,  $x_i$  and  $D_i^{\text{eff}}$ , respectively.

Electrochemical reactions have mainly been studied on the cathode CL microstructure due to the sluggishness of the ORR. These studies have been performed on stochastic [7–15] and FIB-SEM CL reconstructions [16–18]. Chen et al. [15] have used LBM to simulate the electrochemical reactions on a CL reconstruction, but all other studies have used either the finite volume or the finite element methods. Most of the prior studies have used Butler-Volmer or Tafel kinetics to estimate the ORR. As discussed in Section 3.4, the ORR is a multi-step reaction where the rate determining step depends on the overpotential. Therefore, the double trap [397] or the modified double trap model [388], presented in Section 3.4, would be more appropriate. Sabharwal et al. [18] used the double trap model to study the ORR on a FIB-SEM reconstruction of the CL. However, they assumed constant overpotential in the simulation domain.

The electrochemical reactions in the CL microstructure are studied by simulating equation (3.63) in the ionomer phase, equation (3.64) in the carbon and platinum phase, and the steady-state form of equation (3.37) in the pore phase. These three equations are coupled using the source term which depends on the reaction occurring on the Pt surface and can be computed using the kinetic models in Section 3.4. For FIB-SEM and nano-CT imaging, only solid and pore phases can be reconstructed, therefore, the solid phase cannot be separated into carbon, platinum, and ionomer phases. If the domain is small enough so that the overpotential can be assumed constant, then the model proposed by Sabharwal et al. [18] can be used, where only the oxygen diffusion is solved in the pore phase using equation (3.37) (where species  $i$  would now be  $O_2$ ) with boundary conditions

$$\begin{aligned} x_{O_2} &= x_{O_2}^{\text{in}} \quad \text{at all external walls,} \\ (-D_{O_2} c_{\text{tot}} \nabla x_{O_2}) \cdot \mathbf{n} &= \frac{j}{4F} A_{Pt, \text{slg}} \quad \text{at } \Gamma_{\text{slp}}. \end{aligned} \quad (4.6)$$

where  $\Gamma_{\text{slp}}$  indicates the solid-pore interface,  $j$  is the current density per unit area of Pt, and  $A_{Pt, \text{slg}}$  is the ratio of active platinum area in the simulation domain to the solid-pore interface area. The boundary conditions given by equations (4.6) assume that the domain is small enough that the oxygen concentrations at the outer walls of the domain are identical and that the reaction only takes place at the solid-pore interface.

An oxygen transport resistance due to catalyst-ionomer interactions has been proposed as a key factor limiting cathode performance [18, 51, 182, 183, 454, 455]. Zhang et al. [17] and Sabharwal et al. [18] accounted for the mass transport resistance due to the ionomer films in their electrochemical models. The model presented by Sabharwal et al. [18] assumes a fictitious thin film of ionomer to be present at the solid-pore interface as shown in Figure 4.1.

Therefore, for the reaction to take place at the solid-ionomer interface, additional resistances, in the form of an interfacial resistance (considered in the model at the ionomer-gas interface) and diffusion resistance through the

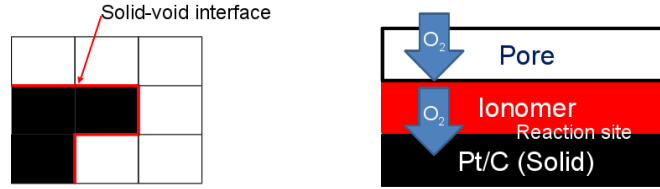


Figure 4.1: Illustration of the solid (black) - pore (white) domain of the CL microstructure with the fictitious ionomer film (red).

ionomer film, are introduced. The mathematical form of these resistances is

$$\begin{aligned}
 (-D_{O_2} c \nabla x_{O_2}) \cdot \mathbf{n} &= -k_{O_2} (c_{O_{2,glf}} - c_{O_{2,glf}}^{eq}), \\
 &= \frac{D_{O_2}^{film}}{\delta_N} (c_{O_{2,glf}} - c_{O_2}^{react}), \\
 &= \frac{j(c_{O_2}^{react}, \phi_s, \phi_m)}{4F},
 \end{aligned} \tag{4.7}$$

where  $k_{O_2}$  is the oxygen dissolution rate in the ionomer,  $D_{O_2}^{film}$  is the oxygen diffusion coefficient in the ionomer film,  $\delta_N$  is the thickness of the ionomer film,  $c_{O_{2,glf}}$  is the concentration of oxygen in the ionomer phase at the gas-ionomer interface,  $c_{O_{2,glf}}^{eq}$  is the equilibrium oxygen concentration obtained from Henry's law using the partial pressure of oxygen in the gas phase, and  $c_{O_2}^{react}$  is the oxygen concentration at the ionomer-catalyst interface used for calculating  $j$ . When solved together, equations (3.37), (4.6), and (4.7) can be used to estimate the electrochemical performance in the CL microstructure assuming constant overpotential in the domain. The results of the electrochemical simulations can be used in macro-scale simulations to provide a better estimate of the local current density in different regions of the CL based on the macro-scale overpotentials and oxygen concentrations. Recently, it has been suggested that the interfacial resistance is likely due to platinum-ionomer interactions instead of oxygen dissolution [454]. In this latter case, the functional form of the equation would remain the same but the physical meaning of  $k_{O_2}$  would change.

Water management is critical to the operation of a PEMFC. The operation of a fuel cell under wet (high RH) and cold (low temperature) conditions can lead to the production of excess liquid water, which can affect the reactant transport and, in severe cases, cause complete shutdown of the cell due to reactant starvation. It is therefore crucial to understand the effect of liquid water saturation on the gas transport and electrochemical reactions in PEMFC. Micro-scale models can be used to correlate the morphology of the porous media to the liquid water movement and the corresponding impact on the gas pathways. Liquid water transport in microstructures has been studied using LBM [363, 437, 440, 441, 456–458], PNM [361, 427, 428, 437, 443–447, 459, 460], and full morphology (FM) models [54, 437, 440, 461–463]. PNM is the most commonly used approach to study liquid water intrusion in the fuel cell porous media microstructures. As described earlier, PNMs abstract the geometry into a network of pores and throats which can be generated using microscopy images such as X-CT [363, 428, 464] or random networks [361, 445–447, 459] calibrated with experimental data such as porosity, mercury intrusion porosimetry, or saturation-pressure profiles. PNMs are extremely fast and provide a computationally inexpensive means of obtaining pressure-saturation profiles for porous media and computing the effective transport properties as functions of saturation for the abstract network. FM models study the liquid intrusion in the porous media using a quasi-static capillary-driven water front approach, in which the following equation is used to compute the capillary pressure required to intrude a pore with liquid water:

$$p_c = \frac{2\gamma \cos\theta}{r_p},$$

where  $\gamma$  is the surface tension of water, and  $\theta$  is the contact angle.

The major advantage of FM over PNM is that no geometry abstraction is required and the liquid water transport and corresponding transport properties can be studied on the actual microstructure. However, FM model is computationally more expensive than PNM [440]. LBM can be used to study the intricate liquid water dynamics in the microstructures as opposed to the quasi-static approach used by PNM and FM, but is computationally very expensive [440]. The details of the different models are not described in this Section and can be found in the references listed above.

Interphase mass transfer between the gas and liquid phase is another mode for the transport of water in the PEMFC layers. Microscale simulations can be used to compute the evaporation/condensation rates in the different porous media. One such study was performed by Zenyuk et al. [465], who measured the evaporation rates in a GDL

microstructure at different saturations. Using X-CT, they reconstructed the partially wetted GDL microstructures to extract the liquid water surface mesh. Diffusive gas transport was simulated using the Maxwell-Stefan equation (3.8), assuming that the region above the liquid water surface was a macro-homogeneous GDL and partial pressure of water vapor near the liquid water surface was equal to the saturation pressure for water vapor. The results of the simulation were used to compute the evaporation rates by measuring the flux of water through the liquid-gas interface. The approach used by Zenyuk et al. [465] provided good agreements with the experimentally measured evaporation rates. However, better models are needed to accurately take into account the morphology of the microstructures and the local water distributions which might not always be connected and planar. Accurate estimates of the evaporation/condensation rates in different porous media are required for the macro-scale models to describe the two-phase flow in PEMFCs and optimize the functionality of different layers.

## 5 Implementation

There are mainly three categories of PEFC models: a) channel models [231, 258, 333, 466–469]; b) through-the-channel MEA models [161, 209, 304, 309, 327, 327–331, 338, 345–350, 406, 470]; and, c) along-the-channel and fuel cell models which account for both gas channels and MEA sandwich [4, 417, 471].

Some channel models consider single-phase flow [466], however, most of the models studying mass transport in the channel include both air and liquid water in their formulation [231, 258, 333, 467–469]. Early two-phase models, e.g., mixture (or  $M^2$ ) models, solved the transport problem for the gas-liquid mixture using a variable phase composition formulation [333]. The transport of the gas mixture is solved using mass (3.1) and momentum (3.2) conservation equations, and saturation is obtained from the water concentration in the mixture. Other two-phase flow models in channels solve Navier-Stokes equations (3.2) and continuity equation (3.1) for both air and liquid water as immiscible phases. Although ANSYS Fluent is the software used for the majority of these studies [231, 467–469], other works use COMSOL Multiphysics [466] or open-source packages such as Gerris flow solver (GFS) [258, 472]. Since ANSYS Fluent and COMSOL are commercial CFD packages, the above-mentioned studies do not include discussion on the implementation of the numerical models, and only the reference manual of each software is cited. Some authors, e.g., Wang et al. [467], included a short discussion on the numerical approach, specifying that some terms in the governing equations were implemented using user-specified functions. The only works that mention details on the implementation and solvers used in open-source packages are that from Theodorakakos et al. [258], and Jarauta et al. [233], the latter being implemented in the open source package Kratos Multiphysics [241].

A typical through-the-channel, single-phase, non-isothermal MEA model includes governing equations for gas, charge, water and heat transport. The transport of gaseous species in the MEA is modeled using Fick’s law of diffusion (equation (3.13)). Charge transport is commonly modeled using Ohm’s law (equation (3.61)). Transport of sorbed water in the membrane is modeled using equation (3.44). Heat transfer is modeled using equation (3.104). An example of single-phase non-isothermal MEA model is implemented in open-source software package OpenFCST v0.3 [83].

Two-phase, non-isothermal MEA models that account for the transport of liquid water are implemented using either a one-equation model based on saturation (equation (3.46)) or a two-equation model including Darcy’s law for the gas and liquid phases (equation (3.47) and (3.48)) together with a set of closure equations. Two-phase model implementations can be found in many modeling packages such as CFDesign [345], STAR-CCM+ [406], ANSYS Fluent [161, 328, 349], COMSOL Multiphysics [209], and OpenFCST [304, 309, 470]. One of the most complete fuel cell models is the one proposed by Zenyuk et al. [209]. Their governing equations are solved using the general solvers provided by COMSOL Multiphysics 5.0/5.1 [240] and MUMPS. A more recent two-phase model is developed by Zhou et al. [470] which is linearized using Newton-Raphson method, discretized using the Galekin finite element method, and solved using MUMPS in OpenFCST.

The models that include both gas flow channel and MEA sandwich are implemented in modeling packages such as ANSYS Fluent [4] and CFX [417, 471]. These models require a high computational power and the convergence can be very slow. For instance, the model proposed by Nguyen et al. [471] required about 6,000-8,000 iterations to achieve convergence.

The partial differential equations for the above mentioned numerical models are nonlinear. For example, the source terms for mass transport equations for oxygen and water vapor depend on current density, which depends on electronic and solid potentials and reactant availability (Table 3.1). Therefore, these equations must be linearized using Newton-Raphson and Picard methods

After a set of linear partial differential equations is obtained, discretization in space is performed. One option relies on using the finite volume method [235] for space discretization. This method is used in many commercial numerical simulation packages such as ANSYS Fluent [236] and STAR-CCM+ [237], and in open-source packages such as FastFC [84]. Another well-known method is the finite element method [239], which is available in commercial packages

such as COMSOL Multiphysics [240] and in open-source frameworks such as deal.ii [473] and OpenFCST [6,83]. Using both finite volume and finite element methods, the computational domain is discretized into small elements, known as the computational mesh. The resulting mesh must contain sufficient elements in order to obtain a grid-independent solution. The meshes can be classified into structured and unstructured meshes. In a structured mesh, all internal nodes are connected to the same number of neighbor nodes and the same element pattern is followed throughout the grid. In an unstructured mesh, the pattern may be irregular and no requirement on the number of vertices surrounding each node exists. Meshes can be refined based on an error estimator of the approximate solution (e.g., a posteriori error estimator developed by Kelly et al. [474]). Adaptive refinement is applied, for example, in OpenFCST [6,44]. To further improve the computational efficiency and avoid non-matching grids, domain decomposition methods (DDMs) are used. DDMs are implemented in commercial (e.g., COMSOL [240], ANSYS Fluent [236]) and open-source (e.g., OpenFOAM [238]) software.

For the reader interested in an open-source implementation of an MEA model, OpenFCST contains several models that can be downloaded and utilized to gain a better understanding of fuel cell modeling [6].

As described in Section 4, continuum models have been used to describe the physical processes in the microstructures of the fuel cell porous media. The governing equations for these models can be discretized using the finite volume method [11, 13, 14, 439, 451] or finite element method [18, 29, 103]. Additionally, when the electrochemical reactions are considered in a CL microstructure, the resulting system of equations might be non-linear. These equations are then linearized using Newton-Raphson method [13, 14, 439] or Picard method [18]. The governing equations can then be solved using commercial packages, such as ANSYS Fluent [236], COMSOL [240], and GEODICT® [475], or open-source software, such as OpenFCST [6,83]. Although not described in this entry, Lattice Boltzmann method and pore network models have also been used for microstructure simulations. Palabos [476] and OpenPNM [85,477] are examples of open-source software which employ LBM and PNM, respectively, to study the physics in the fuel cell porous media microstructures.

## 6 Conclusion

Substantial progress has been achieved in the area of fuel cell modeling since the pioneering work of Springer et al. [1] and Bernardi and Verbrugge [2] in the early 1990s. A deeper understanding of the critical physical phenomena occurring inside the fuel cell coupled with expanding computational resources have allowed researchers to consider higher dimensionality and complex physical and electrochemical processes that were initially neglected due to high computing costs, lack of experimental evidence of their importance and the difficulty of implementation. To date, several two and three-dimensional single and two-phase channel models have been proposed and novel formulations are still under development, such as the implementation of the generalized Navier-Stokes equations proposed by Kerkhof and Geboers [214] for multi-component transport or the embedded Lagrangian-Eulerian formulation proposed by Jarauta et al. [233]. MEA and full-cell models have transitioned from one-dimensional, single-phase models with limited access to the source code, to open-source implementations of two-phase, non-isothermal MEA models that include multi-step reaction kinetics and local mass transport losses [304].

This entry provided an overview of the governing equations used in channel, MEA and full-cell proton exchange membrane fuel cell modeling. Starting with the function and composition of each component of a PEMFC, this entry provided the most common mathematical models for mass, charge and energy transport in PEMFCs, as well as the electrochemical reactions of hydrogen oxidation and oxygen reduction. All models are derived following several levels of detail so that the material of this entry can serve as a base for developing novel PEMFC mathematical models with varying levels of complexity depending on the simplifying assumptions. Due to nonlinearity and stiffness, the resulting numerical models are hard to solve and require an adequate solution approach at all levels from discretization (in both space and time) to the selection of appropriate linear, non-linear and transient solvers. Therefore, a section on implementation details was also provided outlining the solution methodologies used in the literature and highlighting the importance of open-source numerical software.

The governing equations discussed in this entry for full-cell and MEA modeling depend on many effective transport properties, such as effective diffusivity. Obtaining effective transport properties and accounting for local transport effects in the porous media, such as local transport resistances or evaporation, requires tedious experiments that are usually time consuming. FIB-SEM and CT imaging can now provide three-dimensional reconstructions of GDLs, CLs and MPLs with high resolution. This entry showed how numerical modeling can be used to interpret the imaging data in order to extract effective transport properties under dry and wet conditions, and reaction rates per unit volume.

## 7 Future directions

The level of detail and overall complexity of PEMFC mathematical models has drastically increased since 1990's. It is clear, however, that future work is still required in order to remove simplifying assumptions and include additional phenomena. Physical processes such as platinum dissolution and coarsening, carbon corrosion, compression effects, membrane swelling and mechanical and chemical degradation and local mass transport losses have been shown to be critical to fuel cell performance and durability [21, 33]. These processes take place at different time scales and therefore, they are seldom integrated into detailed full-cell or MEA models. Numerical models need to be developed with adaptive time stepping algorithms to capture the dynamics of the fuel cell at the various time scales.

Future numerical models should also be able to integrate PEMFC transport and electrochemical processes across various length scales. This requires developing coupling strategies to introduce nano-scale information from molecular dynamics and density functional theory, and micro-scale information from microstructure simulations from FIB-SEM and CT image reconstructions in the macro-scale models. Progress has been made recently in this regard by coupling a GDL pore network model (PNM) to a volume averaged macro-scale MEA model [338, 400]. However for CLs much more complex couplings might be required, especially to introduce information regarding the electrochemical processes occurring at the pore scale.

In addition to the structure of the porous media, the structure of the interface between the different layers has also been shown to affect the local ohmic resistances [130] and water accumulation [131–134] in the PEFC. Although commonly ignored in the macro-scale models, these interfaces can significantly affect the transport processes in the PEFC and therefore, need to be accounted for in the full-cell models [33]. It is therefore necessary to develop efficient coupling methods to integrate the information about the structure of the porous media and their interfaces into the macro-scale models.

In the area of micro-scale simulations, further development is needed in order to seamlessly integrate modeling into image analysis protocols. Mathematical characterization of the porous media microstructures using multiple statistical functions has seldom been performed in literature. Future studies should aim to characterize the difference in the structure of porous media with different composition and fabrication methods. Correlations also need to be developed between the structure and properties of the porous media. Models to predict ionic transport and wettability of thin ionomer films in the CL and the local mass transport losses identified at the catalyst sites [182, 183, 454, 455] are also required. Recent studies have tried to account for the effects of the ionomer film at micro- [17, 18] and macro-scales [51, 158] however much work is required to understand the mechanism and mathematical functional form of this so-called interfacial resistance.

Future work will therefore be required in the next decade to further extend, and validate with respect to experimental data, current model implementations. Given the complexity of the current models, such extensions are likely to be only possible within the framework of an open-source collaboration. Non-isothermal MEA models, as well as companion simplified models, that have been validated with respect to experimental data [309] and micro-scale models are already publicly available in the open-source fuel cell software OpenFCST at [www.openfcst.org](http://www.openfcst.org). Open-source software should serve as a foundation for further fuel cell model development. It is important that the research community as a collective contributes to the development of open-source software so that the existing knowledge base can be expanded in an efficient manner.

## Index terms

Polymer electrolyte fuel cells, hydrogen energy, numerical modeling of PEFCs

## Primary literature

- [1] Springer T, Zawodzinski T, Gottesfeld S (1991) Polymer electrolyte fuel cell model. *J Electrochem Soc*, 138(8):2334–2342
- [2] Bernardi DM, Verbrugge MW (1992) Mathematical model of the solid-polymer-electrolyte fuel cell. *J Electrochem Soc*, 139(9):2477–2491
- [3] Shimpalee S, Dutta S, Van Zee J (2000) Numerical prediction of local temperature and current density in a PEM fuel cell. *ASME Publ HTD*, 366:1–10
- [4] Dutta S, Shimpalee S, Van Zee J (2001) Numerical prediction of mass-exchange between cathode and anode channels in a PEM fuel cell. *Int J Heat Mass Transf*, 44(11):2029–2042

- [5] Berning T, Lu D, Djilali N (2002) Three-dimensional computational analysis of transport phenomena in a PEM fuel cell. *J Power Sources*, 106(1-2):284–294
- [6] Secanell M, Putz A, Wardlaw P, Zingan V, Bhaiya M, Moore M, Zhou J, Balen C, Domican K (2014) Open-FCST: an open-source mathematical modelling software for polymer electrolyte fuel cells. *ECS Transactions*, 64(3):655–680
- [7] Wang G, Mukherjee PP, Wang CY (2006) Direct numerical simulation (DNS) modeling of PEFC electrodes Part II. Random microstructure. *Electrochimica Acta*, 51:3151–3160
- [8] Wang JX, Springer TE, Adzic RR (2006) Dual-pathway kinetic equation for the hydrogen oxidation reaction on Pt electrodes. *J Electrochem Soc*, 153(9):A1732–A1740
- [9] Wang G, Mukherjee PP, Wang CY (2007) Optimization of polymer electrolyte fuel cell cathode catalyst layers via direct numerical simulation modeling. *Electrochimica Acta*, 52(22):6367–6377
- [10] Mukherjee P, Wang CY (2006) Stochastic microstructure reconstruction and direct numerical simulation of the PEFC catalyst layer. *J Electrochem Soc*, 153(5):A840–A849
- [11] Mukherjee PP, Wang CY (2007) Direct numerical simulation modeling of bilayer cathode catalyst layers in polymer electrolyte fuel cells. *J Electrochem Soc*, 154(11):B1121–B1131
- [12] Siddique N, Liu F (2010) Process based reconstruction and simulation of a three-dimensional fuel cell catalyst layer. *Electrochimica Acta*, 55(19):5357–5366
- [13] Lange KJ, Sui PC, Djilali N (2010) Pore scale simulation of transport and electrochemical reactions in reconstructed PEMFC catalyst layers. *J Electrochem Soc*, 157(10):B1434–B1442
- [14] Lange KJ, Sui PC, Djilali N (2012) Determination of effective transport properties in a PEMFC catalyst layer using different reconstruction algorithms. *J Power Sources*, 208:354–365
- [15] Chen L, Wu G, Holby EF, Zelenay P, Tao WQ, Kang Q (2015) Lattice Boltzmann pore-scale investigation of coupled physical-electrochemical processes in C/Pt and non-precious metal cathode catalyst layers in proton exchange membrane fuel cells. *Electrochimica Acta*, 158:175–186
- [16] Zhang X, Ostadi H, Jiang K, Chen R (2014) Reliability of the spherical agglomerate models for catalyst layer in polymer electrolyte membrane fuel cells. *Electrochimica Acta*, 133:475–483
- [17] Zhang X, Gao Y, Ostadi H, Jiang K, Chen R (2015) Method to improve catalyst layer model for modelling proton exchange membrane fuel cell. *J Power Sources*, 289:114–128
- [18] Sabharwal M, Pant L, Putz A, Susac D, Jankovic J, Secanell M (2016) Analysis of catalyst layer microstructures: from imaging to performance. *Fuel Cells*, 16(6):734–753
- [19] Konno N, Mizuno S, Nakaji H, Ishikawa Y (2015) Development of compact and high-performance fuel cell stack. *SAE Int J Altern Powertrains*, 4(1):123–129
- [20] Kongkanand A, Mathias M (2016) The priority and challenge of high-power performance of low-platinum proton-exchange membrane fuel cells. *J Phys Chem Lett*, 7(7):1127–1137
- [21] Borup R, Meyers J, Pivovar B, Kim Y, Mukundan R, Garland N, Myers D, Wilson M, Garzon F, Wood D, Zelenay P, More K, Stroh K, Zawodzinski T, Boncella J, McGrath J, Inaba M, Miyatake K, Hori M, Ota K, Ogumi Z, Miyata S, Nishikata A, Siroma Z, Uchimoto Y, Yasuda K, Kimijima KI, Iwashita N (2007) Scientific aspects of polymer electrolyte fuel cell durability and degradation. *Chem Rev*, 107(10):3904–3951
- [22] Maranzana G, Lamibrac A, Dillet J, Lottin O (2015) Startup (and shutdown) model for polymer electrolyte membrane fuel cells. *J Electrochem Soc*, 162(7):F694–F706
- [23] Sethuraman VA, Weidner JW, Motupally S, Protsailo LV (2008) Hydrogen peroxide formation rates in PEMFC anode and cathode. *J Electrochem Soc*, 155(1):B50–B57
- [24] Secanell M, Wishart J, Dobson P (2011) Computational design and optimization of fuel cells and fuel cell systems: a review. *J Power Sources*, 196(8):3690–3704

- [25] Martins J, Lambe A (2013) Multidisciplinary design optimization: a survey of architectures. *AIAA J*, 51(9):2049–2075
- [26] Carnes B, Djilali N (2005) Systematic parameter estimation for PEM fuel cell models. *J Power Sources*, 144(1):83–93
- [27] Moore M, Putz A, Secanell M (2013) Investigation of the ORR using the double-trap intrinsic kinetic model. *J Electrochem Soc*, 160(6):F670–F681
- [28] Novitski D, Kosakian A, Weissbach T, Secanell M, Holdcroft S (2016) Electrochemical reduction of dissolved oxygen in alkaline, solid polymer electrolyte films. *J Am Chem Soc*, 138(47):15465–15472
- [29] Litster S, Epting WK, A.Wargo E, Kalidindi SR, Kumbur EC (2013) Morphological analyses of polymer electrolyte fuel cell electrodes with nano-scale computed tomography imaging. *Fuel Cells*, 13(5):935–945
- [30] Kulikovskiy A, Divisek J, Kornyshev A (1999) Modeling the cathode compartment of polymer electrolyte fuel cells: dead and active reaction zones. *J Electrochem Soc*, 146(11):3981–3991
- [31] Nguyen T, White R (1993) A water and heat management model for proton-exchange-membrane fuel cells. *J Electrochem Soc*, 140(8):2178–2186
- [32] Gurau V, Liu H, Kakac S (1998) Two-dimensional model for proton exchange membrane fuel cells. *AIChE J*, 44(11):2410–2422
- [33] Weber AZ, Borup RL, Darling RM, Das PK, Dursch TJ, Gu W, Harvey D, Kusoglu A, Litster S, Mench MM, Rangachary Mukundan, Owejan JP, Pharoah JG, Secanell M, Zenyuk IV (2014) A critical review of modeling transport phenomena in polymer-electrolyte fuel cells. *J Electrochem Soc*, 161(12):F1254–F1299
- [34] Weber AZ, Newman J (2004) Modeling transport in polymer-electrolyte fuel cells. *Chem Rev*, 104(10):4679–4726
- [35] Wang CY (2004) Fundamental models for fuel cell engineering. *Chem Rev*, 104:4727–4766
- [36] Haraldsson K, Wipke K (2004) Evaluating PEM fuel cell system models. *J Power Sources*, 126:88–97
- [37] Biyikoğlu A (2005) Review of proton exchange membrane fuel cell models. *Int J Hydrog Energy*, 30:1181–1212
- [38] Cheddie D, Munroe N (2005) Review and comparison of approaches to proton exchange membrane fuel cell modeling. *J Power Sources*, 147(1-2):72–84
- [39] Siegel C (2008) Review of computational heat and mass transfer modeling in polymer-electrolyte-membrane (PEM) fuel cells. *Energy*, 33(9):1331–1352
- [40] Song GH, Meng H (2013) Numerical modeling and simulation of PEM fuel cells: Progress and perspective. *Acta Mech Sinica*, 29(3):318–334
- [41] Eikerling M, Kulikovskiy A (2014), *Polymer electrolyte fuel cells: physical principles of materials and operation*. CRC Press
- [42] Kulikovskiy AA (2010), *Analytical modelling of fuel cells*. Elsevier
- [43] Eikerling M, Kornyshev A (1998) Modelling the performance of the cathode catalyst layer of polymer electrolyte fuel cells. *J Electroanal Chem*, 453(1-2):89–106
- [44] Secanell M, Karan K, Suleman A, Djilali N (2007) Multi-variable optimization of PEMFC cathodes using an agglomerate model. *Electrochimica Acta*, 52(22):6318–6337
- [45] Mangal P, Pant LM, Carrigy N, Dumontier M, Zingan V, Mitra S, Secanell M (2015) Experimental study of mass transport in PEMFCs: through plane permeability and molecular diffusivity in GDLs. *Electrochimica Acta*, 167:160–171
- [46] Zamel N, Li X (2013) Effective transport properties for polymer electrolyte membrane fuel cells - with a focus on the gas diffusion layer. *Prog Energy Combust Sci*, 39(1):111–146

- [47] Shen J, Zhou J, Astrath NG, Navessin T, Liu ZSS, Lei C, Rohling JH, Bessarabov D, Knights S, Ye S (2011) Measurement of effective gas diffusion coefficients of catalyst layers of PEM fuel cells with a Loschmidt diffusion cell. *J Power Sources*, 196(2):674–678
- [48] Chan C, Zamel N, Li X, Shen J (2012) Experimental measurement of effective diffusion coefficient of gas diffusion layer/microporous layer in PEM fuel cells. *Electrochimica Acta*, 65:13–21
- [49] Owejan JP, Owejan JE, Gu W (2013) Impact of platinum loading and catalyst layer structure on PEMFC performance. *J Electrochem Soc*, 160(8):F824–F833
- [50] Weber A, Kusoglu A (2014) Unexplained transport resistances for low-loaded fuel-cell catalyst layers. *J Mater Chem A*, 2(41):17207–17211
- [51] Secanell M, Putz A, Shukla S, Wardlaw P, Bhaiya M, Pant LM, Sabharwal M (2015) Mathematical modelling and experimental analysis of thin, low-loading fuel cell electrodes. *ECS Transactions*, 69(17):157–187
- [52] Ziegler C, Thiele S, Zengerle R (2011) Direct three-dimensional reconstruction of a nanoporous catalyst layer for a polymer electrolyte fuel cell. *J Power Sources*, 196(4):2094–2097
- [53] Epting W, Gelb J, Litster S (2012) Resolving the three-dimensional microstructure of polymer electrolyte fuel cell electrodes using nanometer-scale X-ray computed tomography. *Adv Funct Mater*, 22(3):555–560
- [54] Zhang X, Gao Y, Ostadi H, Jiang K, Chen R (2014) Modelling water intrusion and oxygen diffusion in a reconstructed microporous layer of PEM fuel cells. *Int J Hydrog Energy*, 39(30):17222–17230
- [55] Wargo E, Kotaka T, Tabuchi Y, Kumbur E (2013) Comparison of focused ion beam versus nano-scale X-ray computed tomography for resolving 3-D microstructures of porous fuel cell materials. *J Power Sources*, 241:608–618
- [56] Thiele S, Fürstenthaupt T, Banham D, Hutzenlaub T, Birss V, Ziegler C, Zengerle R (2013) Multiscale tomography of nanoporous carbon-supported noble metal catalyst layers. *J Power Sources*, 228:185–192
- [57] Lopez-Haro M, Guétaz L, Printemps T, Morin A, Escribano S, Jouneau PH, Bayle-Guillemaud P, Chandezon F, Gebel G (2014) Three-dimensional analysis of Nafion layers in fuel cell electrodes. *Nat Commun*, 5
- [58] Paul DK, Karan K (2014) Conductivity and wettability changes of ultrathin Nafion films subjected to thermal annealing and liquid water exposure. *The J Phys Chem C*, 118(4):1828–1835
- [59] Liu H, Epting W, Litster S (2015) Gas transport resistance in polymer electrolyte thin films on oxygen reduction reaction catalysts. *Langmuir*, 31(36):9853–9858
- [60] Cecen A, Wargo E, Hanna A, Turner D, Kalidindi S, Kumbur E (2012) 3-D microstructure analysis of fuel cell materials: spatial distributions of tortuosity, void size and diffusivity. *J Electrochem Soc*, 159(3):B299–B307
- [61] Wang XD, Xu JL, Yan WM, Lee DJ, Su A (2011) Transient response of PEM fuel cells with parallel and interdigitated flow field designs. *Int J Heat Mass Transf*, 54(11):2375–2386
- [62] Peng J, Shin J, Song T (2008) Transient response of high temperature PEM fuel cell. *J Power Sources*, 179(1):220–231
- [63] Jo A, Lee S, Kim W, Ko J, Ju H (2015) Large-scale cold-start simulations for automotive fuel cells. *Int J Hydrog Energy*, 40(2):1305–1315
- [64] Ko J, Ju H (2012) Comparison of numerical simulation results and experimental data during cold-start of polymer electrolyte fuel cells. *Appl Energy*, 94:364–374
- [65] Kim H, Jeon S, Cha D, Kim Y (2016) Numerical analysis of a high-temperature proton exchange membrane fuel cell under humidified operation with stepwise reactant supply. *Int J Hydrog Energy*, 41(31):13657–13665
- [66] Yin Y, Wang J, Yang X, Du Q, Fang J, Jiao K (2014) Modeling of high temperature proton exchange membrane fuel cells with novel sulfonated polybenzimidazole membranes. *Int J Hydrog Energy*, 39(25):13671–13680
- [67] Chen X, Jia B, Yin Y, Du Q (2013), Numerical simulation of transient response of inlet relative humidity for high temperature PEM fuel cells with material properties. In *Advanced Materials Research*, volume 625, pages 226–229. *Trans Tech Publ*

- [68] Wu H, Berg P, Li X (2010) Modeling of PEMFC transients with finite-rate phase-transfer processes. *J Electrochem Soc*, 157(1):B1–B12
- [69] Verma A, Pitchumani R (2015) Analysis and optimization of transient response of polymer electrolyte fuel cells. *J Fuel Cell Sci Technol*, 12(1):011005
- [70] Gomez A, Raj A, Sasmito A, Shamim T (2014) Effect of operating parameters on the transient performance of a polymer electrolyte membrane fuel cell stack with a dead-end anode. *Appl Energy*, 130:692–701
- [71] Sousa T, Mamlouk M, Scott K, Rangel C (2012) Three dimensional model of a high temperature PEMFC. Study of the flow field effect on performance. *Fuel Cells*, 12(4):566–576
- [72] Songprakorp R (2008), Investigation of transient phenomena of proton exchange membrane fuel cells, PhD thesis, University of Victoria
- [73] Roy A, Serincan M, Pasaogullari U, Renfro M, Cetegen B (2009), Transient computational analysis of proton exchange membrane fuel cells during load change and non-isothermal start-up. In ASME 2009 7th International Conference on Fuel Cell Science, Engineering and Technology, pages 429–438. American Society of Mechanical Engineers
- [74] Wu H, Li X, Berg P (2007) Numerical analysis of dynamic processes in fully humidified PEM fuel cells. *Int J Hydrog Energy*, 32(12):2022–2031
- [75] Sousa T, Mamlouk M, Scott K (2010) A dynamic non-isothermal model of a laboratory intermediate temperature fuel cell using PBI doped phosphoric acid membranes. *Int J Hydrog Energy*, 35(21):12065–12080
- [76] Qu S, Li X, Ke C, Shao ZG, Yi B (2010) Experimental and modeling study on water dynamic transport of the proton exchange membrane fuel cell under transient air flow and load change. *J Power Sources*, 195(19):6629–6636
- [77] Bao C, Bessler W (2015) Two-dimensional modeling of a polymer electrolyte membrane fuel cell with long flow channel. Part I. Model development. *J Power Sources*, 275:922–934
- [78] Balliet R, Newman J (2010) Two-dimensional model for cold start in a polymer-electrolyte-membrane fuel cell. *ECS Transactions*, 33(1):1545–1559
- [79] Wang Y, Wang CY (2005) Transient analysis of polymer electrolyte fuel cells. *Electrochimica Acta*, 50(6):1307–1315
- [80] Wang C, Nehrir M, Shaw S (2005) Dynamic models and model validation for PEM fuel cells using electrical circuits. *IEEE Transactions on Energy Convers*, 20(2):442–451
- [81] Vang J, Andreasen S, Kær S (2012) A transient fuel cell model to simulate HTPEM fuel cell impedance spectra. *J Fuel Cell Sci Technol*, 9(2):021005
- [82] Secanell M (2007), Computational modeling and optimization of proton exchange membrane fuel cells, PhD thesis, University of Victoria
- [83] OpenFCST. <http://www.openfcst.org/>. Accessed on 06.30.2017
- [84] Fast-FC. <https://www.fastsimulations.com/>. Accessed on 06.30.2017
- [85] OpenPNM. <http://openpnm.org/>. Accessed on 07.12.2017
- [86] Yu X, Ye S (2007) Recent advances in activity and durability enhancement of Pt/C catalytic cathode in PEMFC. Part II: degradation mechanism and durability enhancement of carbon supported platinum catalyst. *J Power Sources*, 172(1):145–154
- [87] Wu J, Yuan X, Martin J, Wang H, Zhang J, Shen J, Wu S, Merida W (2008) A review of PEM fuel cell durability: degradation mechanisms and mitigation strategies. *J Power Sources*, 184(1):104–119
- [88] Schmittinger W, Vahidi A (2008) A review of the main parameters influencing long-term performance and durability of PEM fuel cells. *J Power Sources*, 180(1):1–14

- [89] Antunes R, De Oliveira M, Ett G, Ett V (2011) Carbon materials in composite bipolar plates for polymer electrolyte membrane fuel cells: a review of the main challenges to improve electrical performance. *J Power Sources*, 196(6):2945–2961
- [90] Cunningham B, Huang J, Baird D (2007) Review of materials and processing methods used in the production of bipolar plates for fuel cells. *Int Mater Rev*, 52(1):1–13
- [91] Karimi S, Fraser N, Roberts B, Foulkes F (2012) A review of metallic bipolar plates for proton exchange membrane fuel cells: materials and fabrication methods. *Adv Mater Sci Eng*, 2012
- [92] Tawfik H, Hung Y, Mahajan D (2007) Metal bipolar plates for PEM fuel cell – a review. *J Power Sources*, 163(2):755–767
- [93] Antunes R, Oliveira M, Ett G, Ett V (2010) Corrosion of metal bipolar plates for PEM fuel cells: a review. *Int J Hydrog Energy*, 35(8):3632–3647
- [94] Hermann A, Chaudhuri T, Spagnol P (2005) Bipolar plates for PEM fuel cells: a review. *Int J Hydrog Energy*, 30(12):1297–1302
- [95] Lu Z, Kandlikar S, Rath C, Grimm M, Domigan W, White A, Hardbarger M, Owejan J, Trabold T (2009) Water management studies in PEM fuel cells, part II: ex situ investigation of flow maldistribution, pressure drop and two-phase flow pattern in gas channels. *Int J Hydrog Energy*, 34(8):3445–3456
- [96] Li X, Sabir I (2005) Review of bipolar plates in PEM fuel cells: flow-field designs. *Int J Hydrog Energy*, 30:359–371
- [97] Allen GM, Resnick G (2008) Porous plate for a fuel cell. US Pat Off, US20080160366 A1
- [98] Mathias MF, Roth J, Fleming J, Lehnert W (2010), Handbook of fuel cells. John Wiley & Sons, Ltd
- [99] Cindrella L, Kannan A, Lin J, Saminathan K, Ho Y, Lin C, Wertz J (2009) Gas diffusion layer for proton exchange membrane fuel cells - a review. *J Power Sources*, 194(1):146–160
- [100] Park J, Oh H, Ha T, Lee Y, Min K (2015) A review of the gas diffusion layer in proton exchange membrane fuel cells: durability and degradation. *Appl Energy*, 155:866–880
- [101] Hartnig C, Jörissen L, Kerres J, Lehnert W, Scholta J (2008) Polymer electrolyte membrane fuel cells. Mater for fuel cells 1st ed Boca Raton, Boston, New York, Wash DC: CRC Press & Cambridge: Woodhead Publ Ltd, pages 101–84
- [102] Rashapov R, Unno J, Gostick J (2015) Characterization of PEMFC gas diffusion layer porosity. *J Electrochem Soc*, 162(6):F603–F612
- [103] Zenyuk IV, Parkinson DY, Connolly LG, Weber AZ (2016) Gas-diffusion-layer structural properties under compression via X-ray tomography. *J Power Sources*, 328:364–376
- [104] Gostick JT, Ioannidis MA, Fowler MW, Pritzker MD (2009) On the role of the microporous layer in PEMFC operation. *Electrochem Commun*, 11(3):576–579
- [105] Malevich D, Halliop E, Peppley BA, Pharoah JG, Karan K (2009) Investigation of charge-transfer and mass-transport resistances in PEMFCs with microporous layer using electrochemical impedance spectroscopy. *J Electrochem Soc*, 156(2):B216–B224
- [106] Stampino PG, Cristiani C, Dotelli G, Omati L, Zampori L, Pelosato R, Guilizzoni M (2009) Effect of different substrates, inks composition and rheology on coating deposition of microporous layer (MPL) for PEM-FCs. *Catal Today*, 147:S30–S35
- [107] Weber AZ, Newman J (2005) Effects of microporous layers in polymer electrolyte fuel cells. *J Electrochem Soc*, 152(4):A677–A688
- [108] Lin G, Nguyen TV (2005) Effect of thickness and hydrophobic polymer content of the gas diffusion layer on electrode flooding level in a PEMFC. *J Electrochem Soc*, 152(10):A1942–A1948
- [109] Karan K, Atiyeh H, Phoenix A, Halliop E, Pharoah J, Peppley B (2007) An experimental investigation of water transport in PEMFCs the role of microporous layers. *Electrochem Solid-State Lett*, 10(2):B34–B38

- [110] Owejan JP, Owejan JE, Gu W, Trabold TA, Tighe TW, Mathias MF (2010) Water transport mechanisms in PEMFC gas diffusion layers. *J Electrochem Soc*, 157(10):B1456–B1464
- [111] Thomas A, Maranzana G, Didierjean S, Dillet J, Lottin O (2014) Thermal and water transfer in PEMFCs: Investigating the role of the microporous layer. *Int J Hydrog Energy*, 39(6):2649–2658
- [112] Schulze M, Wagner N, Kaz T, Friedrich K (2007) Combined electrochemical and surface analysis investigation of degradation processes in polymer electrolyte membrane fuel cells. *Electrochimica Acta*, 52(6):2328–2336
- [113] Yang Z, Ball S, Condit D, Gummalla M (2011) Systematic study on the impact of Pt particle size and operating conditions on PEMFC cathode catalyst durability. *J Electrochem Soc*, 158(11):B1439–B1445
- [114] Ahluwalia R, Arisetty S, Wang X, Wang X, Subbaraman R, Ball S, DeCrane S, Myers D (2013) Thermodynamics and kinetics of platinum dissolution from carbon-supported electrocatalysts in aqueous media under potentiostatic and potentiodynamic conditions. *J Electrochem Soc*, 160(4):F447–F455
- [115] Topalov A, Cherevko S, Zeradhanin A, Meier J, Katsounaros I, Mayrhofer K (2014) Towards a comprehensive understanding of platinum dissolution in acidic media. *Chem Sci*, 5(2):631–638
- [116] Dubau L, Castanheira L, Maillard F, Chatenet M, Lottin O, Maranzana G, Dillet J, Lamibrac A, Perrin JC, Moukheiber E et al. (2014) A review of PEM fuel cell durability: materials degradation, local heterogeneities of aging and possible mitigation strategies. *Wiley Interdiscip Rev Energy Environ*, 3(6):540–560
- [117] Arisetty S, Wang X, Ahluwalia R, Mukundan R, Borup R, Davey J, Langlois D, Gambini F, Polevaya O, Blanchet S (2012) Catalyst durability in PEM fuel cells with low platinum loading. *J Electrochem Soc*, 159(5):B455–B462
- [118] Rinaldo S, Stumper J, Eikerling M (2010) Physical theory of platinum nanoparticle dissolution in polymer electrolyte fuel cells. *The J Phys Chem C*, 114(13):5773–5785
- [119] Meyers J, Darling R (2006) Model of carbon corrosion in PEM fuel cells. *J Electrochem Soc*, 153(8):A1432–A1442
- [120] Pandey A, Yang Z, Gummalla M, Atrazhev V, Kuzminykh N, Sultanov V, Burlatsky S (2013) A carbon corrosion model to evaluate the effect of steady state and transient operation of a polymer electrolyte membrane fuel cell. *J Electrochem Soc*, 160(9):F972–F979
- [121] Franco A, Gerard M (2008) Multiscale model of carbon corrosion in a PEFC: coupling with electrocatalysis and impact on performance degradation. *J Electrochem Soc*, 155(4):B367–B384
- [122] Franco A, Guinard M, Barthe B, Lemaire O (2009) Impact of carbon monoxide on PEFC catalyst carbon support degradation under current-cycled operating conditions. *Electrochimica Acta*, 54(22):5267–5279
- [123] Solasi R, Zou Y, Huang X, Reifsnider K, Condit D (2007) On mechanical behavior and in-plane modeling of constrained PEM fuel cell membranes subjected to hydration and temperature cycles. *J Power Sources*, 167(2):366–377
- [124] Khattra N, Karlsson A, Santare M, Walsh P, Busby F (2012) Effect of time-dependent material properties on the mechanical behavior of PFSA membranes subjected to humidity cycling. *J Power Sources*, 214:365–376
- [125] Khattra N, Santare M, Karlsson A, Schmiedel T, Busby F (2015) Effect of water transport on swelling and stresses in PFSA membranes. *Fuel Cells*, 15(1):178–188
- [126] Coulon R, Bessler W, Franco A (2010) Modeling chemical degradation of a polymer electrolyte membrane and its impact on fuel cell performance. *ECS Transactions*, 25(35):259–273
- [127] Yu T, Sha Y, Liu WG, Merinov B, Shirvanian P, Goddard III W (2011) Mechanism for degradation of Nafion in PEM fuel cells from quantum mechanics calculations. *J Am Chem Soc*, 133(49):19857–19863
- [128] Robin C, Gérard M, Quinaud M, d’Arbigny J, Bultel Y (2016) Proton exchange membrane fuel cell model for aging predictions: Simulated equivalent active surface area loss and comparisons with durability tests. *J Power Sources*, 326:417–427

- [129] Park S, Lee JW, Popov BN (2012) A review of gas diffusion layer in PEM fuel cells: materials and designs. *Int J Hydrog Energy*, 37(7):5850–5865
- [130] Kim S, Mench M (2009) Investigation of temperature-driven water transport in polymer electrolyte fuel cell: Thermo-osmosis in membranes. *J Membr Sci*, 328(1):113–120
- [131] Kim S, Ahn BK, Mench M (2008) Physical degradation of membrane electrode assemblies undergoing freeze/thaw cycling: Diffusion media effects. *J Power Sources*, 179(1):140–146
- [132] Swamy T, Kumbur E, Mench M (2010) Characterization of interfacial structure in PEFCs: water storage and contact resistance model. *J Electrochem Soc*, 157(1):B77–B85
- [133] Kalidindi A, Taspinar R, Litster S, Kumbur E (2013) A two-phase model for studying the role of microporous layer and catalyst layer interface on polymer electrolyte fuel cell performance. *Int J Hydrog Energy*, 38(22):9297–9309
- [134] Hizir F, Ural S, Kumbur E, Mench M (2010) Characterization of interfacial morphology in polymer electrolyte fuel cells: Micro-porous layer and catalyst layer surfaces. *J Power Sources*, 195(11):3463–3471
- [135] Zenyuk IV, Taspinar R, Kalidindi AR, Kumbur EC, Litster S (2013) Coupling of deterministic contact mechanics model and two-phase model to study the effect of catalyst layer—microporous layer interface on polymer electrolyte fuel cell performance. *ECS Transactions*, 58(1):1125–1135
- [136] Zielke L, Vierrath S, Moroni R, Mondon A, Zengerle R, Thiele S (2016) Three-dimensional morphology of the interface between micro porous layer and catalyst layer in a polymer electrolyte membrane fuel cell. *RSC Adv*, 6(84):80700–80705
- [137] "Gebel G, Loppinet B (1996) Colloidal structure of ionomer solutions in polar solvents. " *Journal Mol Struct*, 383("1-3"):431–442"
- [138] Welch C, Labouriau A, Hjelm R, Orlor B, Johnston C, Kim Yu S (2012) Nafion in dilute solvent systems: dispersion or solution? *ACS Macro Lett*, 1(12):1403
- [139] Kusoglu A, Weber AZ (2017) New Insights into Perfluorinated Sulfonic-Acid Ionomers. *Chem Rev*, 117(3):987–1104
- [140] Huang X, Zhao Z, Cao L, Chen Y, Zhu E, Lin Z, Li M, Yan A, Zettl A, Wang YM et al. (2015) High-performance transition metal-doped Pt<sub>3</sub>Ni octahedra for oxygen reduction reaction. *Sci*, 348(6240):1230–1234
- [141] Strasser P, Koh S, Anniyev T, Greeley J, More K, Yu C, Liu Z, Kaya S, Nordlund D, Ogasawara H, Toney M, Nilsson A (2010) Lattice-strain control of the activity in dealloyed core-shell fuel cell catalysts. *Nat Chem*, 2(6):454–460
- [142] Sasaki K, Naohara H, Cai Y, Choi YM, Liu P, Vukmirovic MB, Wang JX, Adzic RR (2010) Core-Protected Platinum Monolayer Shell High-Stability Electrocatalysts for Fuel-Cell Cathodes. *Angewandte Chemie Int Ed*, 49(46):8602–8607
- [143] Wu G, More K, Johnston C, Zelenay P (2011) High-performance electrocatalysts for oxygen reduction derived from polyaniline, iron, and cobalt. *Sci*, 332(6028):443–447
- [144] Jaouen F, Proietti E, Lefèvre M, Chenitz R, Dodelet JP, Wu G, Chung HT, Johnston C, Zelenay P (2011) Recent advances in non-precious metal catalysis for oxygen-reduction reaction in polymer electrolyte fuel cells. *Energy Environ Sci*, 4(1):114–130
- [145] Lefèvre M, Proietti E, Jaouen F, Dodelet JP (2009) Iron-based catalysts with improved oxygen reduction activity in polymer electrolyte fuel cells. *science*, 324(5923):71–74
- [146] Chen C, Kang Y, Huo Z, Zhu Z, Huang W, Xin HL, Snyder JD, Li D, Herron JA, Mavrikakis M et al. (2014) Highly crystalline multimetallic nanoframes with three-dimensional electrocatalytic surfaces. *Sci*, 343(6177):1339–1343
- [147] Gu J, Zhang YW, Tao FF (2012) Shape control of bimetallic nanocatalysts through well-designed colloidal chemistry approaches. *Chem Soc Rev*, 41(24):8050–8065

- [148] Banham D, Ye S (2017) Current Status and Future Development of Catalyst Materials and Catalyst Layers for Proton Exchange Membrane Fuel Cells: an Industrial Perspective. *ACS Energy Lett*, 2(3):629–638
- [149] Gasteiger HA, Kocha SS, Sompalli B, Wagner FT (2005) Activity benchmarks and requirements for Pt, Pt-alloy, and non-Pt oxygen reduction catalysts for PEMFCs. *Appl Catal B: Environ*, 56(1):9–35
- [150] Wilson A, Marcinkoski J, Papageorgopoulos D (2016). DOE Hydrogen and fuel cells program record #16020
- [151] Marcinkoski J, Spendelow J, Wilson A, Papageorgopoulos D (2015). DOE Hydrogen and Fuel Cells Program Record #15015
- [152] Kim KH, Lee KY, Kim HJ, Cho E, Lee SY, Lim TH, Yoon SP, Hwang IC, Jang JH (2010) The effects of Nafion® ionomer content in PEMFC MEAs prepared by a catalyst-coated membrane (CCM) spraying method. *Int J Hydrog Energy*, 35(5):2119–2126
- [153] Jeon S, Lee J, Rios GM, Kim HJ, Lee SY, Cho E, Lim TH, Jang JH (2010) Effect of ionomer content and relative humidity on polymer electrolyte membrane fuel cell (PEMFC) performance of membrane-electrode assemblies (MEAs) prepared by decal transfer method. *Int J Hydrog Energy*, 35(18):9678–9686
- [154] Song J, Cha S, Lee W (2001) Optimal composition of polymer electrolyte fuel cell electrodes determined by the AC impedance method. *J Power Sources*, 94(1):78–84
- [155] Du S, Millington B, Pollet BG (2011) The effect of Nafion ionomer loading coated on gas diffusion electrodes with in-situ grown Pt nanowires and their durability in proton exchange membrane fuel cells. *Int J Hydrog Energy*, 36(7):4386–4393
- [156] Shukla S, Stanier D, Saha M, Stumper J, Secanell M (2016) Analysis of inkjet printed PEFC electrodes with varying platinum loading. *J Electrochem Soc*, 163(7):F677–F687
- [157] Secanell M, Carnes B, Suleman A, Djilali N (2007) Numerical optimization of proton exchange membrane fuel cell cathodes. *Electrochimica Acta*, 52(7):2668–2682
- [158] Hao L, Moriyama K, Gu W, Wang CY (2015) Modeling and experimental validation of Pt loading and electrode composition effects in PEM fuel cells. *J Electrochem Soc*, 162(8):F854–F867
- [159] Suzuki A, Sen U, Hattori T, Miura R, Nagumo R, Tsuboi H, Hatakeyama N, Endou A, Takaba H, Williams MC et al. (2011) Ionomer content in the catalyst layer of polymer electrolyte membrane fuel cell (PEMFC): Effects on diffusion and performance. *Int J Hydrog Energy*, 36(3):2221–2229
- [160] Berning T, Djilali N (2003) Three-dimensional computational analysis of transport phenomena in a PEM fuel cell - a parametric study. *J Power Sources*, 124(2):440–452
- [161] Sivertsen B, Djilali N (February 2005) CFD based modelling of proton exchange membrane fuel cells. *J Power Sources*, 141(1):65–78
- [162] Sun W, Peppley B, Karan K (2005) An improved two-dimensional agglomerate cathode model to study the influence of catalyst layer structural parameters. *Electrochimica Acta*, 50(16):3359–3374
- [163] Broka K, Ekdunge P (March 1997) Modelling the PEM fuel cell cathode. *J Appl Electrochem*, 27(3):281–289
- [164] Siegel N, Ellis M, Nelson D, Von Spakovsky M (2003) Single domain PEMFC model based on agglomerate catalyst geometry. *J Power Sources*, 115(1):81–89
- [165] Jaouen F, Lindbergh G, Sundholm G (2002) Investigation of mass-transport limitations in the solid polymer fuel cell cathode - I. Mathematical model. *J Electrochem Soc*, 149(4):A437–A447
- [166] Ihonen J, Jaouen F, Lindbergh G, Lundblad A, Sundholm G (2002) Investigation of mass-transport limitations in the solid polymer fuel cell cathode - II. Experimental. *J Electrochem Soc*, 149(4):A448–A454
- [167] Gode P, Jaouen F, Lindbergh G, Lundblad A, Sundholm G (2003) Influence of the composition on the structure and electrochemical characteristics of the PEMFC cathode. *Electrochimica Acta*, 48:4175–4187
- [168] Secanell M, Songprakorp R, Suleman A, Djilali N (2008) Multi-objective optimization of a polymer electrolyte fuel cell membrane electrode assembly. *Energy Environ Sci*, 1:378–388

- [169] Secanell M, Songprakorp R, Djilali N, Suleman A (2010) Optimization of a proton exchange membrane fuel cell membrane electrode assembly. *Struct Multidiscip Optim*, 40(1-6):563–583
- [170] Dobson P, Lei C, Navessin T, Secanell M (2012) Characterization of the PEM fuel cell catalyst layer microstructure by nonlinear least-squares parameter estimation. *J Electrochem Soc*, 159(5):B514–B523
- [171] Shah A, Kim GS, Sui P, Harvey D (2007) Transient non-isothermal model of a polymer electrolyte fuel cell. *J Power Sources*, 163(2):793–806
- [172] Xing L, Liu X, Alaje T, Kumar R, Mamlouk M, Scott K (2014) A two-phase flow and non-isothermal agglomerate model for a proton exchange membrane (PEM) fuel cell. *Energy*, 73:618–634
- [173] Xing L, Mamlouk M, Kumar R, Scott K (2014) Numerical investigation of the optimal Nafion® ionomer content in cathode catalyst layer: An agglomerate two-phase flow modelling. *Int J Hydrog Energy*, 39(17):9087–9104
- [174] Wang Q, Eikerling M, Song D, Liu Z (2004) Structure and performance of different types of agglomerates in cathode catalyst layers in PEM fuel cells. *J Electroanal Chem*, 573:61–69
- [175] Wardlaw P (2014), Modelling of PEMFC catalyst layer mass transport and electro-chemical reactions using multi-scale simulations. Master's thesis, University of Alberta
- [176] Bird RB, Stewart WE, Lightfoot E (2002), *Transport Phenomena*. J. Wiley and Sons, 2nd edition
- [177] Ma S, Solterbeck CH, Odgaard M, Skou E (2009) Microscopy studies on proton exchange membrane fuel cell electrodes with different ionomer contents. *Appl Phys A: Mater Sci & Process*, 96(3):581–589
- [178] Xu F, Zhang H, Ilavsky J, Stanciu L, Ho D, Justice MJ, Petrache HI, Xie J (2010) Investigation of a catalyst ink dispersion using both ultra-small-angle X-ray scattering and cryogenic TEM. *Langmuir*, 26(24):19199–19208
- [179] Banham D, Feng F, Fürstenthaupt T, Pei K, Ye S, Birss V (2011) Effect of Pt-loaded carbon support nanostructure on oxygen reduction catalysis. *J Power Sources*, 196(13):5438–5445
- [180] Epting W, Litster S (2012) Effects of an agglomerate size distribution on the PEFC agglomerate model. *Int J Hydrog Energy*, 37(10):8505–8511
- [181] More K, Borup R, Reeves K (2006) Identifying contributing degradation phenomena in PEM fuel cell membrane electrode assemblies via electron microscopy. *ECS Transactions*, 3(1):717–733
- [182] Kudo K, Suzuki T, Morimoto Y (2010) Analysis of oxygen dissolution rate from gas phase into Nafion surface and development of an agglomerate model. *ECS Transactions*, 33(1):1495–1502
- [183] Suzuki T, Kudo K, Morimoto Y (2013) Model for investigation of oxygen transport limitation in a polymer electrolyte fuel cell. *J Power Sources*, 222:379–389
- [184] Moore M, Wardlaw P, Dobson P, Boisvert J, Putz A, Spiteri R, Secanell M (2014) Understanding the effect of kinetic and mass transport processes in cathode agglomerates. *J Electrochem Soc*, 161(8):E3125–E3137
- [185] Banham D, Feng F, Fürstenthaupt T, Ye S, Birss V (2012) First time investigation of Pt nanocatalysts deposited inside carbon mesopores of controlled length and diameter. *J Mater Chem*, 22(15):7164–7171
- [186] Shao Y, Yin G, Gao Y (2007) Understanding and approaches for the durability issues of Pt-based catalysts for PEM fuel cell. *J Power Sources*, 171(2):558–566
- [187] Katsounaros I, Cherevko S, Zeradjanin A, Mayrhofer K (2014) Oxygen electrochemistry as a cornerstone for sustainable energy conversion. *Angewandte Chemie - Int Ed*, 53(1):102–121
- [188] Roen L, Paik C, Jarvi T (2004) Electrocatalytic corrosion of carbon support in PEMFC cathodes. *Electrochem Solid-State Lett*, 7(1):A19–A22
- [189] Liu Z, Brady B, Carter R, Litteer B, Budinski M, Hyun J, Muller D (2008) Characterization of carbon corrosion-induced structural damage of PEM fuel cell cathode electrodes caused by local fuel starvation. *J Electrochem Soc*, 155(10):B979–B984
- [190] Young A, Stumper J, Gyenge E (2009) Characterizing the structural degradation in a PEMFC cathode catalyst layer: carbon corrosion. *J Electrochem Soc*, 156(8):B913–B922

- [191] Darling RM, Meyers JP (2003) Kinetic Model of Platinum Dissolution in PEMFCs . *J Electrochem Soc*, 150(11):A1523–A1527
- [192] Franco AA, Tembely M (2007) Transient multiscale modeling of aging mechanisms in a PEFC cathode. *J Electrochem Soc*, 154(7):B712–B723
- [193] Rinaldo S, Lee W, Stumper J, Eikerling M (2011) Model- and theory-based evaluation of Pt dissolution for supported Pt nanoparticle distributions under potential cycling. *Electrochem Solid-State Lett*, 14(5):B47–B49
- [194] Holby EF, Morgan D (2012) Application of Pt nanoparticle dissolution and oxidation modeling to understanding degradation in PEM fuel cells . *J Electrochem Soc*, 159(5):B578–B591
- [195] Rinaldo S, Lee W, Stumper J, Eikerling M (2014) Mechanistic principles of platinum oxide formation and reduction. *Electrocatalysis*, 5(3):262–272
- [196] Redmond E, Setzler B, Alamgir F, Fuller T (2014) Elucidating the oxide growth mechanism on platinum at the cathode in PEM fuel cells. *Phys Chem Chem Phys*, 16(11):5301–5311
- [197] Fuller T, Gray G (2006) Carbon corrosion induced by partial hydrogen coverage. *ECS Transactions*, 1(8):345–353
- [198] Newman J, Thomas-Alyea KE (2012), *Electrochemical systems*. John Wiley & Sons
- [199] Bard AJ, Faulkner LR (2001), *Electrochemical methods: fundamentals and applications*. John Wiley & Sons, Inc., second edition
- [200] Verbrugge M, Hill R (1990) Ion and solvent transport in ion-exchange membranes I. A macrohomogeneous mathematical model. *J Electrochem Soc*, 137(3):886–893
- [201] Bernardi D, Verbrugge M (August 1991) Mathematical model of a gas diffusion electrode bonded to a polymer electrolyte. *AIChE J*, 37(8):1151–1163
- [202] Cwirko E, Carbonell R (1992) Interpretation of transport coefficients in Nafion using a parallel pore model. *J Membr Sci*, 67(2-3):227–247
- [203] Zhang Z, Jia L, Wang X, Ba L (2011) Effects of inlet humidification on PEM fuel cell dynamic behaviors. *Int J Energy Res*, 35(5):376–388
- [204] Li HY, Weng WC, Yan WM, Wang XD (2011) Transient characteristics of proton exchange membrane fuel cells with different flow field designs. *J Power Sources*, 196(1):235–245
- [205] Meng H, Ruan B (2011) Numerical studies of cold-start phenomena in PEM fuel cells: a review. *Int J Energy Res*, 35(1):2–14
- [206] Yang X, Yin Y, Jia B, Du Q (2013), Analysis of voltage losses in high temperature proton exchange membrane fuel cells with properties of membrane materials and fluent software. In *Advanced Materials Research*, volume 625, pages 235–238. Trans Tech Publ
- [207] Genevey D, von Spakovsky M, Ellis M, Nelson D, Olsommer B, Topin F, Siegel N (2002), Transient model of heat, mass, and charge transfer as well as electrochemistry in the cathode catalyst layer of a PEMFC. In *ASME 2002 International Mechanical Engineering Congress and Exposition*, pages 393–406. American Society of Mechanical Engineers
- [208] Olapade P, Meyers J, Mukundan R, Davey J, Borup R (2011) Modeling the dynamic behavior of proton-exchange membrane fuel cells. *J Electrochem Soc*, 158(5):B536–B549
- [209] Zenyuk IV, Das PK, Weber AZ (2016) Understanding impacts of catalyst-layer thickness on fuel-cell performance via mathematical modeling. *J Electrochem Soc*, 163(7):F691–F703
- [210] Eikerling M, Kharkats YI, Kornyshev AA, Volfkovich YM (1998) Phenomenological theory of electro-osmotic effect and water management in polymer electrolyte proton-conducting membranes. *J Electrochem Soc*, 145(8):2684–2699
- [211] Fimrite J, Struchtrup H, Djilali N (2005) Transport phenomena in polymer electrolyte membranes. Part I: Modeling framework. *J Electrochem Soc*, 152(9):A1804–A1814

- [212] Weber AZ, Newman J (2004) Transport in Polymer-Electrolyte Membranes: II. Mathematical Model. *J Electrochem Soc*, 151(2):A311–A325
- [213] Fimrite J, Struchtrup H, Djilali N (2005) Transport phenomena in polymer electrolyte membranes. Part II: Binary friction membrane model. *J Electrochem Soc*, 152(9):A1815–A1823
- [214] Kerkhof P, Geboers M (2005) Toward a unified theory of isotropic molecular transport phenomena. *AIChE J*, 51(1):79–121
- [215] Kerkhof P, Geboers M (2005) Analysis and extension of the theory of multicomponent fluid diffusion. *Chem Eng Sci*, 60(12):3129–3167
- [216] Taylor R, Krishna R (1993), *Multicomponent mass transfer*, volume 2. John Wiley & Sons
- [217] White F (1991), *Viscous fluid flow*. McGraw-Hill, 2nd edition
- [218] Donea J, Huerta A (2003), *Finite element methods for flow problems*. John Wiley & Sons, 1st edition
- [219] Meng H, Wang C (2004) Electron transport in PEMFCs. *J Electrochem Soc*, 151(3):A358–A367
- [220] Um S, Wang CY, Chen K (2000) Computational fluid dynamics modeling of proton exchange membrane fuel cells. *J Electrochem Soc*, 147(12):4485–4493
- [221] Shimpalee S, Dutta S, Lee W, Zee JV (1999) Effect of humidity on PEM fuel cell performance: Part II-Numerical simulation. *ASME-PUBLICATIONS-HTD*, 364:367–374
- [222] Dutta S, Shimpalee S, Zee JV (2000) Three-dimensional numerical simulation of straight channel PEM fuel cells. *J Appl Electrochem*, 30(2):135–146
- [223] Zamel N, Li X (2008) A parametric study of multi-phase and multi-species transport in the cathode of PEM fuel cells. *Int J Energy Res*, 32(8):698–721
- [224] Pant L, Mitra S, Secanell M (2013) A generalized mathematical model to study gas transport in PEMFC porous media. *Int J Heat Mass Transf*, 58(1-2):70–79
- [225] Balen C (2016), *A multi-component mass transport model for polymer electrolyte fuel cells*, PhD thesis, University of Alberta
- [226] Golpaygan A, Ashgriz N (2005) Effects of oxidant fluid properties on the mobility of water droplets in the channels of PEM fuel cell. *Int J Energy Res*, 29(12):1027–1040
- [227] Quan P, Zhou B, Sobiesiak A, Liu Z (2005) Water behavior in serpentine micro-channel for proton exchange membrane fuel cell cathode. *J Power Sources*, 152:131–145
- [228] Jiao K, Zhou B, Quan P (2006) Liquid water transport in parallel serpentine channels with manifolds on cathode side of a PEM fuel cell stack. *J Power Sources*, 154(1):124–137
- [229] Cai Y, Hu J, Ma H, Yi B, Zhang H (2006) Effects of hydrophilic/hydrophobic properties on the water behavior in the micro-channels of a proton exchange membrane fuel cell. *J Power Sources*, 161(2):843–848
- [230] Choi J, Son G (2008) Numerical study of droplet motion in a microchannel with different contact angles. *J Mech Sci Technol*, 22(12):2590–2599
- [231] Bazylak A, Sinton D, Djilali N (2008) Dynamic water transport and droplet emergence in PEMFC gas diffusion layers. *J Power Sources*, 176(1):240–246
- [232] Akhtar N, Kerkhof PJAM (2011) Dynamic behavior of liquid water transport in a tapered channel of a proton exchange membrane fuel cell cathode. *Int J Hydrog Energy*, 36(4):3076–3086
- [233] Jarauta A, Ryzhakov PB, Secanell M, Waghmare PR, Pons-Prats J (2016) Numerical study of droplet dynamics in a polymer electrolyte fuel cell gas channel using an embedded Eulerian-Lagrangian approach. *J Power Sources*, 323:201–212
- [234] Ryzhakov PB, Jarauta A, Secanell M, Pons-Prats J (2017) On the application of the PFEM to droplet dynamics modeling in fuel cells. *Comput Part Mech*, 4(3):285–295

- [235] Hyman J, Knapp R, Scovel J (1992) High order finite volume approximations of differential operators on nonuniform grids. *Phys D: Nonlinear Phenom*, 60(1):112–138
- [236] ANSYS Fluent. <http://www.ansys.com/Products/Fluids/ANSYS-Fluent>. Accessed on 06.30.2017
- [237] STAR-CCM+. <https://mdx.plm.automation.siemens.com/star-ccm-plus>. Accessed on 06.30.2017
- [238] OpenFOAM. <http://www.openfoam.com/>. Accessed on 06.30.2017
- [239] Zienkiewicz O, Taylor R, Taylor R (1977), *The finite element method*, volume 3. McGraw-hill London
- [240] COMSOL Multiphysics. <https://www.comsol.com/>. Accessed on 06.30.2017
- [241] Dadvand P, Rossi R, Oñate E (2010) An object-oriented environment for developing finite element codes for multi-disciplinary applications. *Arch Comput Methods Eng*, 17/3:253–297
- [242] Bangerth W, Hartmann R, Kanschat G (2007) deal.II – a general purpose object oriented finite element library. *ACM Trans Math Softw*, 33(4):24/1–24/27
- [243] Chen K, Hickner M, Noble D (2005) Simplified models for predicting the onset of liquid water droplet instability at the gas diffusion layer/gas flow channel interface. *Int J Energy Res*, 29(12):1113–1132
- [244] Kumbur E, Sharp K, Mench M (2006) Liquid droplet behavior and instability in a polymer electrolyte fuel cell flow channel. *J Power Sources*, 161:333–345
- [245] Jarauta A, Secanell M, Pons-Prats J, Ryzhakov PB, Idelsohn SR, Oñate E (2015) A semi-analytical model for droplet dynamics on the GDL surface of a PEFC electrode. *Int J Hydrog Energy*, 40:5375–5383
- [246] Hirt C, Nichols B (1981) Volume of fluid (VOF) method for the dynamics of free boundaries. *J Comput Phys*, 39:201–225
- [247] Youngs DL (1982) Time-dependent multi-material flow with large fluid distortion. *Numer Methods for Fluid Dyn*, 24:273–285
- [248] Gueyffier D, Li J, Nadim A, Scardovelli R, Zaleski S (1999) Volume-of-Fluid interface tracking with smoothed surface stress methods for three dimensional flows. *J Comput Phys*, 152:423–456
- [249] Ferreira RB, Falcão DS, Oliveira VB, Pinto AMFR (2015) Numerical simulations of two-phase flow in proton exchange membrane fuel cells using the volume of fluid method - a review. *J Power Sources*, 277:329–342
- [250] Brackbill J, Kothe D, Zemach C (1992) A continuum method for modeling surface tension. *J Comput Phys*, 100:335–354
- [251] Lafaurie B, Nardone C, Scardovelli R, Zaleski S, Zanetti G (1994) Modelling merging and fragmentation in multiphase flows with SURFER. *J Comput Phys*, 113(1):134–147
- [252] Golpaygan A, Ashgriz N (2008) Multiphase flow model to study channel flow dynamics of PEM fuel cells: deformation and detachment of water droplets. *Int J Comput Fluid Dyn*, 22(1-2):85–95
- [253] Shirani E, Masoomi S (2008) Deformation of a droplet in a channel flow. *J Fuel Cell Sci Technol*, 5(4):041008
- [254] Jiao K, Zhou B, Quan P (2006) Liquid water transport in straight micro-parallel-channels with manifolds for PEM fuel cell cathode. *J Power Sources*, 157(1):226–243
- [255] Zhan Z, Xiao J, Pan M, Yuan R (2006) Characteristics of droplet and film water motion in the flow channels of polymer electrolyte membrane fuel cells. *J Power Sources*, 160(1):1–9
- [256] Quan P, Lai M (2007) Numerical study of water management in the air flow channel of a PEM fuel cell cathode. *J Power Sources*, 164:222–237
- [257] Quan P, Lai M (2010) Numerical simulation of two-phase water behavior in the cathode of an interdigitated proton exchange membrane fuel cell. *J Fuel Cell Sci Technol*, 7(1)
- [258] Theodorakakos A, Ous T, Gavaises M, Nouri J, Nikolopoulos N, Yanagihara H (2006) Dynamics of water droplets detached from porous surfaces of relevance to PEM fuel cells. *J Colloid Interface Sci*, 300:673–687

- [259] Le A, Zhou B (2008) A general model of proton exchange membrane fuel cell. *J Power Sources*, 182(1):197–222
- [260] Osher S, Sethian J (1988) Fronts propagating with curvature dependent speed: algorithms based on Hamilton-Jacobi formulations. *J Comput Phys*, 79:12–49
- [261] Osher SJ, Fedkiw RP (2006), *Level set methods and dynamic implicit surfaces*. Springer
- [262] Rossi R, Larese A, Dadvand P, Oñate E (2013) An efficient edge-based level set finite element method for free surface flow problems. *Int J for Numer Methods Fluids*, 71(6):687–716
- [263] Wörner M (2012) Numerical modeling of multiphase flows in microfluidics and micro process engineering: a review of methods and applications. *Microfluid Nanofluid*, 12:841–886
- [264] Cruchaga M, Celentano D, Tezduyar T (2001) A moving Lagrangian interface technique for flow computations over fixed meshes. *Comput Methods Appl Mech Eng*, 191(6):525–543
- [265] Barton PT, Obadia B, Drikakis D (2011) A conservative level-set method for compressible solid/fluid problems on fixed grids. *J Comput Phys*, 230:7867–7890
- [266] Spelt PDM (2005) A level-set approach for simulations of flows with multiple moving contact lines with hysteresis. *J Comput Phys*, 207(2):389–404
- [267] Zhang YL, Zou QP, Greaves D (2010) Numerical simulation of free-surface flow using the level-set method with global mass correction. *Int J Numer Methods Fluids*, 63(6):366–396
- [268] Ausas RF, Dari EA, Buscaglia GC (2011) A geometric mass-preserving redistancing scheme for the level set function. *Int J Numer Methods Fluids*, 65(8):989–1010
- [269] Ryzhakov PB, Jarauta A (2015) An embedded approach for immiscible multi-fluid problems. *Int J Numer Methods Fluids*, 81:357–376
- [270] Marti J, Ryzhakov P, Idelsohn S, Oñate E (2012) Combined Eulerian-PFEM approach for analysis of polymers in fire situations. *Int J for Numer Methods Eng*, 92:782–801
- [271] Minor G (2007), *Experimental study of water droplet flows in a model PEM fuel cell gas microchannel*. Master's thesis, University of Victoria
- [272] Nield D, Bejan A (2006), *Convection in porous media*, volume 3. Springer
- [273] Jackson R (1977), *Transport in porous catalysts*. Number 4 in *Chemical engineering monographs*. Elsevier Scientific Pub. Co.
- [274] Kerkhof P (1996) A modified Maxwell-Stefan model for transport through inert membranes: the binary friction model. *The Chem Eng J Biochem Eng J*, 64(3):319–343
- [275] Lightfoot E (1973), *Transport phenomena and living systems: biomedical aspects of momentum and mass transport*. Wiley
- [276] Salcedo-Díaz R, Ruiz-Femenia R, Kerkhof P, Peters E (2008) Velocity profiles and circulation in Stefan-diffusion. *Chem Eng Sci*, 63(19):4685–4693
- [277] Datta R, Vilekar SA (2010) The continuum mechanical theory of multicomponent diffusion in fluid mixtures. *Chem Eng Sci*, 65(22):5976–5989
- [278] Vural Y, Ma L, Ingham DB, Pourkashanian M (2010) Comparison of the multicomponent mass transfer models for the prediction of the concentration overpotential for solid oxide fuel cell anodes. *J Power Sources*, 195(15):4893–4904
- [279] Bothe D, Dreyer W (2015) Continuum thermodynamics of chemically reacting fluid mixtures. *Acta Mech*, 226(6):1757–1805
- [280] Akhtar N, Kerkhof P (2012) Predicting liquid water saturation through differently structured cathode gas diffusion media of a proton exchange Membrane Fuel Cell. *J Fuel Cell Sci Technol*, 9(2):021010

- [281] Le A, Zhou B (2009) A generalized numerical model for liquid water in a proton exchange membrane fuel cell with interdigitated design. *J Power Sources*, 193(2):665–683
- [282] Le AD, Zhou B (2009) Fundamental understanding of liquid water effects on the performance of a PEMFC with serpentine-parallel channels. *Electrochimica Acta*, 54(8):2137–2154
- [283] Le A, Zhou B (2010) A numerical investigation on multi-phase transport phenomena in a proton exchange membrane fuel cell stack. *J Power Sources*, 195(16):5278–5291
- [284] Tomadakis M, Robertson T (2005) Viscous permeability of random fiber structures: comparison of electrical and diffusional estimates with experimental and analytical results. *J Compos Mater*, 39(2):163–188
- [285] Williams MV, Begg E, Bonville L, H.R.Kunz, Fenton J (2004) Characterization of gas diffusion layers for PEMFC. *J Electrochem Soc*, 151(8):A1173–A1180
- [286] Gostick J, Fowler M, Pritzker M, Ioannidis M, Behra L (2006) In-plane and through-plane gas permeability of carbon fiber electrode backing layers. *J Power Sources*, 162(1):228–238
- [287] Feser J, Prasad A, Advani S (2006) Experimental characterization of in-plane permeability of gas diffusion layers. *J Power Sources*, 162(2):1226–1231
- [288] Gurau V, Bluemle MJ, De Castro ES, Tsou YM, Zawodzinski Jr TA, Mann Jr JA (2007) Characterization of transport properties in gas diffusion layers for proton exchange membrane fuel cells: 2. Absolute permeability. *J Power Sources*, 165(2):793–802
- [289] Ismail M, Damjanovic T, D.Ingham (2010) Effect of polytetrafluoroethylene-treatment and microporous layer-coating on the in-plane permeability of gas diffusion layers used in proton exchange membrane fuel cells. *J Power Sources*, 195:6619–6628
- [290] Tamayol A, Bahrami M (2011) In-plane gas permeability of proton exchange membrane fuel cell gas diffusion layers. *J Power Sources*, 196(7):3559–3564
- [291] Pant LM, Mitra SK, Secanell M (2012) Absolute permeability and Knudsen diffusivity measurements in PEMFC gas diffusion layers and micro porous layers. *J Power Sources*, 206:153–160
- [292] Carrigy NB, Pant LM, Mitra S, Secanell M (2013) Knudsen diffusivity and permeability of PEMFC microporous coated gas diffusion layers for different polytetrafluoroethylene loadings. *J Electrochem Soc*, 160(2):F81–F89
- [293] Tamayol A, McGregor F, Bahrami M (2012) Single phase through-plane permeability of carbon paper gas diffusion layers. *J Power Sources*, 204:94–99
- [294] Mangal P, Dumontier M, Carrigy N, Secanell M (2014) Measurements of permeability and effective in-plane gas diffusivity of gas diffusion media under compression. *ECS Transactions*, 64(3):487–499
- [295] Inoue G, Kawase M (2016) Effect of porous structure of catalyst layer on effective oxygen diffusion coefficient in polymer electrolyte fuel cell. *J Power Sources*, 327:1–10
- [296] Tomadakis M, Sotirchos S (1993) Ordinary and transition regime diffusion in random fiber structures. *AIChE J*, 39(3):397–412
- [297] Tjaden B, Cooper S, Brett D, Kramer D, Shearing P (2016) On the origin and application of the Bruggeman correlation for analysing transport phenomena in electrochemical systems. *Curr Opin Chem Eng*, 12:44–51
- [298] Flückiger R, Freunberger SA, Kramer D, Wokaun A, Scherer GG, Büchi FN (2008) Anisotropic, effective diffusivity of porous gas diffusion layer materials for PEFC. *Electrochimica Acta* 54, 54:551–559
- [299] LaManna JM, Kandlikar SG (2011) Determination of effective water vapor diffusion coefficient in pemfc gas diffusion layers. *Int J Hydrog Energy*, 36(8):5021–5029
- [300] Hwang G, Weber A (2012) Effective-diffusivity measurement of partially-saturated fuel-cell gas-diffusion layers. *J Electrochem Soc*, 159(11):F683–F692
- [301] Rashapov R, Gostick J (2016) In-plane effective diffusivity in PEMFC gas diffusion layers. *Transp Porous Media*, 115(3):411–433

- [302] Zamel N, Becker J, Wiegmann A (2012) Estimating the thermal conductivity and diffusion coefficient of the microporous layer of polymer electrolyte membrane fuel cells. *J Power Sources*, 207:70–80
- [303] Djilali N, Lu D (2002) Influence of heat transfer on gas and water transport in fuel cells. *Int J Therm Sci*, 41(1):29–40
- [304] Zhou J, Putz A, Secanell M (2017) A mixed wettability pore size distribution based mathematical model for analyzing two-phase flow in porous electrodes I. Mathematical model. *J Electrochem Soc*, 164(6):F530–F539
- [305] Schlögl R (1966) Membrane permeation in systems far from equilibrium. *Berichte der Bunsengesellschaft für physikalische Chemie*, 70(4):400–414
- [306] Singh D, Lu D, Djilali N (1999) A two-dimensional analysis of mass transport in proton exchange membrane fuel cells. *Int J Eng Sci*, 37(4):431–452
- [307] Sundmacher K, Schultz T, Zhou S, Scott K, Ginkel M, Gilles E (2001) Dynamics of the direct methanol fuel cell (DMFC): experiments and model-based analysis. *Chem Eng Sci*, 56(2):333–341
- [308] Bhaiya M (2014), An open-source two-phase non-isothermal mathematical model of a polymer electrolyte membrane fuel cell. Master’s thesis, University of Alberta
- [309] Bhaiya M, Putz A, Secanell M (2014) Analysis of non-isothermal effects on polymer electrolyte fuel cell electrode assemblies. *Electrochimica Acta*, 147:294–304
- [310] Zawodzinski TA, Derouin C, Radzinski S, Sherman RJ, Smith VT, Springer TE, Gottesfeld S (1993) Water uptake by and transport through Nafion® 117 membranes. *J Electrochem Soc*, 140(4):1041–1047
- [311] Ye X, Wang CY (2007) Measurement of Water Transport Properties Through Membrane-Electrode Assemblies I. Membranes. *J Electrochem Soc*, 154(7):B676–B682
- [312] Xu F, Leclerc S, Stemmelen D, Perrin JC, Retournard A, Canet D (2017) Study of electro-osmotic drag coefficients in Nafion membrane in acid, sodium and potassium forms by electrophoresis NMR. *J Membr Sci*, 536:116–122
- [313] Ge S, Yi B, Ming P (2006) Experimental determination of electro-osmotic drag coefficient in Nafion membrane for fuel cells. *J Electrochem Soc*, 153(8):A1443–A1450
- [314] Braff W, Mittelsteadt CK (2008) Electroosmotic drag coefficient of proton exchange membranes as a function of relative humidity. *ECS Transactions*, 16(2):309–316
- [315] Motupally S, Becker A, Weidner J (2000) Diffusion of water in Nafion 115 membranes. *J Electrochem Soc*, 147(9):3171–3177
- [316] Fuller TF (1992), Solid-polymer-electrolyte fuel cells, PhD thesis
- [317] Zhou J, Stanier D, Putz A, Secanell M (2017) A mixed wettability pore size distribution based mathematical model for analyzing two-phase flow in porous electrodes II. Model validation and analysis of micro-structural parameters. *J Electrochem Soc*, 164(6):F540–F556
- [318] Tasaka M, Hirai T, Kiyono R, Aki Y (1992) Solvent transport across cation-exchange membranes under a temperature difference and under an osmotic pressure difference. *J Membr Sci*, 71(1-2):151–159
- [319] Villaluenga J, Seoane B, Barragán V, Ruiz-Bauzá C (2006) Thermo-osmosis of mixtures of water and methanol through a Nafion membrane. *J Membr Sci*, 274(1):116–122
- [320] Hinatsu JT, Mizuhata M, Takenaka H (1994) Water uptake of perfluorosulfonic acid membranes from liquid water and water vapor. *J Electrochem Soc*, 141(6):1493–1498
- [321] Liu Y, Murphy M, Baker D, Gu W, Ji C, Jorne J, Gasteiger H (2009) Proton conduction and oxygen reduction kinetics in PEM fuel cell cathodes: effects of ionomer-to-carbon ratio and relative humidity. *J Electrochem Soc*, 156(8):B970–B980
- [322] Berg P, Promislow K, Pierre J, Stumper J, Wetton B (2004) Water management in PEM fuel cells. *J Electrochem Soc*, 151(3):A341–A353

- [323] Weber AZ (2010) Improved modeling and understanding of diffusion-media wettability on polymer-electrolyte-fuel-cell performance. *Journal Power Sources*, 195(16):5292–5304
- [324] Z.H. Wang CWKC (2001) Two-phase flow and transport in the air cathode of proton exchange membrane fuel cells. *J Power Sources*, 94:40–50
- [325] Meng H, Wang CY (2005) Model of two-phase flow and flooding dynamics in polymer electrolyte fuel cells. *J Electrochem Soc*, 152(9):A1733–A1741
- [326] Siegel N, Ellis M, Nelson D, Von Spakovsky M (2004) A two-dimensional computational model of a PEMFC with liquid water transport. *J Power Sources*, 128(2):173–184
- [327] Nam JH, Kaviany M (2003) Effective diffusivity and water-saturation distribution in single-and two-layer PEMFC diffusion medium. *Int J Heat Mass Transf*, 46(24):4595–4611
- [328] Qin C, Rensink D, Fell S, Hassanizadeh SM (2012) Two-phase flow modeling for the cathode side of a polymer electrolyte fuel cell. *J Power Sources*, 197:136–144
- [329] Eikerling M (2006) Water management in cathode catalyst layers of PEM fuel cells a structure-based model. *J Electrochem Soc*, 153(3):E58–E70
- [330] Weber AZ, Darling RM, Newman J (2004) Modeling two-phase behavior in PEFCs. *J Electrochem Soc*, 151(10):A1715–A1727
- [331] Mulone V, Karan K (2013) Analysis of capillary flow driven model for water transport in PEFC cathode catalyst layer: consideration of mixed wettability and pore size distribution. *Int J Hydrog Energy*, 38(1):558–569
- [332] Natarajan D, Van Nguyen T (2001) A two-dimensional, two-phase, multicomponent, transient model for the cathode of a proton exchange membrane fuel cell using conventional gas distributors. *J Electrochem Soc*, 148(12):A1324–A1335
- [333] Wang Z, Wang C, Chen K (2001) Two-phase flow and transport in the air cathode of proton exchange membrane fuel cells. *J Power Sources*, 94(1):40–50
- [334] Soboleva T, Zhao X, Malek K, Xie Z, Navessin T, Holdcroft S (2010) On the micro-, meso-, and macroporous structures of polymer electrolyte membrane fuel cell catalyst layers. *ACS Appl Mater & Interfaces*, 2(2):375–384
- [335] Thiele S, Zengerle R, Ziegler C (2011) Nano-morphology of a polymer electrolyte fuel cell catalyst layer—Imaging, reconstruction and analysis. *Nano Res*, 4(9):849–860
- [336] Gostick J, Ioannidis MA, Pritzker MD, Fowler MW (2010) Impact of liquid water on reactant mass transfer in PEM fuel cell electrodes. *J Electrochem Soc*, 157(4):B563–B571
- [337] Rebai M, Prat M (2009) Scale effect and two-phase flow in a thin hydrophobic porous layer. Application to water transport in gas diffusion layers of proton exchange membrane fuel cells. *J Power Sources*, 192(2):534–543
- [338] Zenyuk IV, Medici E, Allen J, Weber AZ (2015) Coupling continuum and pore-network models for polymer-electrolyte fuel cells. *Int J Hydrog Energy*, 40(46):16831–16845
- [339] Song D, Wang Q, Liu Z, Eikerling M, Xie Z, Navessin T, Holdcroft S (2005) A method for optimizing distributions of Nafion and Pt in cathode catalyst layers of PEM fuel cells. *Electrochimica Acta*, 50(16):3347–3358
- [340] Baschuk J, Li X (2000) Modelling of polymer electrolyte membrane fuel cells with variable degrees of water flooding. *J power sources*, 86(1):181–196
- [341] Culligan P, Barry D (1996), Scaling immiscible flow in porous media. Technical report, Research Report ED 1207 PC, Centre for Water Research, University of Western Australia, Perth, Australia
- [342] Jiao K, Li X (2011) Water transport in polymer electrolyte membrane fuel cells. *Prog Energy Combust Sci*, 37(3):221–291
- [343] Litster S, Djilali N (2006), Transport phenomena in fuel cells, chapter 5. WIT Press, Ashurst, U.K., 1st edition
- [344] Leverett M, Lewis W (1941) Steady flow of gas-oil-water mixtures through unconsolidated sands. *Transactions AIME*, 142(01):107–116

- [345] Siegel N, Ellis M, Nelson D, Von Spakovsky M (2004) A two-dimensional computational model of a PEMFC with liquid water transport. *J Power Sources*, 128(2):173–184
- [346] Natarajan D, Van Nguyen T (2003) Three-dimensional effects of liquid water flooding in the cathode of a PEM fuel cell. *J Power Sources*, 115(1):66–80
- [347] You L, Liu H (2002) A two-phase flow and transport model for the cathode of PEM fuel cells. *Int J Heat Mass Transf*, 45(11):2277–2287
- [348] Hu M, Gu A, Wang M, Zhu X, Yu L (2004) Three dimensional, two phase flow mathematical model for PEM fuel cell: Part I. Model development. *Energy Convers Manag*, 45(11):1861–1882
- [349] Meng H (2007) A two-phase non-isothermal mixed-domain PEM fuel cell model and its application to two-dimensional simulations. *J Power Sources*, 168(1):218–228
- [350] Lin G, Van Nguyen T (2006) A two-dimensional two-phase model of a PEM fuel cell. *J Electrochem Soc*, 153(2):A372–A382
- [351] Mateo-Villanueva P (2013), A mixed wettability pore size distribution model for the analysis of water transport in PEMFC materials. Master’s thesis, University of Alberta
- [352] Gostick JT, Ioannidis MA, Fowler MW, Pritzker MD (2009) Wettability and capillary behavior of fibrous gas diffusion media for polymer electrolyte membrane fuel cells. *J Power Sources*, 194(1):433–444
- [353] Zhang FY, Spornjak D, Prasad AK, Advani SG (2007) In situ characterization of the catalyst layer in a polymer electrolyte membrane fuel cell. *J Electrochem Soc*, 154(11):B1152–B1157
- [354] Ihonen J, Mikkola M, Lindbergh G (2004) Flooding of gas diffusion backing in PEFCs: Physical and electrochemical characterization. *J Electrochem Soc*, 151(8):A1152–A1161
- [355] Prasanna M, Ha H, Cho E, Hong SA, Oh IH (2004) Influence of cathode gas diffusion media on the performance of the pemfcs. *J Power Sources*, 131(1):147–154
- [356] Dohle H, Jung R, Kimiaie N, Mergel J, Müller M (2003) Interaction between the diffusion layer and the flow field of polymer electrolyte fuel cellsexperiments and simulation studies. *J Power Sources*, 124(2):371–384
- [357] Nguyen T, Lin G, Ohn H, Hussey D, Jacobson D, Arif M (2006) Measurements of two-phase flow properties of the porous media used in pem fuel cells. *ECS transactions*, 3(1):415–423
- [358] Koido T, Furusawa T, Moriyama K, Takato K (2006) Two-phase transport properties and transport simulation of the gas diffusion layer of a pefc. *ECS Transactions*, 3(1):425–434
- [359] Hussaini I, Wang C (2010) Measurement of relative permeability of fuel cell diffusion media. *J Power Sources*, 195(12):3830–3840
- [360] Sole JD (2008), Investigation of water transport parameters and processes in the gas diffusion layer of PEM fuel cells, PhD thesis
- [361] Gostick JT, Ioannidis MA, Fowler MW, Pritzker MD (2007) Pore network modeling of fibrous gas diffusion layers for polymer electrolyte membrane fuel cells. *J Power Sources*, 173(1):277–290
- [362] He G, Ming P, Zhao Z, Abudula A, Xiao Y (2007) A two-fluid model for two-phase flow in PEMFCs. *J Power Sources*, 163(2):864–873
- [363] Koido T, Furusawa T, Moriyama K (2008) An approach to modeling two-phase transport in the gas diffusion layer of a proton exchange membrane fuel cell. *J Power Sources*, 175(1):127–136
- [364] Pintauro P, Bennion D (1984) Mass transport of electrolytes in membranes. 1. Development of mathematical transport model. *Ind & Eng Chem Fundamentals*, 23(2):230–234
- [365] Natarajan D, Nguyen TV (2004) Effect of electrode configuration and electronic conductivity on current density distribution measurements in PEM fuel cells. *J Power Sources*, 135(1):95–109

- [366] Becker J, Flückiger R, Reum M, Büchi FN, Marone F, Stampanoni M (2009) Determination of material properties of gas diffusion layers: experiments and simulations using phase contrast tomographic microscopy. *J Electrochem Soc*, 156(10):B1175–B1181
- [367] Suzuki T, Murata H, Hatanaka T, Morimoto Y (2003) Analysis of the catalyst layer of polymer electrolyte fuel cells. *R&D Rev Toyota CRDL*, 39(3):33–38
- [368] Morris DR, Liu SP, Villegas Gonzalez D, Gostick JT (2014) Effect of water sorption on the electronic conductivity of porous polymer electrolyte membrane fuel cell catalyst layers. *ACS applied materials & interfaces*, 6(21):18609–18618
- [369] Weber AZ, Newman J (2003) Transport in polymer-electrolyte membranes: I. Physical model. *J Electrochem Soc*, 150(7):A1008–A1015
- [370] Bekkedahl T (2007), In-Plane Conductivity Testing Procedures & Results. In DOE High Temperature Membrane Working Group Meeting, Arlington, VA
- [371] Iden H, Ohma A, Shinohara K (2009) Analysis of proton transport in pseudo catalyst layers. *J The Electrochem Soc*, 156(9):B1078–B1084
- [372] Fuller TF, Newman J (1993) Water and thermal management in solid-polymer-electrolyte fuel cells. *J Electrochem Soc*, 140(5):1218–1225
- [373] Peron J, Edwards D, Haldane M, Luo X, Zhang Y, Holdcroft S, Shi Z (2011) Fuel cell catalyst layers containing short-side-chain perfluorosulfonic acid ionomers. *J Power Sources*, 196(1):179–181
- [374] Vang J, Zhou F, Andreasen S, Kær S (2015) Estimating important electrode parameters of high temperature PEM fuel cells by fitting a model to polarisation curves and impedance spectra. *Ecs Transactions*, 68(3):13–34
- [375] Adzakpa K, Agbossou K, Dube Y, Dostie M, Fournier M, Poulin A (2008) PEM fuel cells modeling and analysis through current and voltage transient behaviors. *IEEE Transactions on Energy Convers*, 23(2):581–591
- [376] Makharia R, Mathias M, Baker D (2005) Measurement of catalyst layer electrolyte resistance in PEFCs using electrochemical impedance spectroscopy. *J Electrochem Soc*, 152(5):A970–A977
- [377] Springer T, Zawodzinski T, Wilson M, Gottesfeld S (1996) Characterization of polymer electrolyte fuel cells using AC impedance spectroscopy. *J Electrochem Soc*, 143(2):587–599
- [378] Baricci A, Zago M, Casalegno A (2014) A quasi 2D model of a high temperature polymer fuel cell for the interpretation of impedance spectra. *Fuel Cells*, 14(6):926–937
- [379] Shamardina O, Kondratenko M, Chertovich A, Kulikovskiy A (2014) A simple transient model for a high temperature PEM fuel cell impedance. *Int J Hydrog Energy*, 39(5):2224–2235
- [380] Tant S, Rosini S, Thivel PX, Druart F, Rakotondrainibe A, Geneston T, Bultel Y (2014) An algorithm for diagnosis of proton exchange membrane fuel cells by electrochemical impedance spectroscopy. *Electrochimica Acta*, 135:368–379
- [381] Choopanya P, Yang Z (2014). In Transient performance investigation of different flow-field designs of automotive polymer electrolyte membrane fuel cell (PEMFC) using computational fluid dynamics (CFD). International Conference on Heat Transfer, Fluid Mechanics and Thermodynamics
- [382] Sun W, Peppley BA, Karan K (2005) Modeling the influence of GDL and flow-field plate parameters on the reaction distribution in the PEMFC cathode catalyst layer. *J Power Sources*, 144(1):42–53
- [383] Chen S, Kucernak A (2004) Electrocatalysis under conditions of high mass transport: investigation of hydrogen oxidation on single submicron Pt particles supported on carbon. *The J Phys Chem B*, 108(37):13984–13994
- [384] Gasteiger H, Panels J, Yan S (2004) Dependence of PEM fuel cell performance on catalyst loading. *J Power Sources*, 127(1):162–171
- [385] Damjanovic A, Brusic V (1967) Electrode kinetics of oxygen reduction on oxide-free platinum electrodes. *Electrochimica Acta*, 12(6):615–628

- [386] Paucirova M, Drazic D, Damjanovic A (1973) The effect of surface coverage by adsorbed oxygen on the kinetics of oxygen reduction at oxide free platinum. *Electrochimica Acta*, 18(12):945–951
- [387] Parthasarathy A, Srinivasan S, Appleby AJ, Martin CR (1992) Temperature dependence of the electrode kinetics of oxygen reduction at the platinum/Nafion® interface—a microelectrode investigation. *J Electrochem Soc*, 139(9):2530–2537
- [388] Markiewicz M, Zalitis C, Kucernak A (2015) Performance measurements and modelling of the ORR on fuel cell electrocatalysts—the modified double trap model. *Electrochimica Acta*, 179:126–136
- [389] Tafel J (1905) Über die Polarisation bei kathodischer Wasserstoffentwicklung. *Z Phys Chem*, 50:641
- [390] Heyrovský J (1927) A theory of overpotential. *Recueil des Travaux Chimiques des Pays-Bas*, 46(8):582–585
- [391] Volmer M, Erdey-Gruz T (1930). Principles of adsorption and reaction on solid surfaces
- [392] de Chialvo MRG, Chialvo AC (2004) Hydrogen diffusion effects on the kinetics of the hydrogen electrode reaction. Part I. Theoretical aspects. *Phys Chem Chem Phys*, 6(15):4009–4017
- [393] Quaino PM, de Chialvo MRG, Chialvo AC (2004) Hydrogen diffusion effects on the kinetics of the hydrogen electrode reaction Part II. Evaluation of kinetic parameters. *Phys Chem Chem Phys*, 6(18):4450–4455
- [394] Sepa D, Vojnovic M, Damjanovic A (1981) Reaction intermediates as a controlling factor in the kinetics and mechanism of oxygen reduction at platinum electrodes. *Electrochimica Acta*, 26(6):781–793
- [395] Antoine O, Bultel Y, Durand R (2001) Oxygen reduction reaction kinetics and mechanism on platinum nanoparticles inside Nafion®. *J Electroanal Chem*, 499(1):85–94
- [396] Eslamibidgoli MJ, Huang J, Kadyk T, Malek A, Eikerling M (2016) How theory and simulation can drive fuel cell electrocatalysis. *Nano Energy*, 29:334–361
- [397] Wang JX, Zhang J, Adzic RR (2007) Double-trap kinetic equation for the oxygen reduction reaction on Pt (111) in acidic media. *The J Phys Chem A*, 111(49):12702–12710
- [398] Walch S, Dhanda A, Aryanpour M, Pitsch H (2008) Mechanism of molecular oxygen reduction at the cathode of a PEM fuel cell: non-electrochemical reactions on catalytic Pt particles. *The J Phys Chem C*, 112(22):8464–8475
- [399] Moore M, Putz A, Secanell M (2012), Development of a Cathode Electrode Model Using the ORR Dual-Trap Intrinsic Kinetic Model. In ASME 2012 10th International Conference on Fuel Cell Science, Engineering and Technology collocated with the ASME 2012 6th International Conference on Energy Sustainability, pages 367–376. American Society of Mechanical Engineers
- [400] Medici E, Zenyuk I, Parkinson D, Weber A, Allen J (2016) Understanding water transport in polymer electrolyte fuel cells using coupled continuum and pore-network models. *Fuel Cells*, 16(6):725–733
- [401] Moore M (2012), Investigation of the double-trap intrinsic kinetic equation for the oxygen reduction reaction and its implementation into a membrane electrode assembly model. Master’s thesis, University of Alberta
- [402] Huang BT, Chatillon Y, Bonnet C, Lopicque F, Leclerc S, Hinaje M, Raël S (2012) Experimental investigation of air relative humidity (rh) cycling tests on mea/cell aging in pemfc part ii: study of low rh cycling test with air rh at 62%/0%. *Fuel Cells*, 12(3):347–355
- [403] Breaz E, Gao F, Miraoui A, Tirnovan R (2014), A short review of aging mechanism modeling of proton exchange membrane fuel cell in transportation applications. In Industrial Electronics Society, IECON 2014-40th Annual Conference of the IEEE, pages 3941–3947. IEEE
- [404] Wang L, Husar A, Zhou T, Liu H (2003) A parametric study of PEM fuel cell performances. *Int J Hydrog Energy*, 28(11):1263–1272
- [405] Mazumder S, Cole JV (2003) Rigorous 3-D mathematical modeling of PEM fuel cells II. Model predictions with liquid water transport. *J Electrochem Soc*, 150(11):A1510–A1517
- [406] Ju H, Meng H, Wang CY (2005) A single-phase, non-isothermal model for PEM fuel cells. *Int J Heat Mass Transf*, 48(7):1303–1315

- [407] Ju H, Wang CY, Cleghorn S, Beuscher U (2005) Nonisothermal modeling of polymer electrolyte fuel cells I. Experimental validation. *J Electrochem Soc*, 152(8):A1645–A1653
- [408] Dutta SSS (2000) Numerical prediction of temperature distribution in PEM fuel cells. *Numer Heat Transfer: Part A: Appl*, 38(2):111–128
- [409] Wang Y, Wang CY (2006) A nonisothermal, two-phase model for polymer electrolyte fuel cells. *J electrochemical society*, 153(6):A1193–A1200
- [410] Rowe A, Li X (2001) Mathematical modeling of proton exchange membrane fuel cells. *J Power Sources*, 102(1):82–96
- [411] Ramousse J, Deseure J, Lottin O, Didierjean S, Maillet D (2005) Modelling of heat, mass and charge transfer in a PEMFC single cell. *J Power Sources*, 145(2):416–427
- [412] Weber AZ, Newman J (2006) Coupled thermal and water management in polymer electrolyte fuel cells. *J Electrochem Soc*, 153(12):A2205–A2214
- [413] Birgersson E, Noponen M, Vynnycky M (2005) Analysis of a two-phase non-isothermal model for a PEFC. *J Electrochem Soc*, 152(5):A1021–A1034
- [414] Pasaogullari U, Mukherjee P, Wang CY, Chen K (2007) Anisotropic heat and water transport in a PEFC cathode gas diffusion layer. *J Electrochem Soc*, 154(8):B823–B834
- [415] Bapat CJ, Thynell ST (2007) Anisotropic heat conduction effects in proton-exchange membrane fuel cells. *J Heat Transf*, 129(9):1109–1118
- [416] Zamel N, Li X (2010) Non-isothermal multi-phase modeling of PEM fuel cell cathode. *Int J Energy Res*, 34(7):568–584
- [417] Berning T, Djilali N (2003) A 3D, multiphase, multicomponent model of the cathode and anode of a PEM fuel cell. *J Electrochem Soc*, 150(12):A1589–A1598
- [418] Hwang J, Chen P (2006) Heat/mass transfer in porous electrodes of fuel cells. *Int J Heat Mass Transf*, 49(13):2315–2327
- [419] Hwang J, Chao C, Wu W (2006) Thermal-fluid transports in a five-layer membrane-electrode assembly of a PEM fuel cell. *J Power Sources*, 163(1):450–459
- [420] Hwang J, Chao C, Chang C, Ho W, Wang D (2007) Modeling of two-phase temperatures in a two-layer porous cathode of polymer electrolyte fuel cells. *Int J Hydrog Energy*, 32(3):405–414
- [421] Popiel C, Wojtkowiak J (1998) Simple formulas for thermophysical properties of liquid water for heat transfer calculations (from 0 °C to 150 °C). *Heat Transf Eng*, 19(3):87–101
- [422] Chung DW, Ebner M, Ely DR, Wood V, García RE (2013) Validity of the Bruggeman relation for porous electrodes. *Model Simul Mater Sci Eng*, 21(7):074009
- [423] Aharony A, Stauffer D (2003), *Introduction to percolation theory*. Taylor & Francis
- [424] Ostadi H, Rama P, Liu Y, Chen R, Zhang X, Jiang K (2010) 3D reconstruction of a gas diffusion layer and a microporous layer. *J Membr Sci*, 351(1):69–74
- [425] García-Salaberri PA, Gostick JT, Hwang G, Weber AZ, Vera M (2015) Effective diffusivity in partially-saturated carbon-fiber gas diffusion layers: Effect of local saturation and application to macroscopic continuum models. *J Power Sources*, 296:440–453
- [426] García-Salaberri PA, Hwang G, Vera M, Weber AZ, Gostick JT (2015) Effective diffusivity in partially-saturated carbon-fiber gas diffusion layers: Effect of through-plane saturation distribution. *Int J Heat Mass Transf*, 58:319–333
- [427] Fazeli M, Hinebaugh J, Bazylak A (2016) Incorporating embedded microporous layers into topologically equivalent pore network models for oxygen diffusivity calculations in polymer electrolyte membrane fuel cell gas diffusion layers. *Electrochimica Acta*, 216:364–375

- [428] Hinebaugh J, Fishman Z, Bazylak A (2010) Unstructured pore network modeling with heterogeneous PEMFC GDL porosity distributions. *J Electrochem Soc*, 157(11):B1651–B1657
- [429] Zenyuk IV, Weber AZ (2015) Understanding liquid-water management in PEFCs using X-ray computed tomography and modeling. *ECS Transactions*, 69(17):1253–1265
- [430] Zenyuk IV, Parkinson DY, Hwang G, Weber AZ (2015) Probing water distribution in compressed fuel-cell gas-diffusion layers using X-ray computed tomography. *Electrochem Commun*, 53:24–28
- [431] Kotaka T, Tabuchi Y, Mukherjee PP (2015) Microstructural analysis of mass transport phenomena in gas diffusion media for high current density operation in PEM fuel cells. *J Power Sources*, 280:231–239
- [432] Berejnov V, Susac D, Stumper J, Hitchcock AP (2011) Nano to micro scale characterization of water uptake in the catalyst coated membrane measured by soft X-ray scanning transmission X-ray microscopy. *ECS Transactions*, 41(1):395–402
- [433] Saha MS, Tam M, Berejnov V, Susac D, McDermid S, Hitchcock AP, Stumper J (2013) Characterization and performance of catalyst layers prepared by inkjet printing technology. *ECS Transactions*, 58(1):797–806
- [434] Susac D, Berejnov V, Hitchcock AP, Stumper J (2013) STXM characterization of PEM fuel cell catalyst layers. *ECS Transactions*, 50(2):405–413
- [435] Wargo E, Hanna A, Cecen A, Kalidindi S, Kumbur E (2012) Selection of representative volume elements for pore-scale analysis of transport in fuel cell materials. *J Power Sources*, 197:168–179
- [436] Barbosa R, Andaverde J, Escobar B, Cano U (2011) Stochastic reconstruction and a scaling method to determine effective transport coefficients of a proton exchange membrane fuel cell catalyst layer. *J Power Sources*, 196(3):1248–1257
- [437] Sinha PK, Mukherjee PP, Wang CY (2007) Impact of GDL structure and wettability on water management in polymer electrolyte fuel cells. *J Mater Chem*, 17(30):3089–3103
- [438] Becker J, Wieser C, Fell S, Steiner K (2011) A multi-scale approach to material modeling of fuel cell diffusion media. *Int J Heat Mass Transf*, 54:1360–1368
- [439] Lange KJ, Misra C, Sui PC, Djilali N (2011) A numerical study on preconditioning and partitioning schemes for reactive transport in a PEMFC catalyst layer. *Comput Methods Appl Mech Eng*, 200(9):905–916
- [440] Vogel HJ, Tölke J, Schulz V, Krafczyk M, Roth K (2005) Comparison of a lattice-Boltzmann model, a full-morphology model, and a pore network model for determining capillary pressure–saturation relationships. *Vadose Zone J*, 4(2):380–388
- [441] Mukherjee PP, Wang CY, Kang Q (2009) Mesoscopic modeling of two-phase behavior and flooding phenomena in polymer electrolyte fuel cells. *Electrochimica Acta*, 54(27):6861–6875
- [442] Pharoah J, Choi HW, Chueh CC, Harvey DB (2011) Effective transport properties accounting for electrochemical reactions of proton-exchange membrane fuel cell catalyst layers. *ECS Transactions*, 41(1):221–227
- [443] El Hannach M, Pauchet J, Prat M (2011) Pore network modeling: Application to multiphase transport inside the cathode catalyst layer of proton exchange membrane fuel cell. *Electrochimica Acta*, 56(28):10796–10808
- [444] El Hannach M, Prat M, Pauchet J (2012) Pore network model of the cathode catalyst layer of proton exchange membrane fuel cells: Analysis of water management and electrical performance. *Int J Hydrog Energy*, 37(24):18996–19006
- [445] Wu R, Zhu X, Liao Q, Wang H, Ding Yd, Li J, Ye Dd (2010) A pore network study on water distribution in bi-layer gas diffusion media: effects of inlet boundary condition and micro-porous layer properties. *international journal hydrogen energy*, 35(17):9134–9143
- [446] Wu R, Zhu X, Liao Q, Wang H, Ding Yd, Li J, Ye Dd (2010) A pore network study on the role of micro-porous layer in control of liquid water distribution in gas diffusion layer. *international journal hydrogen energy*, 35(14):7588–7593

- [447] Gostick JT (2013) Random pore network modeling of fibrous PEMFC gas diffusion media using Voronoi and Delaunay tessellations. *J Electrochem Soc*, 160(8):F731–F743
- [448] Berson A, Choi HW, Pharoah JG (2011) Determination of the effective gas diffusivity of a porous composite medium from the three-dimensional reconstruction of its microstructure. *Phys Rev E*, 83:026310
- [449] Kim SH, Pitsch H (2009) Reconstruction and effective transport properties of the catalyst layer in PEM fuel cells. *J Electrochem Soc*, 156(6):B673–B681
- [450] Becker J, Schulz V, Wiegmann A (2008) Numerical determination of two-phase material parameters of a gas diffusion layer using tomography images. *J Fuel Cell Sci Technol*, 5(2):021006
- [451] El Hannach M, Singh R, Djilali N, Kjeang E (2015) Micro-porous layer stochastic reconstruction and transport parameter determination. *J Power Sources*, 282:58–64
- [452] El Hannach M, Kjeang E (2014) Stochastic microstructural modeling of PEFC gas diffusion media. *J Electrochem Soc*, 161(9):F951–F960
- [453] Espinola A, Miguel PM, Salles MR, Pinto AR (1986) Electrical properties of carbons—resistance of powder materials. *Carbon*, 24(3):337–341
- [454] Jinnouchi R, Kudo K, Kitano N, Morimoto Y (2016) Molecular dynamics simulations on  $O_2$  permeation through Nafion ionomer on platinum surface. *Electrochimica Acta*, 188:767–776
- [455] Kudo K, Morimoto Y (2013) Analysis of oxygen transport resistance of Nafion thin film on Pt electrode. *ECS Transactions*, 50(2):1487–1494
- [456] Hao L, Cheng P (2010) Lattice Boltzmann simulations of water transport in gas diffusion layer of a polymer electrolyte membrane fuel cell. *J Power Sources*, 195(12):3870–3881
- [457] Moriyama K, Inamuro T (2011) Lattice Boltzmann simulations of water transport from the gas diffusion layer to the gas channel in PEFC. *Commun Comput Phys*, 9(5):1206–1218
- [458] Kim KN, Kang JH, Lee SG, Nam JH, Kim CJ (2015) Lattice Boltzmann simulation of liquid water transport in microporous and gas diffusion layers of polymer electrolyte membrane fuel cells. *J Power Sources*, 278:703–717
- [459] Sinha PK, Wang CY (2007) Pore-network modeling of liquid water transport in gas diffusion layer of a polymer electrolyte fuel cell. *Electrochimica Acta*, 52(28):7936–7945
- [460] Ji Y, Luo G, Wang CY (2010) Pore-level liquid water transport through composite diffusion media of PEMFC. *J Electrochem Soc*, 157(12):B1753–B1761
- [461] Schulz VP, Wargo EA, Kumbur EC (2015) Pore-morphology-based simulation of drainage in porous media featuring a locally variable contact angle. *Transp Porous Media*, 107(1):13–25
- [462] Schulz VP, Becker J, Wiegmann A, Mukherjee PP, Wang CY (2007) Modeling of two-phase behavior in the gas diffusion medium of PEFCs via full morphology approach. *J Electrochem Soc*, 154(4):B419–B426
- [463] Zamel N, Li X, Becker J, Wiegmann A (2011) Effect of liquid water on transport properties of the gas diffusion layer of polymer electrolyte membrane fuel cells. *Int J Hydrog Energy*, 36(9):5466–5478
- [464] Fazeli M, Hinebaugh J, Bazylak A (2015) Investigating inlet condition effects on PEMFC GDL liquid water transport through pore network modeling. *J Electrochem Soc*, 162(7):F661–F668
- [465] Zenyuk IV, Lamibrac A, Eller J, Parkinson DY, Marone F, Büchi FN, Weber AZ (2016) Investigating evaporation in gas diffusion layers for fuel cells with X-ray computed tomography. *The J Phys Chem C*, 120(50):28701–28711
- [466] Lobato J, Cañizares P, Rodrigo MA, Pinar FJ, Mena E, Úbeda D (2010) Three-dimensional model of a 50 cm<sup>2</sup> high temperature PEM fuel cell. Study of the flow channel geometry influence. *Int J Hydrog Energy*, 35(11):5510–5520
- [467] Wang Y, Basu S, Wang CY (2008) Modeling two-phase flow in PEM fuel cell channels. *J Power Sources*, 179(2):603–617

- [468] Jiao K, Zhou B (2007) Innovative gas diffusion layers and their water removal characteristics in PEM fuel cell cathode. *J Power Sources*, 169(2):296–314
- [469] Chen L, Cao T, Li Z, He Y, Tao W (2012) Numerical investigation of liquid water distribution in the cathode side of proton exchange membrane fuel cell and its effects on cell performance. *Int J Hydrog Energy*, 37(11):9155–9170
- [470] Zhou J, Shukla S, Putz A, Secanell M (2017) Understanding the role of micro porous layer on fuel cell performance using a non-isothermal two-phase model. *Electrochem Acta* (to be submitted)
- [471] Nguyen PT, Berning T, Djilali N (2004) Computational model of a PEM fuel cell with serpentine gas flow channels. *J Power Sources*, 130(1):149–157
- [472] Gerris flow solver. [http://gfs.sourceforge.net/wiki/index.php/Main\\_Page](http://gfs.sourceforge.net/wiki/index.php/Main_Page). Accessed on 07.12.2017
- [473] Arndt D, Bangerth W, Davydov D, Heister T, Heltai L, Kronbichler M, Maier M, Pelteret JP, Turcksin B, Wells D (2017) The deal.II library, version 8.5. *J Numer Math*
- [474] Kelly DW, de S. R. Gago JP, Zienkiewicz OC, Babuska I (1983) A posteriori error analysis and adaptive processes in the finite element method: Part I - Error analysis. *Int J for Numer Methods Eng*, 19(11):1593–1619
- [475] Math2Market® GmbH (2017). GeoDict®
- [476] Palabos. <http://www.palabos.org/>. Accessed on 07.25.2017
- [477] Gostick J, Aghighi M, Hinebaugh J, Tranter T, Hoeh MA, Day H, Spellacy B, Sharqawy MH, Bazylak A, Burns A et al. (2016) Openpnm: A pore network modeling package. *Comput Sci & Eng*, 18(4):60–74